



UNIVERSITAT_{DE}
BARCELONA

Algorithms for light applications: from theoretical simulations to prototyping

Adrià Huguet Ferran



Aquesta tesi doctoral està subjecta a la llicència **Reconeixement 4.0. Espanya de Creative Commons.**

Esta tesis doctoral está sujeta a la licencia **Reconocimiento 4.0. España de Creative Commons.**

This doctoral thesis is licensed under the **Creative Commons Attribution 4.0. Spain License.**

PhD Thesis

Algorithms for light
applications: from theoretical
simulations to prototyping

Adrià Huguet Ferran



UNIVERSITAT^{DE}
BARCELONA

Algorithms for light applications: from theoretical simulations to prototyping

Programa de doctorat en Enginyeria i Ciències Aplicades

Adrià Huguet Ferran



Directors:

Sergi Hernández Márquez

Blas Garrido Fernández

Tutor:

Sergi Hernández Márquez



UNIVERSITAT DE
BARCELONA

Table of Contents

Abstract	5
Resum	6
1 Introduction.....	7
1.1 Light-emitting devices: an Overview	7
1.2 State-of-the-art.....	8
1.3 Outline of the thesis.....	10
2 Fundamentals of light and algorithms	13
2.1 Light	13
2.1.1 The physics of light.....	13
2.1.2 Human perception of light.....	17
2.1.3 Photometric units.....	22
2.1.4 Colorimetry	25
2.1.5 Circadian parameters	40
2.1.6 LED luminaires	44
2.1.7 Multichannel LED light sources.....	54
2.1.8 Sensors, spectrometers, and microcontrollers	58
2.2 Algorithms	62
2.2.1 Classical optimization algorithms.....	63
2.2.2 Machine learning and neural networks.....	63
3 Objectives	71
4 Light emission.....	73
4.1 Algorithms for light emission	74
4.1.1 High resolution calculations	86
4.1.2 Colorimetric and non-visual parameters	97
4.2 Luminaires for experimental verification	105

4.2.1	Development of a control system	105
4.2.2	First version of the prototypes	106
4.2.3	Second version of the prototypes.....	113
4.2.4	Third version of the prototypes.....	119
4.3	Results	129
4.3.1	Measuring the light of the prototypes	129
4.3.2	Showroom installation	136
4.3.3	Measuring the light of a commercial device	137
5	Light sensing	142
5.1	Algorithms for light sensing	144
5.1.1	Sensor selection	145
5.1.2	Microcontroller selection	147
5.1.3	Sensor module simulation.....	148
5.1.4	Creating random SPDs.....	150
5.1.5	Interpolated measurements	152
5.1.6	Spectral reconstruction neural network.....	162
5.1.7	Direct calculation of colorimetric parameters.....	170
5.1.8	Comparison of all the models developed	174
5.1.9	Using a real set of white LED-sources.....	175
5.2	Color sensor for experimental verification	181
5.3	Results	185
6	Conclusions	193
6.1	Conclusions	194
6.2	Future work	201
6.2.1	Light emission	201
6.2.2	Light sensing	202
7	Supplementary tables	204

8	List of Figures.....	211
9	List of Tables	225
10	References	228

Abstract

Although the first LED dates to the middle of the 20th century, it has not been until the last decade that the market has been flooded with high efficiency and high durability LED solutions compared to previous technologies. In addition, luminaires that include types of LEDs differentiated in hue or color have already appeared. These luminaires offer new possibilities to reach colorimetric or non-visual capabilities not seen to date.

Due to the enormous number of LEDs on the market, with very different spectral characteristics, the use of the spectrometer as a measuring device for determining LEDs properties has become popular. Obtaining colorimetric information from a luminaire is a necessary step to commercialize it, so it is a tool commonly used by many LED manufacturers.

This thesis aims at contributing to advance the state of the art and knowledge of LEDs both at the spectral emission level and at the sensor level. On the one hand, we have developed a new spectral simulation algorithm that allows obtaining a large number of results, being able to obtain optimized values of a large number of colorimetric and non-visual parameters. On the other hand, the improvement of the performance of a multichannel colorimetric sensor is explored, providing it with a neural network for spectral reconstruction. In both cases, prototypes are developed as a demonstrator of the theoretical framework generated.

Resum

Tot i que el primer LED apareix a meitats del segle XX, no ha estat fins l'última dècada que el mercat s'ha omplert de solucions LED d'alta eficiència i durabilitat en comparació amb tecnologies anteriors. A més, ja han aparegut lluminàries que inclouen tipus de LEDs diferenciats per tonalitat o color.

Degut a la gran quantitat de LEDs disponibles al mercat amb característiques espectrals diferents, l'ús de l'espectòmetre com a mètode de mesura per determinar les propietats d'aquests LEDs ha esdevingut molt popular. Obtenir informació colorimètrica d'una lluminària és un pas necessari per a comercialitzar-la i ha esdevingut una eina extensament emprada entre els fabricants de LEDs.

Aquesta tesi pretén contribuir a avançar en l'estat de l'art i el coneixement sobre LEDs tant a nivell d'emissió espectral com de sensòrica. Per una banda, hem desenvolupat un nou algoritme de simulació espectral que permet obtenir un nombre molt elevat de resultats, sent capaços d'obtenir valors optimitzats a partir d'un gran nombre de paràmetres colorimètrics i no-visuals. Per altra banda, s'explora la millora funcional d'un sensor colorimètric multicanal, dotant-lo d'una xarxa neuronal per a la reconstrucció espectral. En tots dos casos, s'han desenvolupat prototips per a la demostració del marc teòric generat.

1 Introduction

1.1 Light-emitting devices: an Overview

Currently, the technology that dominates the lighting market is the light-emitting diode (LED). There are many types of LEDs, in terms of electrical power, brightness, color, hue or shape. Beyond the light-emitting device itself, the electrical characteristics have made it possible to assemble large numbers of LEDs in a single housing, making it possible to combine their light very easily. This versatility has enabled the creation of new light sources that are much better adapted to the installation environment, both architecturally and in terms of user needs. Being able to modulate and control dynamic-light luminaires, with different LEDs coexisting in the same electrical circuit, has opened up new possibilities for manufacturing intelligent devices, with a logic behind them that can depend on the surrounding conditions and improve the user experience or save energy, among other possibilities.

On the other hand, the huge catalog of LEDs available on the market has increased the need for luminaire characterization. The different regulations require minimum quality values that can be affected by elements external to the LEDs, such as an optical diffuser or poor thermal dissipation. For this reason, devices such as spectrometers are becoming increasingly common among professionals in the sector.

In parallel, the need to create algorithms that can help optimize and measure the light emitted by a luminaire has arisen. These

algorithms focus on the general behavior of a luminaire, specifically on the spectrum and power (luminous and electrical) of emission, for example by improving colorimetric parameters, or by simulating the emission pattern of a luminaire, as well as its distribution in a space.

1.2 State-of-the-art

The combination of the different colors of the LEDs of a multichannel light source with the aim of obtaining specific colors or spectra is not new. In 2004, long before the boom of LED technology in the field of lighting, publications on the optimization of colorimetric parameters such as the Color Rendering Index and its difficulties due to the non-linearity of the calculations were already beginning to be published [1].

Recently, algorithms dedicated to the optimization of lighting parameters have evolved and numerous research groups have continued to improve the results. For example, control techniques have been developed for luminaires that offer a deviation of less than 50 K in the Correlated Color Temperature [2]. Others have incorporated sensors to provide feedback to the microcontroller of the luminaire, being able to perform precise calculations instantaneously. This fact is especially interesting in cases where temperature variations can be important or there is a degradation of the LEDs used, since the emission spectrum of an LED is strongly conditioned by these variables, although they are not the only ones. The deviations have been corrected in such a way that the shift due to these factors is negligible to the human

eye [3]. In other cases, new algorithms have been created to perform optimization calculations on the luminaire's own microcontroller, without the need to use an external computer [4]. In addition to improving performance, the optimization of color fidelity values of new metrics, potentially maintaining a high value of luminous efficacy, has been published [5].

Some of these results can already be found in widely used commercial devices, such as Philips Hue, IKEA TRÅDFRI or LIFX bulbs. In all these cases the light from the different LEDs inside the bulb are mixed to ensure a good quality of light in different hues.

On the other hand, the strong and rapid adoption of LEDs as a lighting technology has led to the need for accurate measurements of the new luminaires produced by the manufacturers. Both light and color sensors, which operate with filters, and spectrometers, which operate with diffraction gratings, are commonly used for measurements. However, there has been no notable evolution of the technology in recent years, and although the systems are becoming more stable and user-friendly, they are already good enough to perform their task. However, it should be noted that some colorimetric parameters require the use of a spectrometer, which costs several orders of magnitude more than a color sensor.

1.3 Outline of the thesis

This doctoral thesis has been built from the need to investigate new dynamic light sources and new ways to process the data obtained by sensors. The good results of some of the initial developments motivated to create a spinoff company of Universitat de Barcelona called Enlighting Technologies S.L., which operates under Kumux brand. This company, created in June 2017, is in the commercialization phase of its developed products, all of them linked to lighting and software. During the development of the thesis, the company has participated in business (Neotec, Urban Centric Lighting) and scientific (SHAPE) projects, and the deposit of a patent at European and American level has been made. On the other hand, the work carried out has also been presented at different conferences such as Light Symposium 2022, Light Professional Symposium (LpS) 2016 and 2020, obtaining the Best Scientific Lecture/Paper - Technology Award 2020.

In terms of structure, this doctoral thesis is composed of two main blocks: light emission and light sensing. The main Chapters developed are described below:

- Chapter 1 (Introduction) is related to the generic presentation of the topics to be covered, a summary of the thesis outline and a section dedicated to the state-of-the-art of the technology.
- Chapter 2 (Fundamentals of light and algorithms) provides the theoretical basis that will explain the

central content of the thesis. The essential parameters related to light and algorithmics are discussed.

- Chapter 3 (Objectives) defines the specific objectives of the work and presents the metrics that will be used to measure the results.
- Chapter 4 (Light emission) is focused on light emission algorithms. The method of the registered patent, the SHAPE project to perform calculations with MareNostrum 4 supercomputer and an adaptation of the LpS 2020 paper are presented. Later, the prototypes created are shown, and their results are experimentally measured.
- Chapter 5 (Light sensing) is focused on light sensing algorithms. A choice of a multichannel color sensor and a microcontroller is made, and a theoretical model is created to increase the resolution of the sensor so that it can operate as a spectrometer. Subsequently, the created prototypes are trained and a transfer of the theoretical model to an experimental model is made, being able to perform measurements with the prototype. Finally, the results obtained are evaluated.
- Chapter 6 (Conclusions) lists the general conclusions drawn from the work, as well as a proposal for future work.

- Chapter 7 (Supplementary tables) is devoted to tables of raw experimental results, without any previous treatment.

2 Fundamentals of light and algorithms

2.1 Light

2.1.1 The physics of light

Nature of light has been widely discussed along the history of humanity: Christian Huygens proposed a wave theory to explain the observed phenomena, while Isaac Newton proposed a particle theory. Later, Fresnel, Maxwell, and Young certified Huygens' theories, thus calling Newton's view into question [6]. At the beginning of the 20th century, Albert Einstein explained the photoelectric effect based on photons, putting the corpuscular theory back in the spotlight [7]. Soon after, the physicist Louis-Victor de Broglie related the wavelength to the linear momentum of particles, postulating a duality of wave and particle [8]. Today, given these discoveries, it is accepted that light can be characterized as an electromagnetic wave or as a collection of particles (photons), depending on the properties observed in an experiment. This duality of observation is called wave-corpuscule duality (or wave-particle duality, depending on the author). It extends to all existing particles, so it is not a postulate reserved only for light.

When we speak about electromagnetic radiation, we mean the propagation of electromagnetic waves carrying electromagnetic radiant energy [9]. Depending on the energy, electromagnetic radiation can be divided into gamma rays, X-rays, ultraviolet, visible light, infrared, microwaves, and radio waves [10]. Visible light is a small region within the electromagnetic spectrum, so

radiation outside this range is not observable to the human eye. Figure 2-1 represents the visible spectrum in comparison with the rest of the spectrum:

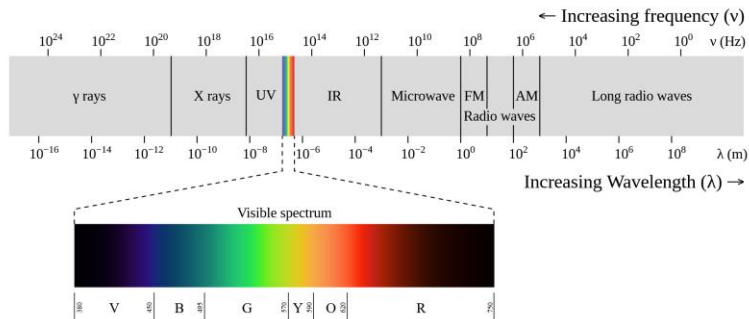


Figure 2-1. The electromagnetic spectrum, with the visible portion, highlighted [11].

Within the visible spectrum, the shortest wavelengths are associated with the violet color, passing through blue, green, yellow, orange, and red, with wavelengths close to 700 nm. The boundaries of the visible spectrum are not entirely clear and vary depending on the source, as color is a subjective measure and may depend on the study and radiant power that reaches the retina [12]. However, the most up-to-date colorimetric evaluation methods use a range from 380 nm to 780 nm to define the visible range [13].

In general, the wavelength ranges that are accepted to delimit the different colors are summarized in Table 2-1:

Table 2-1. Relationship between color and wavelength [14].

Color	Wavelength range (nm)
Ultraviolet	< 390
Violet	390 - 455
Blue	455 - 490
Cyan	490 - 515
Green	515 - 570
Yellow	570 - 600
Amber	590 - 600
Orange	600 - 625
Red	625 - 720
Infrared	> 720

A light source is normally not purely monochromatic, so it emits optical power at various wavelengths. We can define the spectral power distribution (SPD) as the optical power per unit of wavelength. The entire visual perception of a light source, as well as the colorimetric parameters that define it, depends on its SPD. There is a theoretically infinite number of SPDs capable of generating white light. Among all the possibilities, there is one that is particularly interesting for the study of the effect of light on human perception and vision: blackbody radiation.

All bodies emit energy in the form of electromagnetic waves simply because they have a certain temperature associated to them. At room temperature, this emission cannot be perceived by the eye, since the emission is very weak, and the SPD is almost completely in the infrared region, where the eye is not sensitive. As the temperature of a body increases, the emission of electromagnetic radiation also increases, and the SPD peak enters the visible light range, so it become perceptible to the human eye.

A black body is an ideal object that absorbs all the radiation incident on it. Despite its name, the black body also emits electromagnetic radiation because it is at a certain temperature, constituting an ideal physical system. Radiance is only characterized by its temperature, as shown in Equation (1):

$$I(\lambda, T) = \frac{2hc^2}{\lambda^5 [\exp(\frac{hc}{\lambda kT}) - 1]} \quad (1)$$

where h is Planck's constant, c is the speed of light in vacuum, k is Boltzmann's constant, λ is the wavelength and T is the temperature. Figure 2-2 shows a normalized black body radiation at different temperatures:

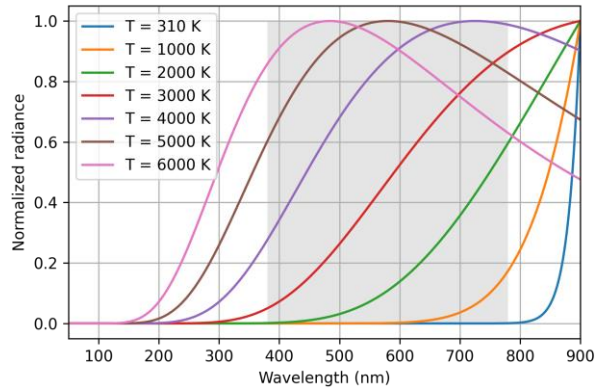


Figure 2-2. Normalized blackbody radiation at different temperatures.

The gray region indicates the visible range.

These relations were developed by Max Planck in 1900 and signified the beginning of quantum physics, since they could not be explained by the classical theories existing at that time [15].

Sunlight is caused by the blackbody radiation from the outermost layer of the Sun, its atmosphere, which is at 5772 K [16]. Human beings have evolved considering the light conditions provided over time by the Sun. Although there are many factors that prevent sunlight from reaching our retina while preserving the properties of an ideal black body, its spectral shape and dynamism have marked the way we perceive the objects around us. Figure 2-3 shows the solar irradiance above the atmosphere and surface:

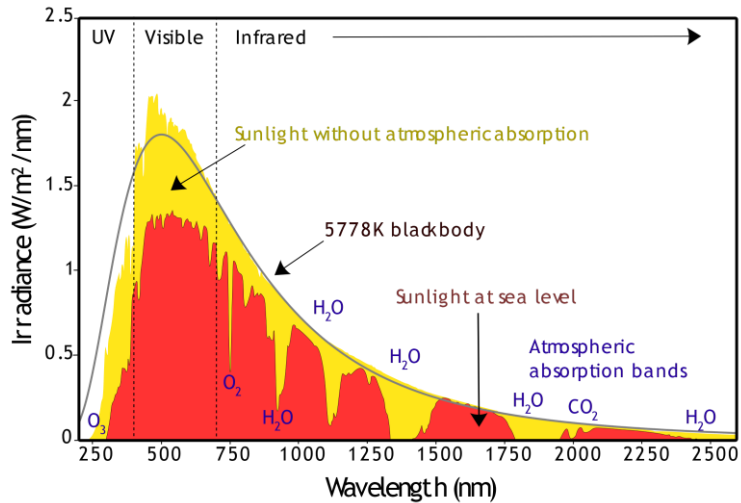


Figure 2-3. Solar irradiance spectrum above the atmosphere (yellow) and surface (red) [17].

2.1.2 Human perception of light

Color vision is defined as the ability to discriminate among stimuli based on their hue, independently of any other stimulus property, such as brightness or polarization [18]. It is an illusion

created by millions of interactions of neurons in the human brain. In the external world, color is a non-existent concept, since it is born of neuronal creation and is projected onto the world we observe. It is intimately related to the perception of form, where color facilitates the detection of the edges of physical objects, as can be seen in Figure 2-4.



Figure 2-4. Comparison of a black and white and color picture of a plant. If there is no color, it is much more difficult to distinguish the flowers from the rest of the plant.

Color is created using two properties of light: energy and frequency of vibration. The separation of these two properties and the recombination to form the brain's perception of color is an unknown that has been investigated for many years by scientists [19].

Also, like other mammals, the human eye has cells (neurons) that have nothing to do with image formation. These are the intrinsically photosensitive retinal ganglion cells, which are also located in the retina, but in the lower part, and are responsible

for regulating melatonin secretion or synchronizing circadian rhythms [20] [21].

Focusing on humans, vision is one of the five senses that humans must gather information about the world in which we live. The eye is the organ of vision. It is composed of a large number of components that allow light to enter its interior, with the objective of detecting light and converting it into electrochemical impulses that travel to our neurons, as can be seen in Figure 2-5. In humans, the eye is a complex optical system that collects light from the environment, regulates its intensity through the diaphragm, focuses through a set of lenses to form an image, converts the image into a set of electrical signals, and transmits these signals to the brain through the optic nerve.

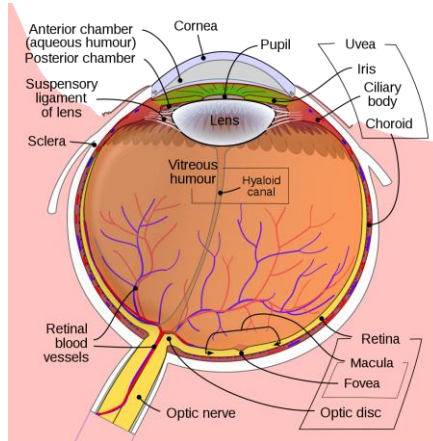


Figure 2-5. Schematic diagram of the human eye [22].

The retina is the part of the human eye that is most involved in the reception of light. It contains the photoreceptors, which are mainly divided into cones and rods. In each eye we have

approximately 100 million photoreceptors in the retina, 95% of which are rods and 5% are cones.

There are three distinct regimes of vision. Photopic vision, related to vision in high illumination, is mediated by cones. Scotopic vision is the vision of the eye under low light conditions and is mediated by the rods. Therefore, in low light conditions, the vision mechanisms are directed by the rods and objects lose color. Mesopic vision is the intermediate illumination between photopic and scotopic vision, generally given in conditions of low artificial illumination or in a dawn situation. In the latter both cones and rods are of similar importance. The limits of these three regimes are not entirely clear and depend on individual factors, such as the age of the subject, but some authors propose to set limits that depend on the illuminance, a parameter that is defined in the section 2.1.3. Mesopic vision can be defined in the range of 0.05 – 50 lux (the unit of illuminance), being in between scotopic and photopic vision [23].

The cones are located mainly at the center of the retina, in an area called fovea, a site where there are practically no rods. The density of cones decreases very rapidly as they leave this area. Rods, on the other hand, begin to appear from an angular separation from the center of the fovea. This allows them to act over a large visual angle [24]. With the information obtained from all those neurons, the brain is able to process it and construct an image.

Spectral sensitivity is key to understanding color detection and color formation. On the one hand, the sensitivity curve of rods

follows a Gaussian distribution centered at 507 nm, with a full width at half maximum (FWHM) of 100 nm, approximately. On the other hand, there are three types of cones: L cones, sensitive to large wavelengths (red); M cones, sensitive to medium wavelengths (green); and S cones, sensitive to short wavelengths (blue), always considering the visible range. Their sensitivity peaks are at range 564-580 nm, 534-545 nm and 420-440 nm, respectively [25].

The eye sensitivity describes the spectral sensitivity of human vision or, in other words, the sensitivity of the eye for different wavelengths and different conditions. Specifically, for photopic conditions, this function is generally referred to as the photopic eye sensitivity function, $V(\lambda)$. The Commission Internationale de l'Eclairage (CIE) established a standard for determining this function over the entire visible range, as can be seen in Figure 2-6.

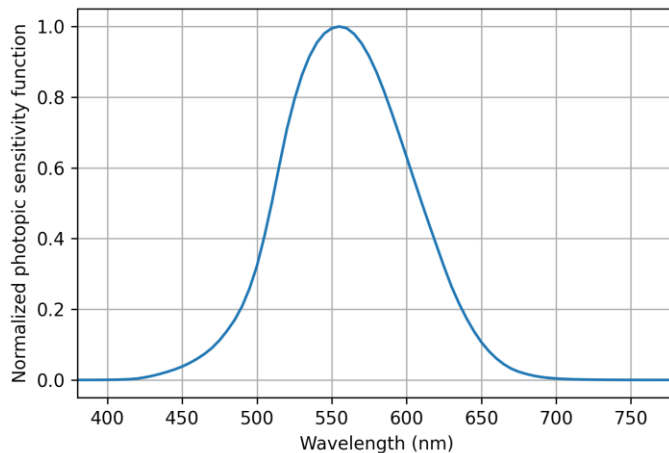


Figure 2-6. Photopic eye sensitivity function [26].

2.1.3 Photometric units

The physical properties of electromagnetic radiation are characterized by radiometric units. However, these units lose value when we want to talk about human perception. It must be borne in mind that the human eye cannot perceive radiation outside the visible range, so talking about radiation in general makes no sense when referring to human perception. To characterize light and color sensation, photometric units are used, which consider the characteristics of the human eye.

Radiant flux or optical power (P), in watts (W), emitted by a light source is given by Equation (2):

$$P = \int_{\lambda} P(\lambda) d\lambda \quad (2)$$

where $P(\lambda)$ is the spectral power density, or the power emitted per wavelength of a light source.

The luminous flux (Φ_{lum}) represents the power of a source perceived by the human eye, and its unit is the lumen (lm). In physical terms, 1 lumen is the luminous flux emitted by a monochromatic source at 555 nm with an optical power of 1/683 watts [14].

Mathematically, the luminous flux is obtained through radiant flux through the expression given in Equation (3):

$$\Phi_{lum} = 683 \frac{lm}{W} \int_{\lambda} V(\lambda)P(\lambda)d\lambda \quad (3)$$

where $V(\lambda)$ is the sensitivity function of the eye, and 683 lm/W is a normalization factor.

The illuminance (E) is the luminous flux incident per unit area, measured in lux ($\text{lux} = \text{lm}/\text{m}^2$), and is considered a SI unit used when characterizing lighting conditions. Reference values for outdoor daylighting and for different environments are shown in Table 2-2.

Table 2-2. Reference values for outdoor daylighting and for different environments [27] [28].

Illumination condition	Illuminance (lux)
Direct sunlight	100000
Office work	300 - 500
Educational tasks	300 - 750
Health care	100 - 1000
Full moon	0.1

The luminous efficacy of radiation (LER) of a light source is the conversion of optical power to luminous flux. It is measured in units of lumens per watt of optical power. Mathematically it is defined in Equation (4):

$$LER = \frac{\Phi_{lum}}{P} = \frac{683 \frac{lm}{W} \int_{\lambda} V(\lambda) P(\lambda) d\lambda}{\int_{\lambda} P(\lambda) d\lambda} \quad (4)$$

For monochromatic light sources, the luminous efficacy is equal to the eye sensitivity function $V(\lambda)$ multiplied by 683 lm/W. However, for extended sources, the calculation of luminous efficacy requires integration over all wavelengths.

The luminous efficiency (E) of a light source is the luminous flux divided by the electrical operating power, as can be seen in Equation (5). Its unit is lumens per electrical watt (lm/W), in the international system of units.

$$E = \frac{\Phi_{lum}}{W_{elec}} \quad (5)$$

Thus, luminous efficiency corresponds to the value of the ratio between the light flux emitted by a source and its power consumption. This parameter is very important in light sources working within the visible spectrum, since a source with a high value may imply energy savings with respect to other sources with lower values.

It is important to distinguish between the luminous efficiency and the LER of a light source. LER is defined as the ratio between the luminous flux and radiant flux, and its units are the same as energy efficiency, lm/W, which makes confusion relatively frequent. Because they have similar names, for the sake of clarification, we will call luminous efficiency energy efficiency.

2.1.4 Colorimetry

Colorimetry is the science and technology used to quantify and describe physically the human color perception [29].

The human sense of sight is very different from the sense of hearing. As humans, we can differentiate two or more frequencies sounding simultaneously, as might be a musical chord emitted by an instrument such as a piano or guitar. The sense of vision, on the other hand, is not capable of distinguishing simultaneous monochromatic signals. When two or more monochromatic signals are emitted, humans see only one color related to the signals, being unable to distinguish them separately.

Light causes different levels of excitation in the red, green, and blue cones of our eye. However, the color sensation and luminous flux caused by a particular light varies slightly in different individuals. Furthermore, color sensation can be considered a subjective quantity. For this reason, the CIE has worked to standardize the measurement of color in terms of color-matching functions and different chromaticity diagrams.

During the late 1920s, Wright and Guild independently experimented to determine whether there was any way to match colors by combining red, green, and blue light (RGB) [30] [31]. Their findings were used to create the CIE 1931 color space system. Observers were asked to adjust the three primary colors (red at 700 nm, green at 546.1 nm and blue at 435.8nm) until they created an RGB color combination that looked like the visible light spectrum shown sequentially. Using this

methodology, each color has its own intensity curve. Negative numbers indicate that one of the primary colors was needed to create the matching secondary color. These were later adopted by the CIE as the standardized RGB color matching functions denoted as $\bar{r}(\lambda)$, $\bar{g}(\lambda)$ and $\bar{b}(\lambda)$. The representation of these functions can be seen in Figure 2-7:

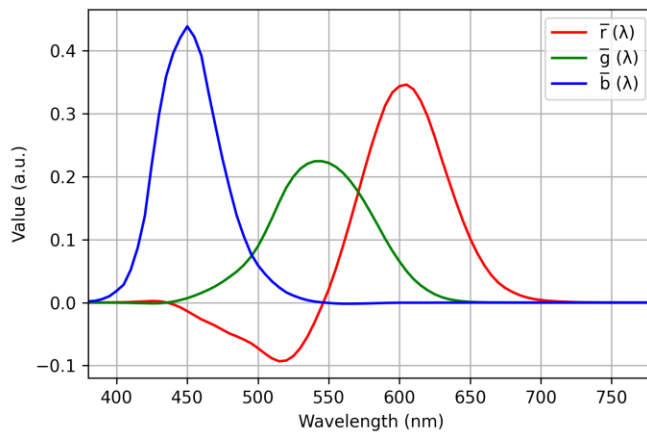


Figure 2-7. Color matching functions for the Wright and Guild data [24].

In 1931, the CIE redefined the RGB color matching functions by eliminating negative values. These transformations can be thought of as a linear transformation between two spaces. This new CIE 1931 XYZ color matching functions are denoted as $\bar{x}(\lambda)$, $\bar{y}(\lambda)$ and $\bar{z}(\lambda)$. The representation of these new functions can be seen in Figure 2-8:

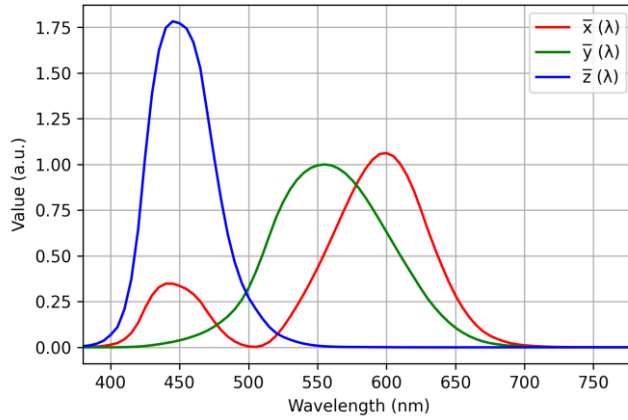


Figure 2-8. CIE 1931 XYZ color matching functions [32].

The stimulation of the primary red, green, and blue lights needed to match the color of a given spectral power density, $P(\lambda)$, are known as the tristimulus values. The three equations are defined in Equation (6), Equation (7) and Equation (8):

$$X = \int_{\lambda} \bar{x}(\lambda)P(\lambda)d\lambda \quad (6)$$

$$Y = \int_{\lambda} \bar{y}(\lambda)P(\lambda)d\lambda \quad (7)$$

$$Z = \int_{\lambda} \bar{z}(\lambda)P(\lambda)d\lambda \quad (8)$$

Therefore, the values of X , Y , and Z indicate, approximately, the red, green, and blue color of the given spectral power density $P(\lambda)$ [33].

Due to the fact that those three coordinates are contained in the plane $X + Y + Z = 1$, color can be expressed just using two coordinates.

Thus, the chromaticity coordinates (x, y) are calculated from the tristimulus values according to the expressions shown in Equation (9), Equation (10) and Equation (11):

$$x = \frac{X}{X + Y + Z} \quad (9)$$

$$y = \frac{Y}{X + Y + Z} \quad (10)$$

$$z = \frac{Z}{X + Y + Z} = 1 - x - y \quad (11)$$

Therefore, the value of the chromatic coordinate is the stimulation of each type of retinal cone divided by the entire stimulation ($X + Y + Z$).

The chromaticity diagram (x, y) is shown in Figure 2-9. The reddest and greenest colors are found at the large x and y values, respectively. The bluish colors are found at the large values of z , which corresponds to small values of x and y , close to the origin of coordinates of the chromaticity diagram. All colors can be characterized in terms of the location on the chromaticity diagram.

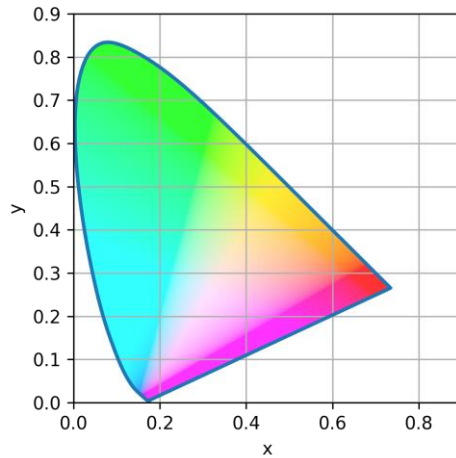


Figure 2-9. CIE 1931 chromaticity diagram generated using Luxpy library [34].

However, this diagram is very inconsistent in terms of color difference, since the mathematical distance between two points is not proportional to the color distance. For this reason, in 1976 the CIE incorporated several improvements to provide better uniformity to the chromaticity diagram [29].

Thus, the CIE 1976 uniform chromaticity scale diagram offers new coordinates (u', v') that can be calculated from the tristimulus values using following Equation (12) and Equation (13):

$$u' = \frac{4X}{X + 15Y + 3Z} \quad (12)$$

$$v' = \frac{9Y}{X + 15Y + 3Z} \quad (13)$$

This diagram, shown in Figure 2-10, provides a color difference proportional to the geometric distance between two points much more accurately than the CIE 1931 diagram.

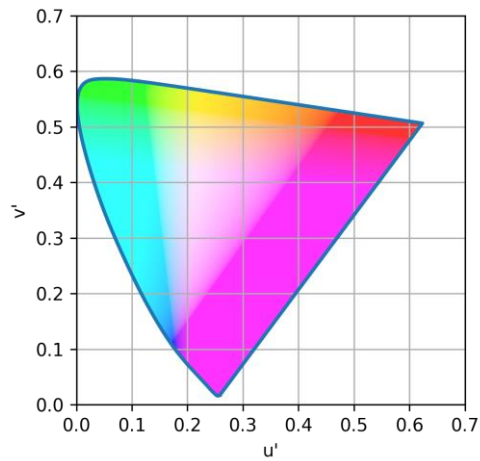


Figure 2-10. CIE 1976 uniformity chromaticity scale diagram generated using Luxpy library.

The equations relating both chromaticity diagrams are given by Equation (14), Equation (15), Equation (16) and Equation (17):

$$u' = \frac{4x}{-2x + 12y + 3} \quad (14)$$

$$v' = \frac{9y}{-2x + 12y + 3} \quad (15)$$

$$x = \frac{9u'}{6u' - 16v' + 12} \quad (16)$$

$$y = \frac{4v'}{6u' - 16v' + 12} \quad (17)$$

In both chromaticity diagrams, monochromatic light sources like lasers, which have a very narrow spectral width, are located on the perimeter of the chromaticity diagram. As an example, the emission coming from *monochromatic* LEDs seems monochromatic to the human eye, but they are not strictly monochromatic as their emission has a broadening of several tens of nanometers. Given this characteristic, *monochromatic* LED-sources do not lie exactly on the perimeter of the chromaticity diagram, although they are very close. When a source emits distributed light with a wider spectral width, the location of the chromaticity coordinates moves in the direction of the center of the diagram [35].

White light can be generated in many ways. Of all these forms, the blackbody radiation occupies a privileged and unique place because it has some special properties related to colorimetry.

The location of the blackbody radiation on the chromaticity diagram is called the blackbody locus or the Planckian locus. It is defined as the line connecting the chromaticity points of the series of absolute temperatures of black bodies [36]. In Figure 2-11 can be observed directly on the CIE 1931 and CIE 1976 chromaticity diagrams. As the blackbody temperature increases, the chromatic locus moves from the red sector of wavelengths in the direction of the center of the diagram. In addition, natural daylight approximates to a blackbody, and its temperature evolves over the day.

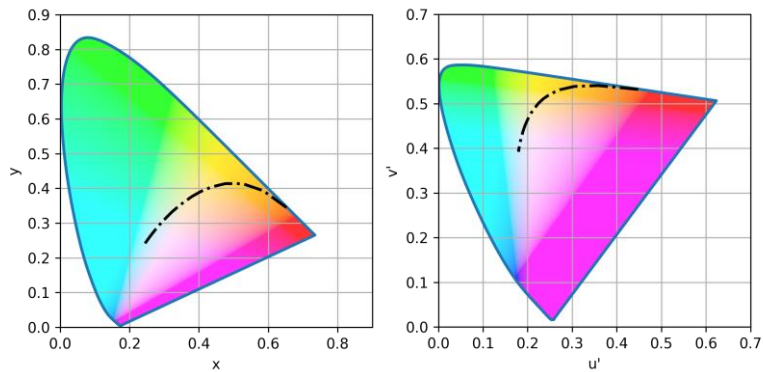


Figure 2-11. Situation of the Planckian locus in the CIE 1931 (left) and the CIE 1976 (right) chromaticity diagrams.

In the two chromaticity diagrams from Figure 2-11, the Planckian locus starts in the area near red, moves towards orange and yellow and ends in the white region. This sequence of colors corresponds to the colors of a black body in thermal equilibrium that is heated to high temperatures, indicating that real objects with certain temperature roughly follow the chromaticity of Planck's ideal black bodies.

The color temperature (CT) of a white light source is the temperature of an ideal black body (Planckian radiator) which emits radiation of the same chromaticity of the source [37]. Due to the fact that this CT is related to the real temperature of a black body, its magnitude in the international system is measured in Kelvins (K).

On the other hand, if the light source is not exactly on the Planckian locus, we speak of correlated color temperature. The correlated color temperature (CCT) of a white light source is the temperature of the Planckian radiator whose chromaticity is nearest to that of the source in a suitable uniform chromaticity-scale diagram [37]. In a similar way than the CT, their units are also Kelvins.

In order to determine the CCT, in terms of geometric distance in the uniform chromaticity diagram (u', v') , the point of the Planckian locus that is closest to the chromatic location of the test source is considered. Thus, the CCT is the blackbody temperature at this point. Figure 2-12 shows a dynamic white light source operating at different CCTs:

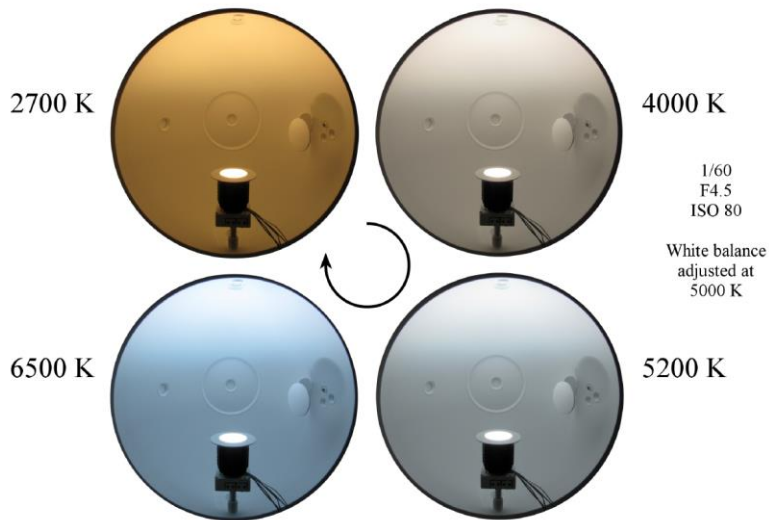


Figure 2-12. Dynamic white light source working at different CCTs.

CCTs below 3500 K are considered to correspond to warm whites, between 3500 and 4500 K to neutral whites and above 4500 K to cool whites. This division is subjective, since the eye can perform white balances to accommodate different spectra, but it can serve as a reference.

To describe the chromaticity of a lamp, either (x, y) or (u', v') coordinates can be used, although the industry has accepted to describe it using CCT. For this reason, it is very useful to define another parameter that complements CCT: Duv. Duv is an indication of the degree to which a lamp's chromaticity coordinate lies above the Planckian locus (positive Duv) or below it (negative Duv) [38]. As a reference value, according to the ANSI C78.377-2015 standard [39], Duv must be inside the ± 0.0060 range for warm LED light sources (CCT < 2870 K).

Color rendering

Additive mixing of two or more light sources is used in a very large number of applications. In LED displays, for example, three different types of LEDs (usually red, green, blue) are used. The colors are mixed so that the observer can experience a very wide range of colors.

For two different colors represented by two points on the chromaticity diagram, the mixed color is located on the straight line connecting the two points. Therefore, it is possible to create any color (including white) located between two points by balancing their relative intensities.

The area located within more than two points on the color diagram is called color gamut and represents all the colors that can be created by the different light sources. These colors lie within the perimeter of the formed figure. The ability to create a large variety of colors is a very interesting feature in displays, as a large color gamut ensures that bright and saturated colors can be created.

The color gamut represents the full range of colors that can be created through a series of light sources [40]. They are usually polygons positioned near the perimeter of the color chart. For the case of the three primary colors (red, green, and blue), the color gamut is a triangle, as can be seen in Figure 2-13:

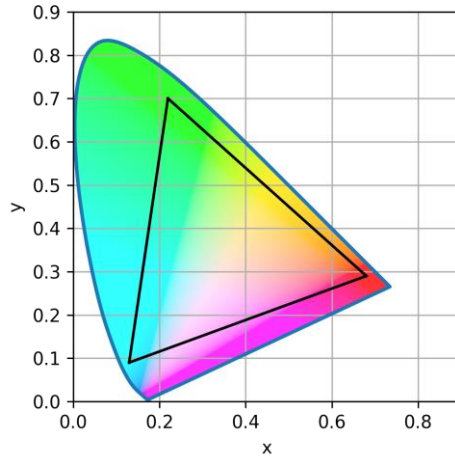


Figure 2-13. Example of the color gamut for a RGB LED display in the CIE 1931 chromaticity diagram.

Another important characteristic of light is their color rendering. The color rendering of a light source is the effect of an illuminant on the color appearance of objects by conscious or subconscious comparison with their color appearance under a reference illuminant [41]. In other words, color rendering can be defined as the ability to show the true colors of the objects being illuminated by a light source [42].

To quantify the color rendering, the CIE defined the General Color Rendering Index (Ra) as the average magnitude of the color appearance shift of a set of 8 standard colored samples (TCS) under a test and a reference illuminant. The reference illuminant is set as the source with optimum color rendering and any deviation from the color appearance under this reference is penalized. The reference is defined to be a blackbody radiator for

color temperatures under 5000 K and a daylight model for other cases. Ra maximum value is 100 and for lower values the difference from 100 is proportional to the average size of the color differences. As an example, a Ra value of 60 indicates that the average color difference is two times bigger than a Ra value of 80.

The calculation of Ra is done by simulation. The 8 TCSs are illuminated by the test source and then by the reference source. Mathematically, each source SPD is multiplied by each of the specified surface spectral reflectance functions of the TCSs. Then, for each TCS, their color appearance difference is calculated (measured as a Euclidean distance in the CIE 1976 chromaticity diagram) and finally, to get Ra , the values are arithmetically averaged [43].

Some typical CCT and Ra values for different light sources are shown in Table 2-3.:

Table 2-3. Examples of CCT and Ra values of different light sources [44] [45]. The LED values have been analyzed using a database that contains data of 963 commercial LEDs.

Light source	CCT (K)	Ra
Daylight (D65)	6500	100
Daylight (D50)	5000	100
Incandescent	2650	100
Fluorescent (warm white)	2940	83
Fluorescent (cool white)	4290	63
High pressure sodium lamp	2070	20
White LED	2200 - 6500	70 - 98

Ra metric is widely adopted in the industry and in many standards and specifications. However, this metric has been suffering from some well-known deficiencies, such as few TCSs, an outdated chromatic adaptation transforms, a nonuniform color space, and confusing negative scores [46]. For this reason, new metrics were developed.

In 2015 the Illuminating Engineering Society (IES) developed a technical memorandum where they try to improve the quantification of color rendition using a statistical approach. In this memorandum, there are parameters related to color fidelity, gamut area and hue-specific properties.

The procedure to follow is equivalent to the calculation of Ra : comparing the appearance of a set of color samples as rendered by a test light source and a reference illuminant, quantified with a model of human vision. In this case, the reference illuminant is

a Planckian radiator if CCT is below 4000 K, a mixture between a Planckian radiator and a daylight model between 4001 K and 4999 K, and a daylight model from 5000 K onwards. Another important difference is the number of TCSs, which in this case are a set of 99 components representing a very important variety of objects, materials, skin tones, paints, or flowers, among others. In addition, in this case an updated uniform color space, CAM02-UCS, is used, which ensures greater uniformity [47].

This technical memorandum has a lot of output parameters, and we will focus on Rf and Rg , which represent the average values of color fidelity and color gamut, respectively. Rf and Ra parameters have obvious theoretical similarities, so that in many cases we can find similar values for the same light source. In Figure 2-14 there is a comparison of Rf and Ra for a database containing information on 963 commercial LEDs.

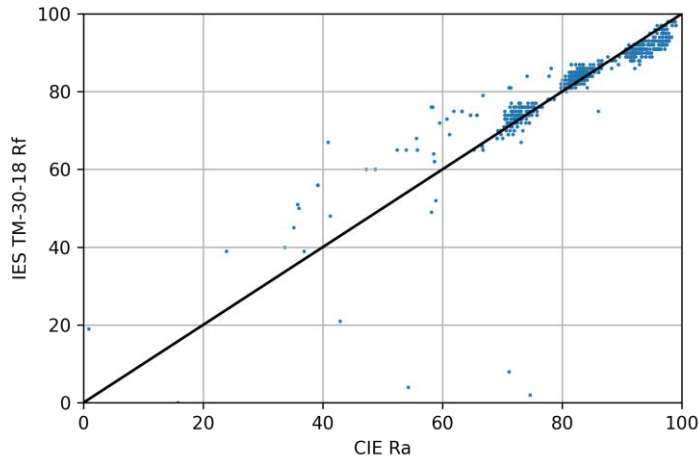


Figure 2-14. Comparison between Rf and Ra values of 963 commercial LEDs. The diagonal black line serves as a reference to visualize the difference between Rf and Ra .

This technical memorandum has been updated with minor changes, so that in this case the IES TM-30-18 version is used. The development of this memorandum has been well adopted in the industry, and currently there are companies that manufacture LEDs and light sources that are already using it in their products.

2.1.5 Circadian parameters

In 2001, a research group discovered that inside our eye, besides the cones and rods, there were other types of photoreceptor cells that had not been discovered until then [48]. These cells are called intrinsically photosensitive retinal ganglion cells (ipRGCs). Their spectral and temporal response is different from cones and

rods, as they are more sensitive to blue light and act in the long term [49]. These cells are connected to the suprachiasmatic nucleus, known to be the master circadian pacemaker in mammals [50]. Figure 2-15 shows the difference in the sensitivity of the photopic and circadian curves:

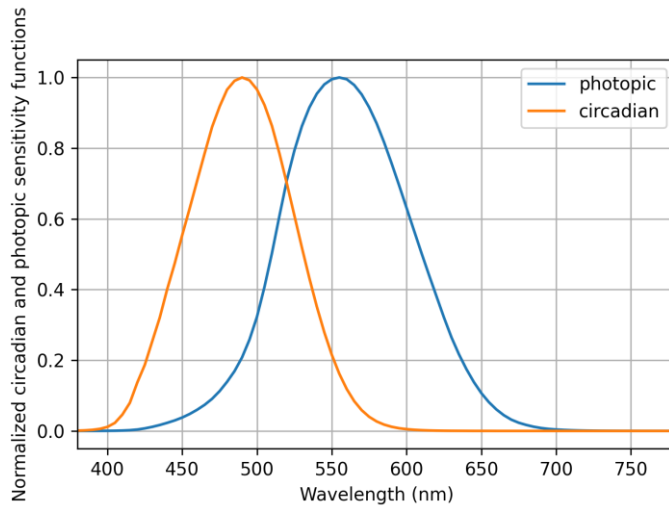


Figure 2-15. Difference between circadian (orange) and photopic (blue) sensitivity functions [51].

The human circadian system is directly related to the temporal cycles of some physiological processes such as body temperature variations, metabolism, sleep/wake cycles or secretion of hormones such as melatonin. Its role in regulating all these physiological processes means that the circadian system is considered an important agent linked to human health and well-being. [52].

There are different technical parameters that relate exposure to lighting to circadian system impairment. These include the

equivalent melanopic lux (EML), the melanopic equivalent daylight illuminance (mEDI) or the circadian stimulus (CS), and all of them, apart from the spectral shape, also depend on the illuminance level.

EML is a proposed metric that is weighted to the ipRGCs instead of to the cones' response, which is the case with traditional lux. It is the circadian parameter adopted by the WELL Building Standard, dedicated to the concept of building designs that promotes healthy environments for living, working, learning and play [53]. As an example, in living environments, during the daytime, at least 200 EML lux measured facing the wall in the center of the room at 1.2 m above the floor are required. However, during the nighttime, lights must not provide more than 50 EML lux as measured 0.76 m above the floor [54].

Equation (18) shows the relation between EML and illuminance. If we divide the EML by the illuminance we get the melanopic/photopic ratio (M/P ratio), that can be defined as a comparison as the melanopic (related to ipRGC) potential to the light source's ability to produce light for daytime detail (photopic) vision.

$$EML = (M/P \text{ ratio}) \cdot E \quad (18)$$

There are four different methods for calculating the M/P ratio. In this case we use the following procedure, used by the WELL Building Standard v2 [55]:

- Take the measured SPD values.
- Multiply the value of the SPD at each wavelength by the value at the same wavelength of the melanopic weighting function normalized so that its area under the curve equals 1 when evaluating the equal-energy spectrum. Sum the values to get melanopic radiant power.
- Multiply the value of the SPD at each wavelength by the value at the same wavelength of the photopic weighting function normalized so that its area under the curve when evaluating an equal-energy spectrum is 1. Sum the values to get photopic radiant power.
- Divide the summed melanopic radiant watts by the summed photopic radiant watts. This gives you the M/P ratio.

The other two parameters (mEDI and CS) also try to estimate the potential melanopic contribution to lighting in a similar way. In the case of mEDI, it has been adopted by the CIE, while CS has been adopted by Underwriters' Laboratories (UL) and the Lighting Research Center (LRC) [56]. In addition, there is no direct conversion between CS and EML or MEDI, as can be seen in Figure 1-16:

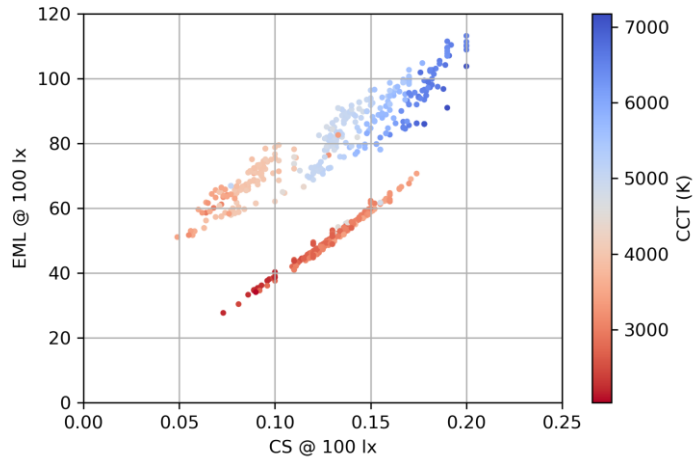


Figure 2-16. Relationship between EML and CS (both at 100 lx) for 723 commercial white LEDs. The data have been obtained from information provided by the manufacturers.

2.1.6 LED luminaires

There are currently a very large number of LED luminaires available on the market with different electrical, luminous, or colorimetric properties. This section explains the basic elements that make up LED luminaires, such as the LED diode itself and the Printed Circuit Board (PCB) containing the LEDs, the driver, the heatsink and the optical reflection and diffusion elements.

LEDs

Solid-state light-emitting (SSL) devices can generate light in the visible, ultraviolet, and infrared range using electroluminescence, which is the emission of photons in response to an electric

current. When a semiconductor diode is switched on, electrons flow from the cathode to the anode, whereas holes flow from the anode to the cathode. When a free electron in the conduction band and a hole in the valence band reach the intrinsic region of a P-N junction, they can recombine radiatively, giving their excess of energy to the creation of a photon. LEDs are the most common type of SSL devices, and they can be divided into inorganic or organic semiconductor materials.

The first high-efficiency LEDs were developed in the 1960s, based on materials such as gallium arsenide (GaAs) or gallium phosphide (GaP), among others, which could produce infrared radiation and red or green light, however with luminous efficacies quite poor (below 10 lm/W) [57]. In the 1990s a very important milestone for LED technology was achieved: the creation of a blue LED that, combined with a phosphor, was able to create white illumination for lighting purposes. This combination is still used today, as it allows decent colorimetric properties to be achieved along with very high efficiency [58]. Figure 2-17 shows the schematic operation of an LED:

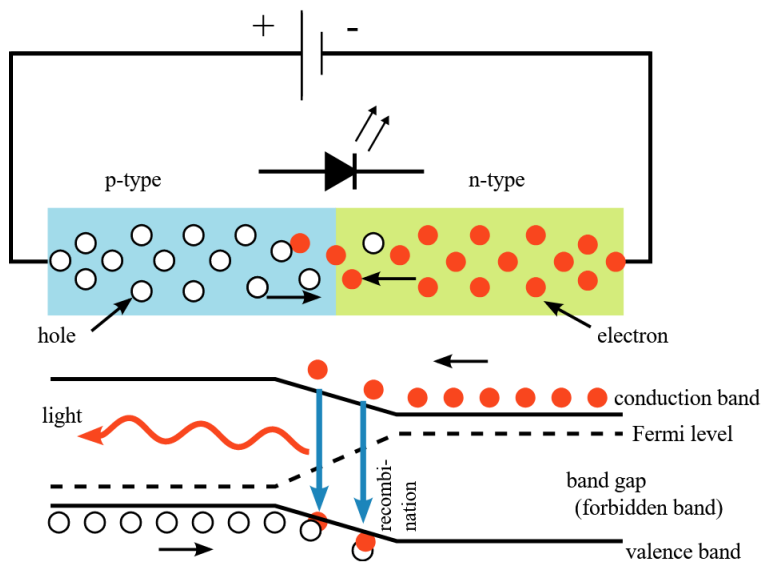


Figure 2-17. Schematic of an LED [59].

In the industry, an LED is presented as a package containing the LED itself well protected in a housing with terminals ready to be connected to electrical power means. If the LED is white, the package itself already contains the phosphor needed to make the down-conversion of photons from blue to the rest of the visible spectrum (i.e., emitting white light).

There are packages of different sizes, ranging from 1 mm to a few centimeters. In terms of electrical potential differences, they generally range from about 2 V to several tens. In terms of electrical current, they can range from a few milliamperes to a few amperes. Figure 2-18 shows various LED packages:



Figure 2-18. Different LEDs presented in different packages [60].

In lighting-related applications, multiple LEDs are usually soldered onto a PCB to be used in combination, as can be seen in Figure 2-19. Connections are made in series and/or in parallel, depending on the electrical characteristics needed. In addition, some elements such as resistors, capacitors or inductors can be incorporated to adjust values such as potential drop or electrical current through them.

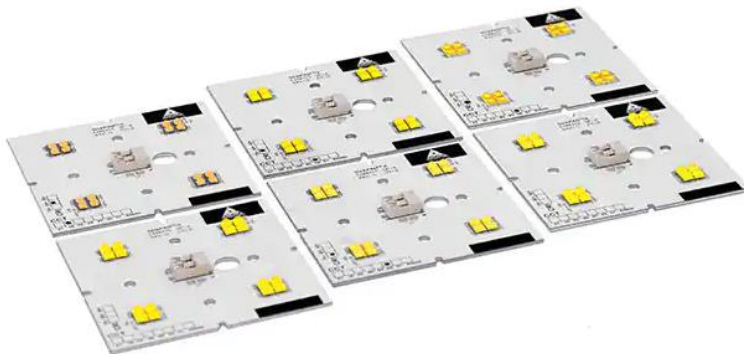


Figure 2-19. Example of an LED PCB [61].

Drivers

LEDs are devices that emit a certain amount of light depending on the electrical current flowing inside them. The electrical current circulating inside them, like any ideal diode, depends exponentially on the potential difference supplied, as shown in

Figure 2-20. This means that the electrical current circulating inside the diode must be carefully controlled, since small variations in the potential difference can lead to large changes in the electrical current circulating inside the diode.

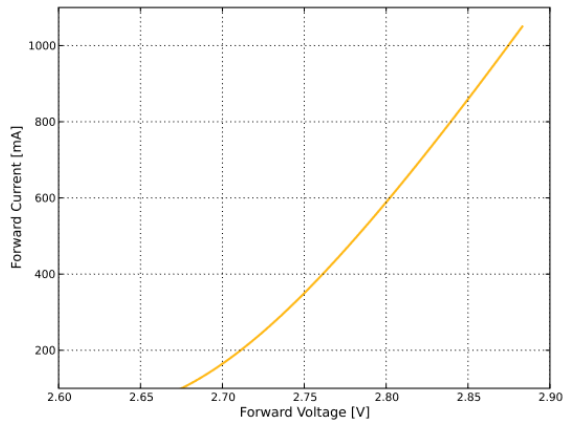


Figure 2-20. Typical forward current vs. forward voltage for LUXEON C PC Amber [62].

There are mainly two ways to dim the light of an LED in a simple way: by varying directly the electrical current or by using Pulse-Width Modulation (PWM).

Using the variation of the electric current it is possible to dim an LED, since more or less current is traduced into higher or lower luminous flux. However, LEDs do not have a completely linear response with electric current, so this approach will not always be valid if we are looking for precision, as can be seen in Figure 2-21.

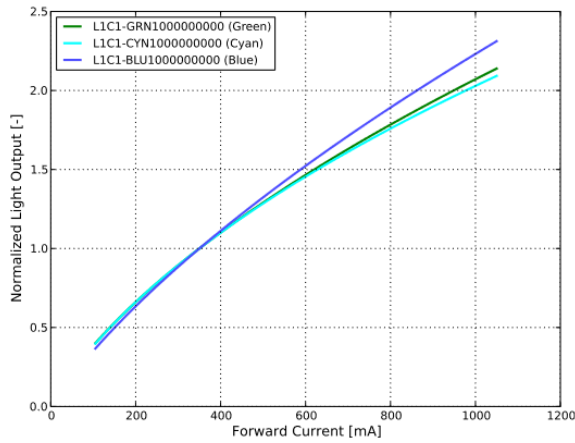


Figure 2-21. Typical normalized light output vs. forward current for LUXEON C Green, Cyan and Blue [62].

On the other hand, PWM is characterized by allowing the control of the amplitude of a periodic and square-shaped electric pole. By controlling the periods duty cycle, it is possible to control the total power delivered on the LED and, thus, its average emission. Normally the frequency of the pole is much higher than the resolution frequency of the human eye, being useful for controlling the light intensity of LEDs. PWM guarantees a correct attenuation of an LED, preserving the linearity in a much more precise way. Figure 2-22 shows a square-shaped wave, example of PWM:

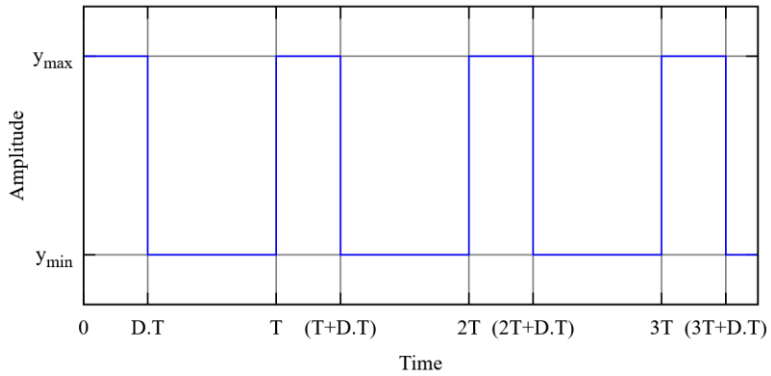


Figure 2-22. A square-shaped wave, example of PWM [63].

Heat sink

A heat sink is an external heat exchanger that transfers heat from an electronic device to a liquid medium, where it is dissipated away from that device. Applied to lighting, heat sinks disperse excess heat from the LED.

Heat dissipation in an LED is critical to preserve the efficiency and lifetime of the device. In general, the lifetime of an LED can be more than 35,000 hours, although after a few thousand hours of operation it usually begins to emit significantly less luminous flux. Choosing the right heat sink is a complex task and sometimes simulation software is used [64].

A heat sink is designed to maximize its surface area in contact with the surrounding medium, usually the air. The most determining parameters that define them are the material of manufacture (usually metals), the design, the air velocity, or the thermal adhesive with which the heat sink is coupled to the

integrated circuit containing the various LEDs. Figure 2-23 shows different types of heat sinks:



Figure 2-23. Different types of heat sinks [65].

Thermal resistance determines the choice of a suitable heat sink. The heat flow between the semiconductor and the ambient air can be modeled through a series of thermal resistances, resulting from the sum between the semiconductor and the LED package, between the package and the heat sink, and finally between the heat sink and the air. The sum of these resistances is the total thermal resistance, which is defined as the temperature rise per unit of power, analogous to the electrical resistance. This magnitude is typically obtained in degrees Celsius per watt ($^{\circ}\text{C}/\text{W}$). Thus, if the heat dissipation of the device and the total thermal resistance are known, the temperature rise of the semiconductor with respect to air can be calculated. Obviously, these calculations are valid in a moderate range of temperature, as the linear approximation (sum of resistances) is no longer valid when nonlinearity of convection effects appear, that may affect the temperature rise or temperature changes over time.

Optical components

To have absolute control over the light emitted by a luminaire it is important to consider the optical elements that allow manipulating the direction of the outgoing flux in a practical and efficient way.

A reflector is a surface reflecting optical element that allows to have a directional control of the light. They are typically attached to a light source and their purpose is to shape the light reflected from it. There are many different types of reflectors, but they are all based on a parabolic reflection pattern and are usually made of aluminum, due to its high reflectance and low weight. Figure 2-24 shows different types of reflectors:



Figure 2-24. Different types of reflectors [66].

On the other hand, a diffuser is an optical element of light diffusion that is responsible for smoothing the outgoing flow of the luminaire. Its purpose is to abandon the punctuality offered by LEDs, creating a more extensive light source. In some designs, diffusers are combined with lenses for a higher dispersion of light (in this case, lenses are placed at their focal distance to the LEDs for generating parallel rays). Different types of optical diffusers are shown in Figure 2-25:



Figure 2-25. Different optical diffusers used in linear lighting [67].

There are many different types of luminaires, including downlights, floodlights, linear luminaires, or simple bulbs. For each different luminaire model there will be its own light pattern. The light pattern or photometric distribution shows the angular dependence of the luminous flux of a light source. Depending on the design of the luminaire, these patterns can distribute the light as appropriate, providing direct light or indirect light. Direct light is considered to be a luminous flux that is emitted within a cone, illuminating a limited area. Indirect light is light that typically comes from reflections or points in directions spread out in space. Classically, light patterns were defined by diffuser elements since classical luminaires do not have versatility in the configuration of light-emitting devices. Today, two luminaires with similar optics can have very different radiation patterns since the arrangement and patterns of individual LEDs can critically affect the overall radiation pattern. As might be expected, there are commercial LEDs with very different photometric distributions, expanding the number of design and implementation possibilities for new light distributions.

2.1.7 Multichannel LED light sources

A variable spectrum light source has a unique ability to change the emission spectrum to adjust it to some specific lighting parameters, such as CCT, M/P ratio or Ra , among others. Before the advent of LEDs there were primitive forms of spectral control combining several technologies, such as fluorescent and incandescent bulbs [68]. These techniques offered few options and were highly inefficient, so they did not prosper in their implementation. The invention of these monochromatic and polychromatic light emitters, and their combination, has brought a real revolution in this field.

There are simple applications of polychromatic light sources that just combine the primary colors in a way that is visually attractive, with variations of their spectrum over time (for instance, the lights of a Christmas tree). However, variable spectrum sources offer a dynamic variability of illumination that goes far beyond simple decorative purposes. With the development of these LED luminaires, a new possibility has emerged: to modulate lighting parameters at will, with important implications in colorimetry and an important impact in health. Figure 2-26 shows an example of a compact 5-channel LED strip:



Figure 2-26. Example of a compact 5-channel LED strip (red, green, blue, warm white and cool white) commercialized by Samsung [69].

One of the most interesting possibilities of these systems is the production of metamers. The metamerism is the perceived matching of colors with different nonmatching SPDs [70]. Colors that match this way are called metamers. If two light sources with different spectra are directly observed, it is possible to perceive the exact same color if they are metamers. However, they can deliver different light properties, such as Ra or M/P ratio and they can have different energy efficiency. An example of metamer generation in a multichannel light source is shown in Figure 2-27:

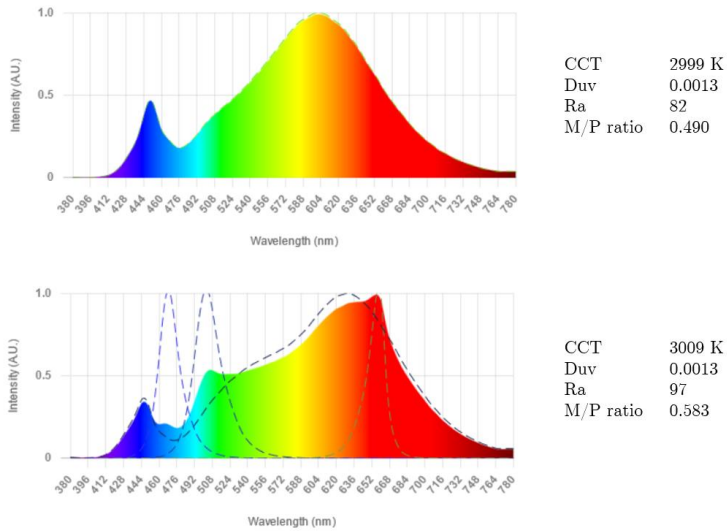


Figure 2-27. Production of metamers using Kumux platform [71]. In the first case, the system is composed of a single 2999 K warm white LED with a Duv of 0.0013. In the second case, the system is composed of a red, a cyan, a blue and a warm white which, combined together, can provide a CCT of 3009 K with a Duv of 0.0013. In both cases a standard observer will not be able to distinguish the color of the two light sources, although they have different Ra and M/P ratio parameters.

In addition, outside the world of general lighting applications, these sources have many possible applications. Within the medical field, for example, it can be used to investigate the improvement of some dermatological conditions [72] or seasonal affective disorder [73]. Outside the visible range, with the incorporation of ultraviolet LEDs, these luminaires can develop disinfection functions [74] and with the incorporation of infrared LEDs they can be transformed into information communication and data transmission devices without wiring [75]. They are also

of interest in the world of horticulture [76], since they can simulate situations to stimulate the productivity of plants.

These luminaires are composed of different channels of LEDs, connected to current drivers that allow the dimming of each channel independently. The choice of the different types of LEDs depends mainly on the intended use of the luminaire. For decorative purposes it may be sufficient to have only RGB LEDs, since they can reproduce a very large number of colors, as seen before. For lighting purposes, it would be interesting to incorporate more channels, since the maximum Ra that an RGB lighting system can provide is usually below the indoor lighting regulation [27]. If a high luminous flux with good energy efficiency is also desired, the use of wide-spectrum white LEDs is highly recommended. On the other hand, for applications where only CCT modulation is required, it is possible to have only two channels of warm and cool white LEDs. Thus, a combination of white and monochromatic LEDs can provide very large spectrum versatility, allowing to achieve spectra with very high Ra and very high range of CCTs [77]. Finally, by covering the entire spectrum with monochromatic LEDs, applications can be developed to simulate spectra with complete freedom (however, compromising their energy efficiency) [78]. Figure 2-28 shows a multichannel light source specifically designed for horticulture applications:



Figure 2-28. Multispectral horticultural luminaire by Valoya [79].

2.1.8 Sensors, spectrometers, and microcontrollers

Until a few years ago, the technology available on the market to create new lighting solutions was quite limited. The market was dominated by technologies (incandescent, fluorescent, sodium, etc.) that allowed no spectral control, or very few possibilities. However, with the emergence of LEDs for general lighting applications, a very large number of possibilities arose, and they are still under investigation.

Apart from the development of light sources, another field that has been arising is the sensor sector, as they can be connected to luminaires to improve performance or create behaviors based on collected data. According to the Oxford Dictionary, a sensor is a device that can react to light, heat, pressure, etc. in order to make a machine, etc. do something or show something [80]. Applied to lighting, the information collected from a sensor can

be used to control a luminaire by either dimming the light output or changing the spectral properties of the light.

In particular, a color sensor is an array of integrated light sensors that typically includes both RGB and XYZ light sensors for precise color measurement, determination, and discrimination. XYZ sensors are capable of providing chromaticity coordinates, or CCTs and Duvs. Typical color sensors measure 3 different bands inside the visible range, although in some cases it can reach almost 20 different bands inside and outside of the visible range [81]. A schematic of the difference between a color sensor and a spectrometer can be seen in Figure 2-29:

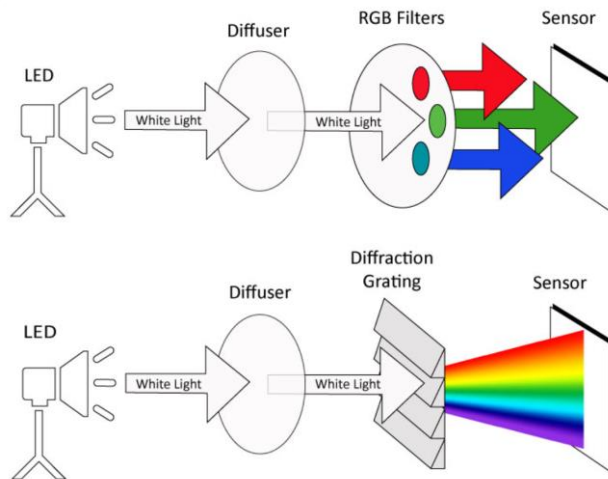


Figure 2-29. Typical operation of a color sensor (top) and a spectrometer (bottom). Normally, the spectrometer obtains a wavelength resolution unattainable for a color sensor [82].

Nevertheless, with the information of some discrete bands of the analyzed spectrum, a color sensor does not provide accurate

information about the whole spectrum of a light source. Due to the fact that color sensors cannot provide accurate information on some more advanced colorimetric parameters (such as Ra or Rf) a spectrometer is needed. A spectrometer is a much more precise device for measuring light intensity as a function of wavelength and can reach typical resolutions of 1 nm (advanced spectrometer can achieve resolutions as good as 0.05 nm). Figure 2-30 shows a photograph of a portable spectrometer.



Figure 2-30. UPRtek MK350S premium calibrated portable spectrometer [83].

For processing all the collected data from those color sensors and actuate over the light sources, a processing unit is necessary, either a computer or a small microcontroller. In this context, a

microcontroller is a small computer on an integrated circuit that consists of a processor, a memory and input and output units. They are specially designed for applications related to autonomous systems that require a minimum of computing power, so they are necessary for any system that uses sensors or actuators. They are usually small in size and low in cost, so they are widely used for digital control of devices. In the case of smart lighting, a microcontroller is an indispensable element if we want to provide a minimum of intelligence to the light source, since it acts as the *brain* of the lighting system, controlling many operations. Figure 2-31 shows a microcontroller in two different versions.

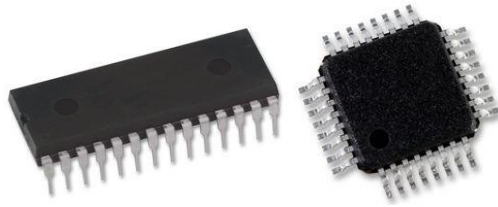


Figure 2-31. ATMEGA328 microcontroller in two different versions [84].

2.2 Algorithms

An algorithm is the step-by-step unambiguous instructions to solve a given problem. In the traditional study of algorithms, there are two criteria for evaluating the merits of an algorithm: correctness and efficiency. Correctness is related to solving the problem in a finite number of steps, while efficiency is about solving how many resources are needed, in terms of memory and execution time [85].

In the lighting world, algorithms have been employed for a long time. There are simulation algorithms that allow calculating the illuminance level in a plane, depending on the luminaire and contour parameters, such as the room furniture or the contribution of natural light [86]. Other algorithms allow simulating the angular distribution patterns of luminaires considering the LED aperture and the lenses used [87]. There are many different examples that can be implemented for different specific applications.

One of the cases under study are spectral simulation algorithms for lighting systems with more than one channel. These algorithms can help find the luminous intensity of each channel to optimize colorimetric, non-visual or energy efficiency parameters. Depending on the problem to solve, different algorithms can be employed, as discussed in the following sections.

2.2.1 Classical optimization algorithms

There are numerous algorithms that can be used for spectral optimization in multichannel luminaires. Genetic algorithms based on spectral shaping have been applied for the design of a circadian-tunable luminaire which also outputs white light with high Ra , Rf and LER [88]. Also, differential evolution algorithms have been used to produce CCT optimizations considering colorimetric, and illuminance constraints [89]. For other similar spectral optimization applications, such as SPD matching, other algorithms can be used, such as Monte Carlo or simulated annealing [90].

However, in these cases we are faced with a unique solution that allows obtaining a local maximum or minimum that fulfills some specific parameters. For obtaining more general solutions, brute force algorithms can also be used. These types of algorithms allow obtaining solutions based on absolute maxima given a certain resolution, obtaining a large number of results along the way. Their operation applied to a multichannel light source will be explained later, as well as the combination with other optimization algorithms.

2.2.2 Machine learning and neural networks

Machine Learning (ML) is a subfield in artificial intelligence (AI) with the goal of developing algorithms capable of learning from data automatically. Techniques in ML tend to be more focused on prediction rather than estimation and tend to be applied to

more complex high-dimensional problems than those typically encountered in a classical statistics course [91].

The general goal of ML is to recognize patterns in data, which inform the way unseen problems are treated. There are many examples of systems that today use ML to achieve concrete results. Among them, there are systems where a lot of information is received from sensors, being able to evaluate parameters that are difficult to quantify by other means (such as the danger when a computer is piloting an autonomous car).

In parallel to the growth of ML in the industrial sector, there is a growing interest in the scientific field. In both cases, there is a concern to design new models related to data acquisition and analysis to predict the behavior of complex systems. ML provides the necessary intelligence to create models extracted from data. Although sometimes it can be a powerful tool, the resulting models and data patterns are opaque from the point of view of a researcher's understanding [92].

It is possible to define three large classes of learning problems: supervised, unsupervised and reinforcement learning. In this doctoral thesis, we will focus on supervised learning, where the input data can be related to a label. The goal of supervised learning is to correctly approximate the label when a new data is entered into the model.

One can define a set of n samples, such that each sample follows the criteria $X_\mu \in \mathbb{R}^p$, where $\mu = 1, \dots, n$. To each sample X_μ we assign a label $y_\mu \in \mathbb{R}^d$. In this case, the objective will be focus on

finding a function f that can approximate a correct label to a new sample X_{new} . The dataset $\{X_\mu, y_\mu\}_{\mu=1, \dots, n}$ is called training subset.

In addition to the training subset, normally two extra subsets are also created: validation and test. In this case, the training subset is used to allow learning the function f , while the validation and test subsets are used to evaluate the function f while it is training and once a solution has been obtained, respectively.

The training process is determined by the loss function $\mathcal{L}[f_w(X_\mu), y_\mu]$ for each sample μ , where $w \in \mathbb{R}^k$ are the parameters (called weights) that express the function f . The loss function is small when the similarity between $f_w(X_\mu)$ and the label y_μ is large, and vice versa. The mean value of the loss function for the training set is known as the empirical risk, as shown in Equation (19):

$$\mathcal{R}(f_w) = \sum_{\mu=1}^n \frac{\mathcal{L}[f_w(X_\mu), y_\mu]}{n} \quad (19)$$

In the training process, the weights are adjusted so that, in an ideal case, the value of the empirical risk is smaller and smaller. To avoid cases of overfitting, where at a certain point the function simply memorizes the training subset through successive iterations, the validation subset is used. While the function f is learning, the empirical risk values of the two subsets (training and validation) are obtained. In this way, it is possible to see the behavior of both loss functions and to validate in parallel the

output in a subset that has had nothing to do with the training process, having the parameters linked to the error and correctness in a controlled way. To avoid overfitting, it is necessary that the loss value of the validation subset does not grow while the loss value of the training subset decreases, as this would mean that the training is only valid for the training subset, not being generalizable to other datasets. Finally, the test subset is used to check that the error distribution is similar to that of the training and validation subsets.

Typically, gradient descent (GD) algorithms are used to minimize the value of the empirical risk. This algorithm adjusts the weights iteratively in the direction of the gradient of the empirical risk, as shown in Equation (20):

$$w^{t+1} = w^t - \gamma \nabla_w \mathcal{R}(f_w) \quad (20)$$

where γ is the learning rate, a parameter that can be adjusted according to the problem to be solved and the loss values over the iterations during the learning process.

There is a widely used variant of GD: the stochastic gradient descent (SGD), where the empirical risk function \mathcal{R} is replaced by the contribution of a random subset of samples. There are many variants of the SGD algorithm and it is generally used to increase the efficiency with respect to a GD algorithm, achieving faster iterations [93].

In a regression task, the objective is to learn a function with real values. The accuracy, typically, is related to the value of the

mean-squared error (MSE) between the labels y_μ and the predictions of the function $f_w(X_\mu)$. One of the most widely used regression tasks is linear regression, where the function $f_w(X)$ is parametrized as $f_w(X_\mu) = X_\mu \cdot w$. However, in supervised machine learning, there are other techniques that have been a real revolution, such as artificial neural networks (NN).

There are several types of NNs and, although the basic principles are very similar among them, we will focus on the so-called feed-forward NNs. A NN behaves as a universal approximator, which means that it can perform an arbitrary mapping between two vector spaces of different dimensionality. The main advantage is that they can use unknown information hidden in the data and to generate a function f that relates the input samples X_μ to the output labels y_μ . In this case, the NN training process is related to the process of capturing the unknown information hidden in the data.

A NN consists of neurons, which are arranged in layers, as shown in Figure 2-32. The first layer is called input layer and the last layer is called output layer, while the intermediate neuron layers are called hidden layers.

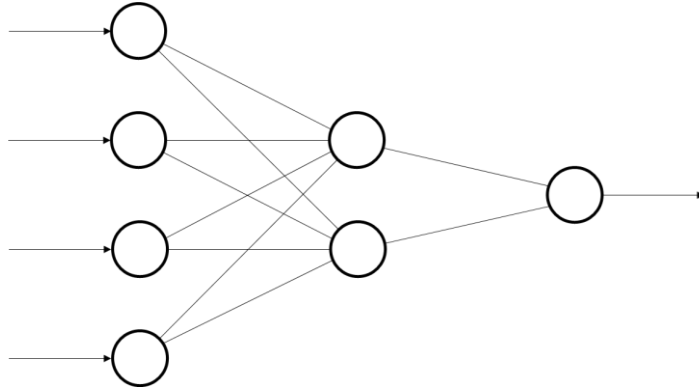


Figure 2-32. Diagram of a NN consisting of 4 neurons in the input layer, 1 hidden layer consisting of 2 neurons, and an output layer with a single neuron.

In the case of fully connected NN, each neuron in each layer is connected to all neurons in the next layer. The connection between the i th neuron and the j th neuron is characterized by a weight coefficient of w_{ij} , and the i th neuron will also have a bias coefficient b_i . The weight coefficients mark the importance of a connection in an NN. The output value (activity) of the i th neuron, x_i , is determined by the Equation (21) and Equation (22):

$$x_i = g(z_i) \quad (21)$$

$$z_i = b_i + \sum_j w_{ij}x_j \quad (22)$$

where j are all predecessors of the i th neuron, z_i is the potential of the i th neuron and the function $g(z_i)$ is the so-called activation function [94].

An activation function is used, within the context of NNs, to transform an input signal into an output signal which, in turn, is used as an input signal in the next layer. There is no rule specifying which activation function is necessary to use in each case [95]. There are different types of activation functions. Some are widely used in classification problems (sigmoid and hyperbolic tangent, for example) and others in more general problems (rectified linear units, also known as ReLu, for example). ReLu functions help to increase the efficiency of the training process, compared to sigmoid and hyperbolic tangent, in general converging faster [96].

The definition of the ReLu function is defined by the Equation (23):

$$g(x) = \begin{cases} x & \text{if } x \geq 0 \\ 0 & \text{if } x < 0 \end{cases} \quad (23)$$

Focusing the attention on the NN, and supposing a fully connected NN with a number of layers L defining its depth, generally speaking the function $f_w(X_\mu)$ is parameterized as the Equation (24):

$$f_w(X_\mu) = g^{(L)} \left(W^{(L)} \dots g^{(2)} \left(W^{(2)} g^{(1)} \left(W^{(1)} X_\mu \right) \right) \right) \quad (24)$$

where $W^{(i)} \in \mathbb{R}^{r_i \times r_{i-1}}$ with $r_0 = p$ and $r_L = d$ are the matrices of weights, and r_i for $1 \leq i \leq L - 1$ is called the width of the i th hidden layer. The functions $g^{(i)}, 1 \leq i \leq L$ are the activation functions [92].

The number of nodes (neurons) of the input and output layers are determined by the input and output dimensions of the function we are creating. However, as with activation functions, the number of hidden layers and hidden neurons in each layer is an open problem that has no clear solution. There are several theoretical results that claim that an NN with two hidden layers can approximate any arbitrary nonlinear function. There is no rule that can be applied to know how many neurons each hidden layer must have, but experience has shown that using a simple NN is better than a very complex one if the results are similar, especially in terms of efficiency. Choosing the dimensions of a NN is considered something of an art [97].

Unlike classical optimization algorithms, ML has not penetrated with the same importance in the lighting world. For example, there are scientific articles linking the use of NNs with lighting to predict the spectral behavior of LEDs when subjected to different electrical currents and thermal variations [98], but there are no commercial tools or particular practical cases where this technology is used to perform calculations related to light emission or sensing. In this case, in Chapter 5 we will study the possibility of using ML and NNs to increase the resolution of a multichannel colorimetric sensor, being able to calculate parameters such as CCT, Ra or Rf with a very small margin of error.

3 Objectives

This thesis has been developed within the framework of an industrial PhD program, so we have tried to find a practical application to all the theoretical developments.

In this thesis, the main objective is to make progress in the state of the art regarding light emission and light sensing, so this manuscript has been divided into two parts. Each part, in turn, contains a theoretical development and an experimental implementation, where the theoretical results obtained are tested in a real environment.

Thus, at a schematic level, the specific objectives of this work are described below:

- Objective 1: Developing new algorithms that can be incorporated in multichannel lighting systems to reach new applications. These algorithms are designed to obtain optimized values of colorimetric, non-visual and energy efficiency parameters throughout the chromaticity diagram, mixing the light of the different LED channels of the luminaire. Specifically, the new algorithms must be able to return results separated by 0.01 units in the CIE 1976 chromaticity diagram with an $R_f > 80$, even outside the Planckian locus.

- Objective 2: Creating prototypes to be incorporated in a showroom that have the results of the developed algorithms in the microcontroller memory. Experimental

measurements of the created prototypes will be performed, and their quality will be checked through the ANSI C78.377-2015 standard. In addition, tests will be performed on a commercial device. It is expected that at least half of the measured points will pass the quality test, both in the prototypes and in the commercial device.

- Objective 3: Developing algorithms that allow a light sensor to provide CCT, Ra and Rf values in an accurate way. We have incorporated four different types of spectral reconstruction models to perform a calculation of colorimetric properties, making a comparison between the models through different statistical parameters related to the error and choose a candidate to be implemented to a prototype.

- Objective 4: Creating a prototype with the improved light sensor to validate the development. This prototype will have the chosen spectral reconstruction algorithm incorporated and measurements of commercial lighting systems will be performed. The relative error between the created prototype and a professional spectrometer will be calculated, expecting at least half of the measured points to be within the error margins (2% for the CCT and 1.5% for Ra and Rf).

4 Light emission

This section is divided into 2 parts, coinciding with the specific objectives of this work: algorithms for light emission and luminaires for experimental verification. Then, the results are presented.

The aim of this chapter focusses on explaining the spectral generation algorithms and the developed prototypes.

4.1 Algorithms for light emission

As previously explained, there are numerous algorithms that can be used in the emission of light by a multichannel luminaire. In this case, a brute force algorithm has been developed which, through spectral emission simulations, allows for the generation of a large number of results. Subsequently, these results are filtered to choose those combinations of channels that best suit the needs of the problem to be solved.

All the code of the simulations has been written using Python 3. Among all the libraries used for the matrix calculation of the simulations, Numpy, Scipy and Pandas stand out, libraries that are widely used to perform general mathematical calculations and implement algorithms of all kinds. In addition, Luxpy library [28] has been used to calculate some of the colorimetric parameters (such as CCT, Ra or Rf , among others).

For all this process described below, a patent application has been filed under the Patent Cooperation Treaty (PCT) and protection has been obtained at European and North American level. The patent also defines some areas of interest within the chromaticity diagram that are outside the interest of the spectral generation algorithm and a device that will be described at the section 4.2 [90].

A flow diagram of the developed algorithm is shown in Figure 4-1:

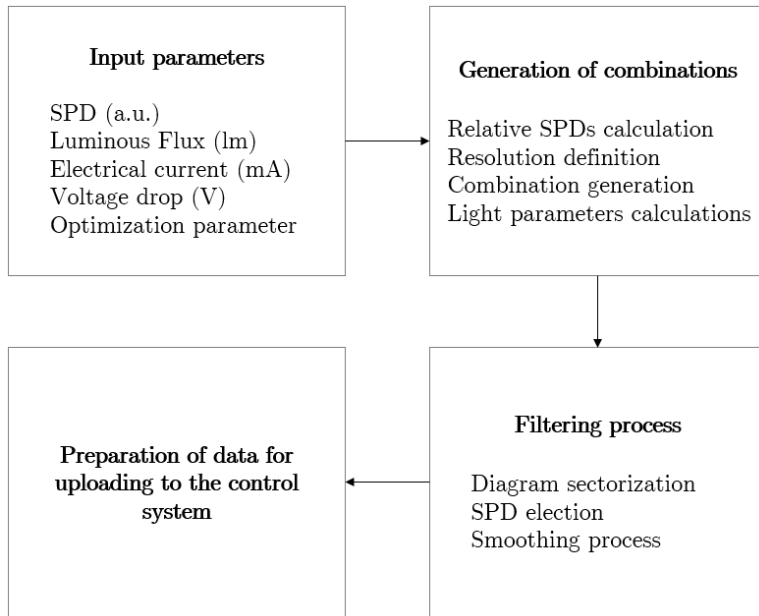


Figure 4-1. Flow diagram of the developed algorithm.

The starting point consists of a luminaire with n different channels and a control system that is capable of independently controlling each of the n channels. In addition, linear PWM dimming of the channels is assumed, with the possibility of adding specific profiles at the end of the process if necessary. Usually, there is a small difference between simulations and experimental measurements which, although they are usually imperceptible, must be considered when carrying out high precision studies.

The input data for the simulation algorithm for each of the n channels are described below:

- SPD within the visible range (from 380 to 780 nm) with arbitrary units
- Luminous flux in lumens
- Electrical intensity in milliamps
- Potential drop in volts

In addition, the optimization parameter is also required, specifying whether to maximize or minimize.

Once these values are entered, the algorithm starts calculating the relative SPDs between the n channels by making an adjustment between the input luminous flux and the SPDs in arbitrary units. A resolution r is defined, which corresponds to the number of accessible steps for each channel. The value of r must be lower than the resolution of the electrical current controller used by the light source.

Most electrical current controllers for LED light sources have a resolution ranging from 100 to 4096 steps, which means that it is possible to have either 100 to 4096 light intensities per each LED channel, depending on the current controller. Therefore, the total number of light combinations that can be emitted in a lamp depends on the resolution of the electrical current controller and the number of different LED channels. The number of possible combinations between LED channels follows the relationship of the Equation (25):

$$c = r^n \tag{25}$$

where c is the number of possible combinations, r is the resolution and n are the number of channels.

If, for example, we use a 5-channel light source with an electric current controller with a resolution of 4096 steps, this means that we can create $1.15 \cdot 10^{18}$ different SPDs, which is too large a number for a modern computer to handle. Since the number of channels is a fixed parameter of a given luminaire, this algorithm only allows us to change the resolution we work with.

Thus, to generate the c different combinations, the n SPDs of the channels are multiplied in an orderly sequence by a natural number between 0 and $r - 1$, both included. Subsequently, the n SPDs are added to obtain the SPD mix. This process is performed with all the different possibilities, generating the c possible combinations for a multichannel light source. In addition, all the colorimetric, non-visual or energy parameters derived from the set c of mixed SPDs to be considered are also calculated, generating a significant amount of data. Among these calculations are the colorimetric coordinates of the CIE 1931 and CIE 1976 chromaticity diagrams. Along with these data, the normalized combination is also stored. Below (Figure 4-2) is a comparative example of the obtained results of a simulation of a 5-channel light source (red, green, blue, warm white and cool white) at a resolution of 4 and 16 steps:

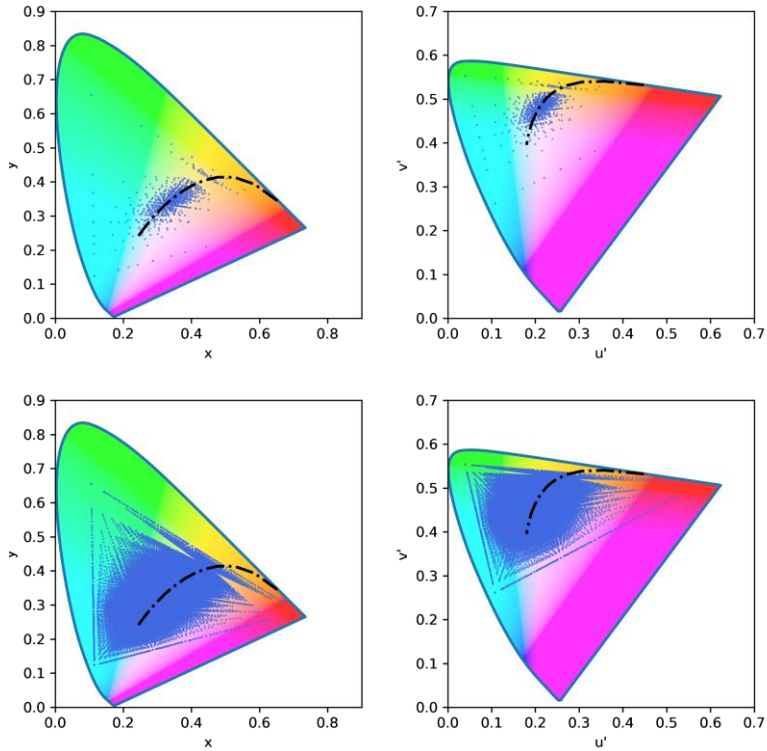


Figure 4-2. Results of a simulation of a 5-channel light source (red, green, blue, warm white and cool white LEDs) at a resolution of 4 (top) and 16 (bottom) steps for the CIE 1931 (left) and CIE 1976 (right) chromaticity diagrams. Each dot corresponds to the chromatic position of each SPD.

A particular combination is determined by the values of the channels of a multichannel source, so that it forms a vector with a components number equal to the number of channels. As an example, an LED-source with 5 different channels consisting of red (R), green (G), blue (B), warm white (WW) and cool white (CW), forms a vector which, normalized, can be displayed as follows:

[0, 0, 1, 0, 0]: all channels are off except B, which is at 100%.

[0, 1, 0, 0, 0]: all channels are off except G, which is at 100%.

[0.5, 0.5, 0, 0.5, 0]: channels B and CW are off, the rest at 50%.

Each combination of channels defines a possibility, a particular SPD of the LED-source. If, in addition, a resolution is defined, as it could be 11 steps, it means that each component of the vector can access 11 different values, defined by 0.10 value intervals, from 0 to 1, both included. Thus, for the proposed example (luminaire with 5 different channels with a resolution of 11 steps), $1.61 \cdot 10^5$ different possibilities are obtained.

The described way of operating, performing a systematic enumeration of all possible candidates to find an optimal solution (e.g., maximizing the colorimetric parameter Ra in a particular range of CCTs) and checking all candidates one by one, is called brute force search. This technique is widely used in solving many different problems, although most of the time it is not very computationally efficient.

Once the c possible combinations are obtained, a filtering process determined by the parameters to be optimized is performed.

The filtering process starts by sectorizing the CIE 1931 or the CIE 1976 chromaticity diagram, as appropriate. Using the CIE 1976 chromaticity diagram makes sense if you want to obtain points at the same distance in terms of color, but for the

visualization of results the CIE 1931 chromaticity diagram will be used, as it is much more widely used by the industry. As an example, a sectorization of the CIE 1976 chromaticity diagram is shown in Figure 4-3:

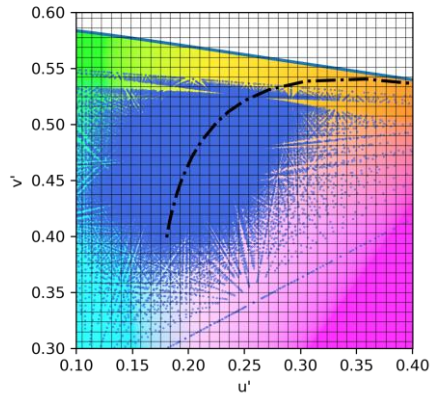


Figure 4-3. Detail of the sectorization of the CIE 1976 chromaticity diagram.

When the sectorization of the chromaticity diagram is obtained, if the sectorization is sufficiently small, we will find that the possibilities found within each sector have an extremely similar color, forming a subset of combinations c_i . It should be noted that, although the subset c_i emits a very similar color, the SPDs that form it do not have to resemble each other. Thus, we can consider the subset c_i as a set of metamers.

The concept of metamerism can be extended to all kinds of colorimetric parameters (such as CCT, Ra , $Rf...$), non-visual (M/P ratio, CS...) or even electrical (energy efficiency). On a practical level, for example, a specific yellowish illumination with fixed (x, y) coordinates can be obtained in many different ways:

using monochromatic amber LEDs, using RGB LEDs or using cool white and red LEDs. These three possibilities may be emitting exactly the same color with totally different SPDs. However, on a visual level, if an observer looks directly at the light source, it will appear that there are no differences between them.

In addition, it must be considered that the colorimetric and non-visual calculation parameters follow non-linear relations with the intensity of the different channels. To better understand this problem, let us take an example with two different white LEDs, one of warm hue with Ra 80 and the other of cool hue with Ra 90. Depending on the spectra of the two LEDs, when combining their light, it is possible that, during the transition from warm white to cool white, Ra reaches intermediate values between 80 or 90 or that at some points it is even higher than 90. Ra value during the transition cannot be known in advance nor can be interpolated, and it is necessary to perform precise spectral calculations to know exactly the Ra value at each point of the transition. If other different LED combination are also added and other colorimetric parameters such as Rf are calculated, the complexity of the problem increases enormously. If a classical optimization algorithm for Ra maximization is implemented, such as gradient descent, it is very easy to fall into a local minimum/maximum since the relationships between the simulated spectra and the calculation of these parameters do not follow linear relationships. Local maxima can be found continuously depending on the initial conditions.

Adding to this problem, it must be considered that the industry has the need to optimize more than one parameter at a time. For Human Centric Lighting (HCL) solutions, for example, it is necessary to consider the colorimetric affectation and the non-visual affectation. Thus, it can be necessary to optimize the parameters Ra and CS, with the possibility of modulating CCT and maximizing the energy efficiency. The lamp will include results with very different light characteristics (combinations with warm hues, cold hues, very high Ra , very high or very low M/P ratio, very high energy efficiency...), so we are interested in finding general values and then being able to filter the results according to the particular interests.

At this point, the input optimization parameter becomes relevant. For each sector, the chosen optimization parameter is filtered with the maximized or minimized value, as appropriate. In this way, a combination (with a given SPD) representing each sector is obtained, forming a set of vectors (with all the calculated information) distributed equispatially throughout the chromaticity diagram.

If, for example, the Ra parameter is chosen as the optimization parameter, it means that each sector is represented by the SPD whose color is within the sector and which maximizes Ra . Figure 4-4 is obtained by maximizing its value throughout the CIE 1931 chromaticity diagram.

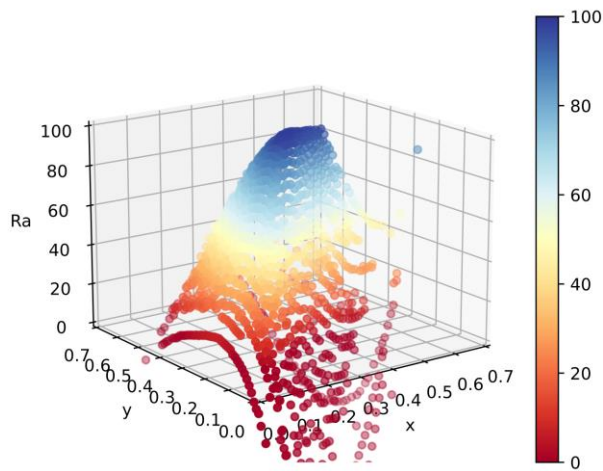


Figure 4-4. Ra values distributed according to the coordinates (x, y) of the CIE 1931 chromaticity diagram. The color scale cuts the negative Ra values to a minimum value of 0.

Another way to visualize the same information is to superimpose the different points on top of the chromaticity diagram in zenith view, as can be seen in Figure 4-5:

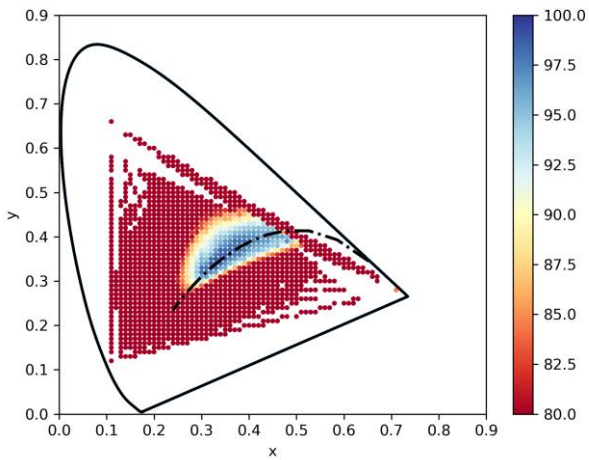
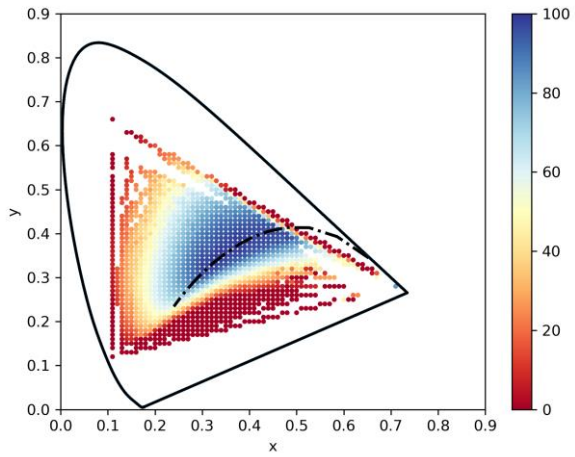


Figure 4-5. Ra values distributed according to the (x, y) coordinates of the CIE 1931 color diagram viewed from above. The color scale cuts the smallest Ra values from 0 (top) and 80 (bottom) to facilitate the visualization of highest values.

A common case is that a sector has a very different luminous flux from those around it, since the algorithm may have found very

different combinations of channels for neighboring regions. It should be noted that different light source channels can have different luminous fluxes, so these differences can be very large. This can be a problem if a transition of light between close sectors is chosen, as the user will perceive a sudden change in brightness of the light source. To solve this problem, smoothing is applied by implementing a low-pass filter. This type of filter is very common in signal processing and is often used to smooth data sets. In this way we ensure a smooth transition between sectors, so that the luminous flux varies in small increments in adjacent sectors. The optimized parameter suffers some small variation due to the smoothing of some of the sectors, although it is usually almost negligible if the resolution with which we have worked is sufficiently high. In addition, this process can also be used to fill in some sectors where there is no defined combination, creating more points in the entire color gamut of the light source. At the points where there is no defined combination, the control system can perform an interpolation of the closest points with negligible error.

The smoothing process can be repeated as many times as necessary, although it should be noted that, in every iteration, all combinations are modified.

Once the final results are available, they will be prepared to be compatible with the control system. Depending on the system, this may be limited by several factors, so it is necessary to consider the particular characteristics of each case. There are some systems that only support CCT control, while there are more advanced systems that can handle requests for colorimetric

coordinates. In this way, the luminaire will be able to provide the minimum or maximum value of the optimized parameter throughout its color gamut.

4.1.1 High resolution calculations

Using a supercomputer to run and test algorithms provides an important competitive advantage, since in many cases the algorithms have very intensive calculation needs considering the non-linearity of the results and the hard implementation of classic optimization algorithms.

The resolution and the number of channels are very important when calculating the computational resources needed to run the described algorithm. For each simulated light combination, the summed spectrum of the different LED channels and the parameters related to colorimetry, non-visual and energy properties are calculated. This process has a computational cost that is not depreciable, especially when there are a large number of light combinations generated.

In 2019 we received a request to enter a project related to lighting in a hospital environment. The different partners of the project were the scientific team in charge of the hospital itself, a manufacturer of light sources, a lamp control platform and us (*Kumux*). In this context, we were responsible for performing the high-resolution calculations of the LED system to be able to choose different light scenarios considering the visual, non-visual and power properties of light, such as luminous and radiant flux

or the energy efficiency of the particular light scenario. The main goal of the project was, once the results of the simulation had been processed and replicated to the lamps, to be able to quantitatively demonstrate the incidence of bio-adapted light in the recovery of patients, since there are preliminary studies that show very significant reductions in the hospitalization period of the patient. The study is still in process and there is a confidentiality agreement, so it is not yet possible to give preliminary information.

In this case, the luminaire manufacturer provided a luminaire with 6 different channels and the scientific team wanted results at the highest possible resolution. Since there is no clear boundary between low and high resolution, it was decided to do some initial calculations at 16 steps.

To try to provide more accuracy, an extra procedure was developed within the algorithm, complementary to the brute force method, which used gradient descent to find local minima and maxima at points of interest. These points of interest were defined together with the scientific team of the hospital and focused on finding maxima and minima of M/P ratio for certain given CCTs while preserving values close to the Planckian locus.

Following Equation (25), if we use a 16-step resolution with 6 different channels, $16 \cdot 10^6$ different combinations are generated. On an Intel Core i7-6700K processor (4 GHz, 4 cores), paralleling the calculations to take advantage of the computing power of all cores, 13.2 hours are needed to generate the table of results. Memory usage was also at its limit (32 GB), so the possibility of

using more powerful machines to increase resolution was considered.

At this point, it was decided to submit a SHAPE project to the Partnership for Advanced Computing in Europe (PRACE) in which we were able to access the MareNostrum supercomputer at Barcelona Supercomputing Center (BSC) and perform calculations at resolution 32. In this case, 200 nodes with 48 cores each were used, for a total of 9600 cores at 2.4 GHz.

In comparison, to perform the calculations at resolution 32, using the same Intel Core i7-6700K processor, we would have needed 35.2 days just to create the data file, without taking into account the memory limitation and other secondary processes. As explained below, using the MareNostrum it took about 2.3 hours to generate the file ready for processing and filtering.

Since the majority of LED electrical current controllers have a resolution ranging from 100 to 4096 steps, at the moment it is not possible to work with so much resolution using a 6 channel LED system, even for a supercomputer.

Working on the optimization of several parameters at the same time, for example, maximizing Ra and minimizing CS for a fixed CCT, evident differences can be observed between the spectra calculated in a resolution of 8 steps and 16 steps. In the 8-step resolution, the spectral solution found does not have some components that the 16-step solution has. For example, in a 128-step current controller we can work at a lower resolution to spend less time in the calculations of the simulation. We can

work at resolution 4, which implies 32-value steps in the current controller ($32 \times 4 = 128$). If we decide to work at 8-step resolution, the steps in the current controller will be of value 16, so working at resolution 8 implies that the values of resolution 4 are also being calculated. As expected, the 16-step resolution achieves better results since it contains the 8 resolution results.

For example, if we compare the results of the maximization of Rf in a 10,000 K CCT at different resolutions, we obtain the results shown in Figure 4-6.

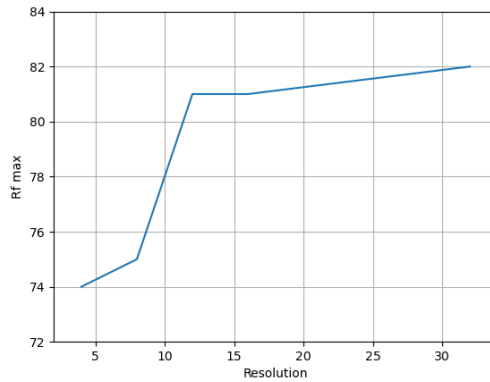


Figure 4-6. Results of the maximization of the IES TM-30-18 Rf for 10000 K CCTs at different resolutions.

Another interesting example is the comparison of the maximization of the M/P ratio parameter around a CCT of 3000 K white light ($-0.001 < Duv < 0.001$), as can be seen in Figure 4-7:

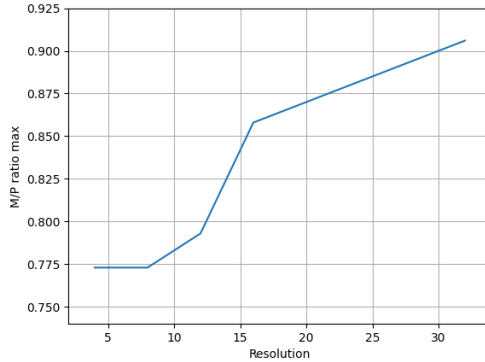


Figure 4-7. Results of the maximization of the M/P ratio for 3000 K CCTs white light ($-0.001 < \text{Duv} < 0.001$) at different resolutions.

In both examples it is possible to observe that, as the resolution increases, the value of the optimized parameters also increases. To know the LED system limits of the two optimized parameters (Rf and M/P ratio) it would be necessary to launch a simulation at the limit of the current controller resolution. However, as we have discussed previously, due to the high resolution at which they can work, it is not possible to simulate it with the current computational tools.

Initial version of the code for common computers

The first version of the code (version 1.0) used the *multiprocessing* module as parallelization strategy. The *multiprocessing* Python package supports spawning processes using an API similar to the threading module. Table 4-1 shows that the scalability of the version 1.0 of the code was poorly efficient.

Table 4-1. Performance of the version 1.0 of the code with resolution 6.

Cores	Time (s)	SpeedUp	Efficiency
1	2969.02	1	100.00%
2	1495.78	1.98	99.25%
4	846.23	3.51	87.71%
8	555.18	5.35	66.85%
16	371.64	7.99	49.93%
32	287.31	10.33	32.29%
48	259.22	11.45	23.86%

In this case, efficiency is the ratio of the ideal value of the code parallelization divided by the actual computation time. As an example, in Table 4-1, ideally the parallelized code with 48 cores should take 61.85 s, although in reality it takes 259.22 s. If the division is performed and multiplied by 100 to obtain the percentage, the value of 23.86% efficiency is obtained.

A first profiling study of the code showed that there were two main parts that consume most of the execution time. First of all, the simulation run a part of the code related to the gradient descent method, which was not parallelized initially, and it calculates results depending on a list of parameters (CCT, Rf , M/P ratio and Duv) given by the input. When this method ended, the simulation started the brute force part, which was parallelized using *multiprocessing* and was independent of the gradient descent part. Since the brute force part calculated all the possible combinations by brute force, these combinations

with a *mpi4py* parallelization to enable the code to run multi-node simulations. The *mpi4py* package provides Python bindings for the Message Passing Interface (MPI) standard. Additionally, in version 2.0 of the code, the gradient descent part is also parallelized using the *mpi4py* package improving the total execution time. The gradient descent is parallelized dividing each parameter of the input into the MPI processes available for this task. The brute force part is parallelized with *mpi4py*, distributing all the possible combinations over all the MPI processes dedicated to this part of the simulation. At the end of the parallel region of both parts of the code, all the results are gathered and processed to generate the results and the output. As both parts are independent, they can run simultaneously. To adjust the partitioning, a new parameter is included to decide how many MPI processes are involved in each part of the simulation.

Table 4-2. Performance of the versions 1.0 and 2.0 with resolution 6.

Cores	Version	Version	Version	Version	Version	Version
	1.0 Time	1.0 SpeedUp	1.0 Efficiency	2.0 Time	2.0 SpeedUp	2.0 Efficiency
1	2969.02	1	100.00 %	2745.34	1	100.00 %
8	555.18	5.35	66.85 %	345.51	7.95	99.32 %
48	259.22	11.45	23.86 %	82.78	33.16	69.09 %
192	-	-	-	21.89	125.42	65.32 %

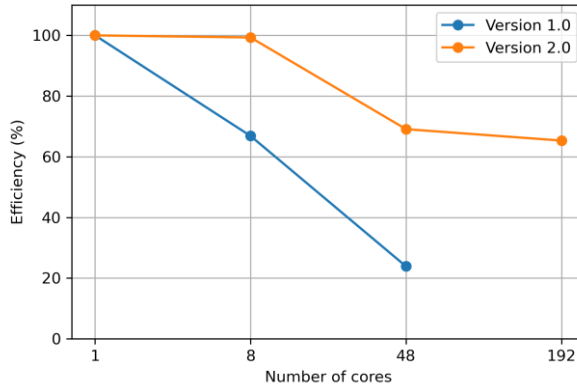


Figure 4-9. Performance comparison between code versions 1.0 and 2.0.

As observed in Table 4-2 and Figure 4-9, the performance of the version 2.0 had been improved parallelizing the gradient descent part and *mpi4py* enables the code to run on multiple nodes, for example with 192 cores, 4 nodes on MareNostrum. As version 1.0 cannot run on multiple nodes, the largest jobs with that version are up to 48 cores, the cores from one node of MareNostrum.

With version 2.0 we were able to run calculations with larger resolutions, but as the number of results depends on the resolution of the simulation, the generation of all the possible combinations and the output generations were a bottleneck. On version 2.0 (inherited from 1.0), the master process generated all the possible combinations for the brute force calculations, and it stored them on a text file. Then, each process reads from this file to get which subsection of the combinations is necessary to be calculated. Additionally, when each process ended its calculations, they sent their local results to the master process. And finally, the master MPI task processed these results and

generated an output file with them. In order to enable the code for larger resolutions, we developed a new version (version 3.0), where the generation of combinations was adapted to be done on each process involved on the brute force part. Therefore, each process computing the brute force calculations generates its own combinations. Additionally, on the version 3.0 of the code, when a process ends its calculations, it processes its own results and then it writes them in on a CSV file.

For example, as observed on Figure 4-10, using the version 2.0 with a simulation with resolution 16 using 4800 cores, the calculations take 460 seconds but the input and output generation on the master process takes more than 7000 seconds. Using the new implementation, the input and output generation is reduced to 120 seconds and 280 seconds for the calculations. The main performance improvement comes from the output generation, because as soon as a process finishes its calculations, it writes them on the output file. On previous versions, it is done sequentially by the master. In the case of a simulation with 9600 cores, with resolution 32 and with the new implementation, it takes 7200 seconds for the calculations and 1100 seconds for the input/output. It has been impossible to run a simulation with a resolution of 32 with the version 1.0 and 2.0 of the code due to a large number of combinations and results generated and gathered on the master node.

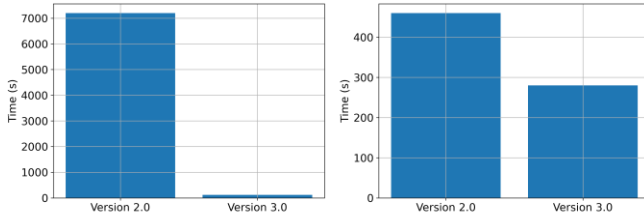


Figure 4-10. Time spent on input/output of versions 2.0 and 3.0 (left).
Time spent on calculations of versions 2.0 and 3.0 (right).

Also, as observed in Figure 4-11, the efficiency and scalability of the version 3.0 has been improved compared with the previous versions:

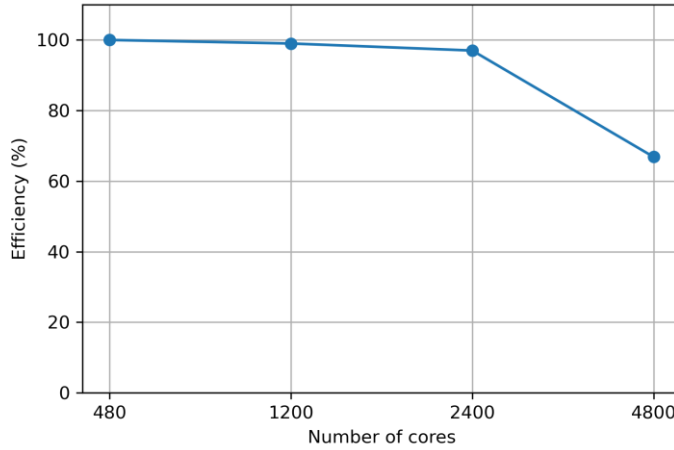


Figure 4-11. Efficiency of the version 3.0 with resolution 16.

As a conclusion for this section, the version developed during the SHAPE project enabled the code to run on multiple nodes and it was able to run simulations with higher resolutions, which were impossible to run on a reasonable time on the initial version of

the code. Also, due to the flexibility of the code to run with multiple nodes, the code is now capable of being used on a cloud infrastructure commonly used on a high-power computing project.

From a light point of view, it has been shown that higher results of Rf and M/P ratio can be obtained by increasing the resolution (Figure 4-6 and Figure 4-7). In some cases, improvements of about 6% can be achieved by going from a resolution of 16 steps to a resolution of 32 steps. However, as the resolution increases, the system is closer to reaching the absolute minimum or maximum, so the improvement tends to be smaller for higher resolutions. These improvements are not only important in hospital environments, where patients are exposed 24 hours a day to artificial lighting, but can also be important in other areas such as museum lighting, where the chromatic reproduction of works of art is essential to see the colors in an unaltered way.

A scientific article has been written about this section, published on the PRACE website, entitled “High resolution calculation for the optimization of commercial LED spectra in health applications” [99].

4.1.2 Colorimetric and non-visual parameters

Derived from the spectral calculation, a statistical study of hundreds of white LEDs on the market has also been carried out in order to find relationships between colorimetric and non-visual parameters.

In the industry, M/P ratio is often wrongly related to CCT and is often used indistinctly. To see if there is a relationship between the M/P ratio and CCT we will use a database of commercial LEDs where we have analyzed and filtered the white ones (723 different devices). In Figure 4-12 we can see the representation of these LEDs in the CIE 1931 chromaticity diagram and the position of every LED on the M/P ratio *versus* CCT chart. If there was a direct relationship between these two parameters, this point cloud would be a straight line.

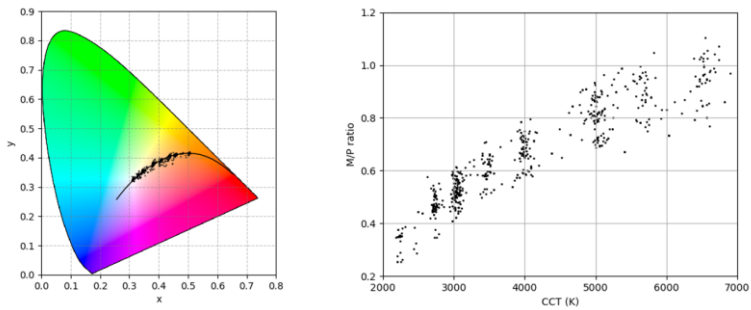
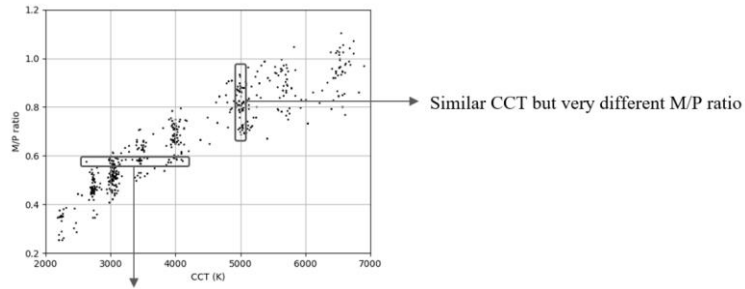


Figure 4-12. 723 white LEDs of the database represented on the CIE 1931 chromaticity diagram (left) and in the M/P ratio vs CCT chart (right).

It is very easy to find out that there are a lot of LEDs with similar M/P ratios but a very different CCT and vice versa, as shown in Figure 4-13:



Similar M/P ratio but very different CCT

Figure 4-13. M/P ratio vs CCT chart and comparison between white LEDs with similar M/P ratio but different CCT and vice versa.

For example, in Figure 4-14 we have two different commercial LEDs with a difference of 1500 K but with no M/P ratio variation. As the maximum of the circadian sensitivity function is situated around 490 nm, the amount of radiation around this value is crucial when calculating this parameter.

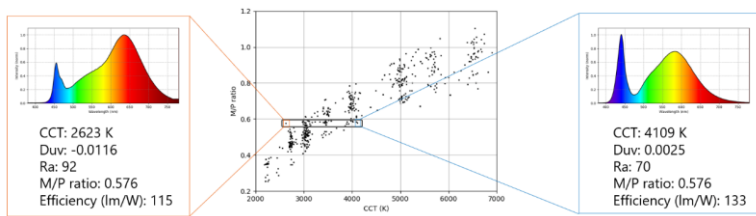


Figure 4-14. Comparison between two LEDs with the same M/P ratio but very different CCT.

Another interesting example can be shown in Figure 4-15: two LEDs with practically identical CCTs but with a huge variation of M/P ratio.

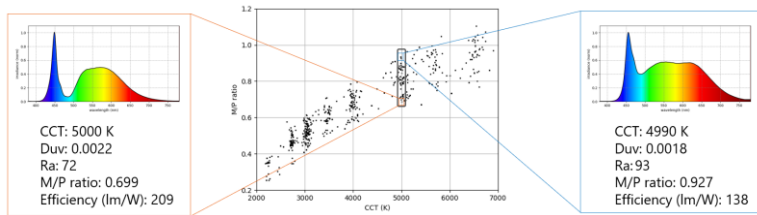


Figure 4-15. Comparison between two LEDs with very similar CCT but different M/P ratio.

What happens if we add Ra as a new variable in the same M/P ratio *versus* CCT chart? We can say that, when comparing phosphor-converted white LEDs and variations of this technology, the relationship between these three parameters seems more defined, as shown in the Figure 4-16. White LEDs have similar shapes: a blue/violet peak and then a spectral distribution of radiation along the visible range. LEDs with high Ra usually have more radiation around 490 nm, avoiding the cyan gap and affecting the M/P ratio value. However, as discussed later, the relationship between these three parameters is not generally applicable.

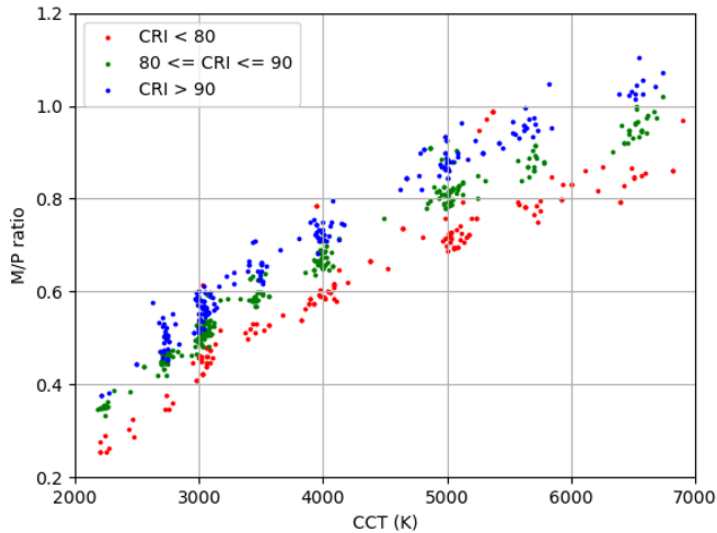


Figure 4-16. Relationship between M/P ratio, CCT and Ra applied to 723 commercial white LEDs.

If we take a look on the capabilities of a 5-channel system, composed by a red, green, blue, warm white and cool white LEDs, when comparing to the commercial white LEDs we can see that it is possible to achieve higher M/P ratio values for the same CCT, as shown in Figure 4-17. We can have Ra 80 combinations with a M/P ratio above 1 in CCTs greater than 4000 K. Moreover, if we focus on Ra values, we can see that it is possible to achieve Ra 95 values from 2400 K to beyond 7000 K. The white LEDs working alone have both an Ra of 84, so there is a substantial improvement resulting from a controlled mixing of the light.

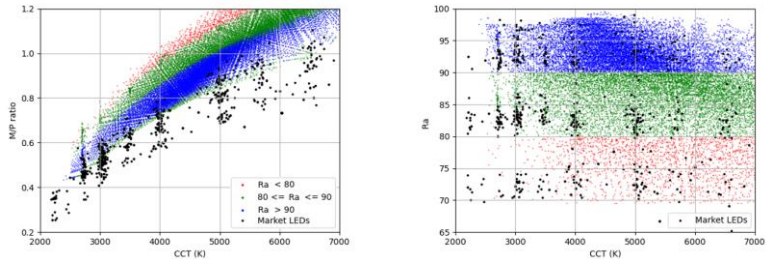


Figure 4-17. Achievable values of a multichannel luminaire for M/P ratio (left) and Ra (right) in function of CCT.

The results of a multichannel system are closely related to the global LEDs chosen. In this case, the choice is related to certain colorimetric parameters and the efficiency of the white LEDs.

If we select LEDs considering the M/P ratio, we can have a system that can achieve practically any M/P ratio available on the market. As shown in Figure 4-18, at 3000 K we can have Ra 80 combinations with an M/P ratio that can go from 0.4 to 0.8. If we look at Ra versus CCT chart, we can have values of Ra 95 from 2000 K to 7000 K and beyond. This means that we have the technology to achieve practically any value available on the market and this technology, on a multichannel system, depends more on the global selection of LEDs than the individual selection of white LEDs of the fixture we are creating.

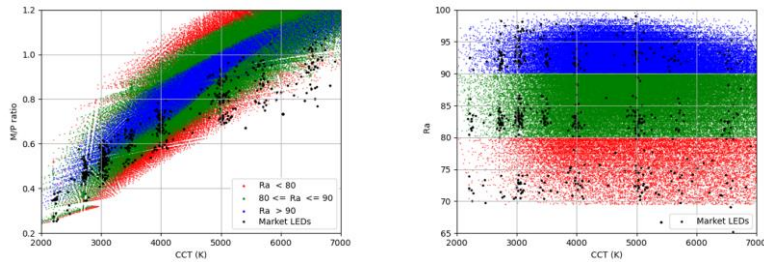


Figure 4-18. Achievable values of a multichannel LED system in order to get the maximum flexibility in M/P ratio.

Furthermore, the relationship between CCT, M/P ratio and Ra found for white LEDs is not applicable in multichannel systems. This is because these systems can deliver a lot of different spectral distributions as opposed to commercial white LEDs, that generally have similar SPDs. CCT can be modulated through several ways and the peaks of the monochromatic LEDs are crucial on the determination of the M/P ratio. A violet, blue, cyan, or green LED can increase CCT, but each one is going to have different impact on the M/P ratio.

Using a multichannel system enables us having full control over the light properties and going beyond the possibilities offered by the market. However, shaping the spectrum that matches our interests can be really challenging, because all the light parameters are interconnected. If we increase, for example, the intensity of the red channel, it will have consequences on the decreasing of CCT and M/P ratio but also varying Ra , energy efficiency, distance to the Planckian locus, etc.

This section is part of a paper presented at the LED Professional Symposium 2020 in the form of a digital conference [91] and to

the LED Professional Review magazine in the Sept/Oct issue of the same year [92]. The paper was awarded the Best Scientific Lecture/Paper – Technology Award 2020 for “systematically examine the effects of spectral distribution of LED and LED systems on various parameters for light quality and show that the quality parameters correlated weakly but it was necessary to optimize the spectral distribution in order to reach target values” [100].

4.2 Luminaires for experimental verification

This section describes the prototypes built that carry the results of the spectral generation algorithms developed in the previous sections, considering that the results described have been filtered, so they are ready to be incorporated into the microcontroller's memory.

4.2.1 Development of a control system

To have control over the prototypes, a software (Color Perception) was developed in Python 3 with a custom-made graphical user interface (GUI) that allows the adapted control of the luminaire both through the CCT and through the coordinates (u', v') of the CIE 1976 chromaticity diagram. In addition, the software is also able to communicate with an Ocean Optics USB2000+ spectrometer through the SeaBreeze library [101], so it is possible to measure the SPD of the prototype within an integrating sphere. In addition, Color Perception provides updated parameters of all colorimetric variables. The user can also control the device that is responsible for measuring the spectrum, changing its integration time or the number of scans. In the first version of the program, communication was via USB cable, while later versions use Wi-Fi control.

Below (Figure 4-19) there is a screenshot of the developed graphical interface:

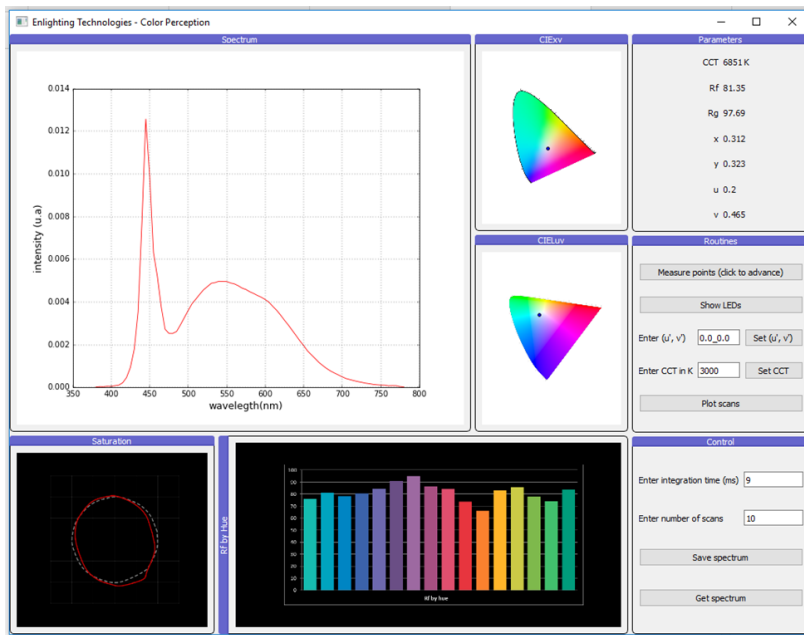


Figure 4-19. GUI of the program Color Perception.

4.2.2 First version of the prototypes

All the prototypes generated follow the same scheme, as shown in Figure 4-20:

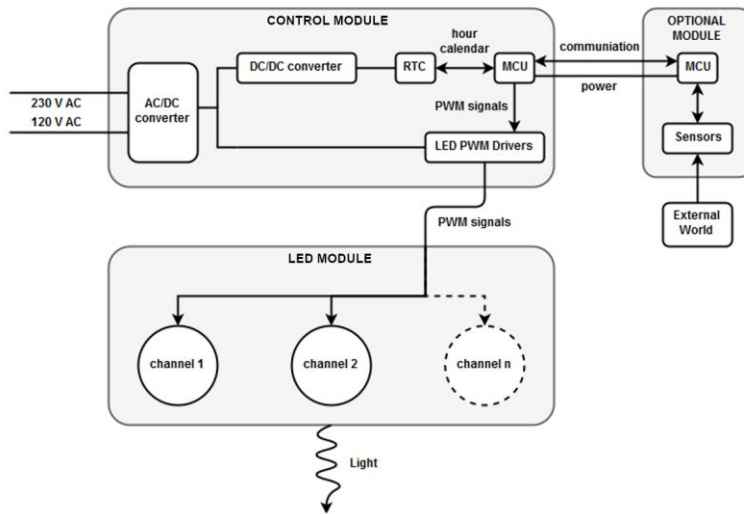


Figure 4-20. Schematic view of the prototypes created. It is possible to see the electrical connections and communication paths between the different elements, separated by modules.

Figure 4-20 shows the different modules of the prototypes:

- Control module. It consists of an AC/DC converter, a DC/DC converter, a real time clock (RTC), a microcontroller and electrical current drivers. The results of the algorithm are stored in this microcontroller, which, connected to the light sources through the current drivers, will provide the previously calculated light.
- LED module. It consists of a plurality of light sources mounted on a PCB. They receive the electrical signals necessary for their operation and emit the light simulated by the spectral generation algorithms. Each channel may

be composed of one or more LEDs with similar electro-optical characteristics.

- Optional module. It consists of a microcontroller that can be connected to one or more sensors. If connected, this microcontroller communicates with the microcontroller of the control module to exchange information (sensor data, specific information, time coordinates, etc.). The optional module can take control of the lighting system, so the microcontroller of the control module is in charge of managing the whole system, whether the optional module is attached or not. This microcontroller can also have the results of the algorithm loaded into it if necessary. The two microcontrollers communicate via standardized communication protocols such as digital interfaces, I²C interfaces or serial communication.

After evaluating different possibilities, it was decided to use a general-purpose microcontroller for the control module: the ATSAM21G18 from Microchip Technology Inc., which stands out for its low power consumption and is used for home automation, consumable products, measurement, or industrial applications. It is a 32-bit microcontroller and has an operating frequency of 48 MHz, 256 KB of flash memory and 32 KB of SRAM. In addition, it is connected to a variable voltage ranging from 1.62 V to 3.63 V, compatible with many sensors and components on the market [102]. To create the first version of the prototype, a breakout board was purchased from SparkFun Electronics, equipped with a USB interface (micro-B USB) and

compatible with the Arduino IDE, which allows fast prototyping. Figure 4-21 shows a picture of the breakout board used:

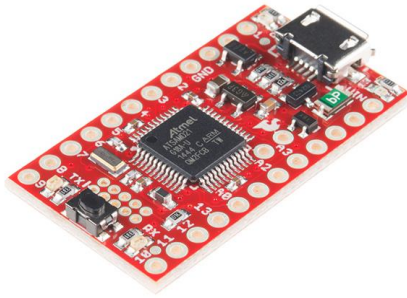


Figure 4-21. Picture of the breakout board used [103].

The algorithm can deliver the generated results in three different ways:

- Functions that run through the whole colorimetric diagram. Consists of a surface function within the available domain for each channel of LEDs, so they take up very little space in the memory of the microcontroller, but the time to obtain the electrical currents of the different channels is appreciable (a few tenths of a second for each channel).
- A single matrix that runs through the whole colorimetric diagram. The matrix has the colorimetric coordinates of the accessible area and the electric current values of each LED channel for each coordinate. This option has preference over the usage of functions, since the processing time of the microcontroller decreases a lot,

and the microcontroller has enough memory to store all the information of the matrix.

- Functions provided only by CCT. They are interesting since they allow obtaining the values of each channel of LEDs for a given CCT and deliver very smooth transitions. For the microcontroller, the speed of calculation is very high, and they take up very little space, but they only allow obtaining white light, without any color accent. This approach is useful if the control system supports CCT modulation.

A secondary objective of building these prototypes, besides experimentally validating the theoretical results achieved through the spectral mixing algorithm, is to be able to provide dynamic lighting that does not depend on an external control system (such as a smartphone). This means that the prototypes will be able to make variations of the emitted SPD throughout the day with an integrated control system inside the control module. This will require having an RTC connected to the prototype.

The first interaction of the prototype development consisted of building, on a solderless breadboard, a control module so that it could be connected to an LED module. To do this, breakout boards were used for the different basic elements: the microcontroller, an RTC and the drivers needed to power and control the LED module.

The RTC is a DS3231 device, which provides factory I²C communication compatible with the microcontroller. In this case,

the crystal needed to keep track of the time is inside the chip itself, which generates a great stability depending on the temperature. The power supply of these devices is external, since in case of switching off the luminaire, it will have to know the time at the moment of switching on in order to provide the appropriate SPD. In this first version, a breakout board from Adafruit Industries was used [104].

On the other hand, the current controllers used (using the AL8860 chip) provide a constant current intensity selectable at 330 mA or 660 mA with a potential drop that can reach up to 36 V. Dimming of each LED channel can be done via PWM. This type of dimming allows a linear control of the light intensity emitted by the LED [105], which is ideal for this type of applications. In this case, a breakout board from SparkFun Electronics has been used, which contains all the necessary elements for an easy and fast connection [106].

As can be seen in Figure 4-20, the designed electrical circuit is divided in two parts. There is an AC/DC converter that allows us to connect the prototype to the electrical network. Once a constant voltage is obtained, on one side the 24 V potential is reduced to a value of 3.3 V, compatible with the microcontroller and the RTC. On the other hand, the 24 V potential is used to power the LEDs, so the electrical current controllers are connected to this line. This allows working at two different voltages, having an adequate power supply in both parts.

The first version of the prototype mounted on a breadboard can be seen in Figure 4-22:

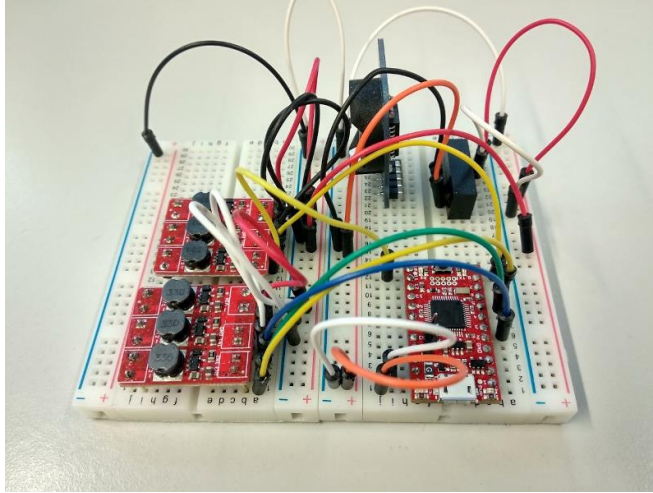


Figure 4-22. First version of the designed control system without the LED module.

On the other hand, an LED PCB was designed and manufactured to perform the first tests and the results of the algorithm were tested (Figure 4-23). This first PCB consisted of a matrix of 30 different LEDs with groups of 6 LEDs of 5 different types: red, green, blue, warm white and cool white. All LEDs were connected in series and the electrical current was limited to 120 mA to avoid excessive overheating, so an electrical resistor had to be added to the electrical current drivers.

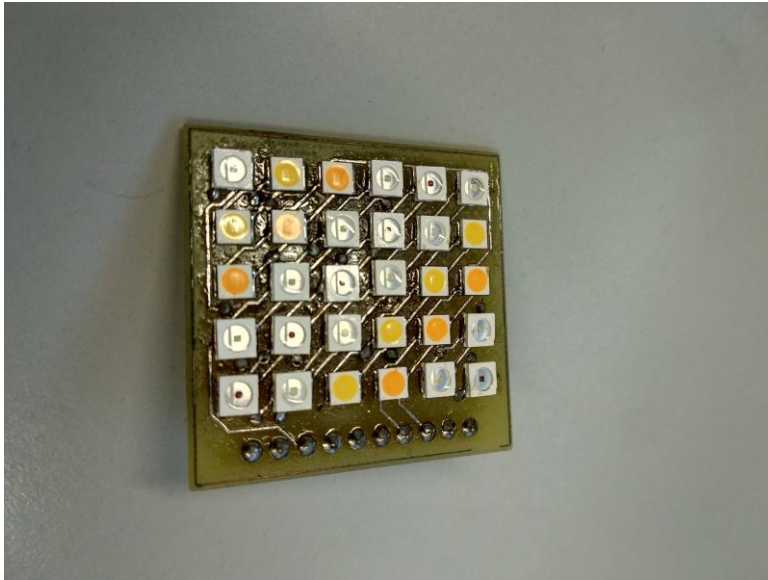


Figure 4-23. First version of the LEDs PCB.

4.2.3 Second version of the prototypes

The second version of the prototypes is conceptually the same as the first one. However, in this case a much more compact design has been made, avoiding the use of wires, creating a custom PCB both in the control system and in the LEDs. The components of the previous version have been maintained, since the objective was to see if it was possible to make a first encapsulation of all the components in a globe-type light bulb.

For this purpose, the Eagle PCB design software [107] was used, creating all the components and the connections between them. The design of the PCB for the control system can be seen in Figure 4-24:

In addition, for the study of the thermal behavior in operation, thermal pictures with a FLIR E5 thermal camera [108] have been taken to verify that the elements dissipate the heat correctly.

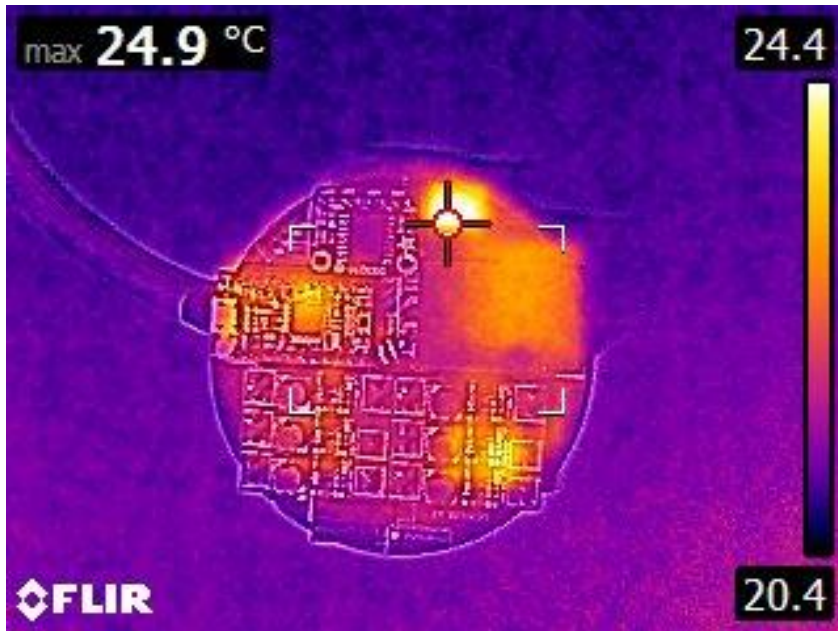


Figure 4-26. Thermal image of the driver PCB while working.

As can be seen in Figure 4-26, all components are close to room temperature while working.

In addition to the control module PCB, an LED module PCB was also developed to be able to take full advantage of the technology. The LEDs that were previously used were updated since they were discontinued, having to try numerous different models to find the best candidates.

For the evaluation of the different LEDs, 30 different models of various brands were purchased. The LEDs were soldered onto copper plates (Figure 4-27) discarded from other electronic designs and evaluated on the integrating sphere, obtaining the basic spectral properties of all of them. The main objective of this procedure was to find those LEDs that, among them, had a good match at the colorimetric level. To perform quick tests, a reduced version of the algorithm was developed, which allowed preliminary results to be obtained in a few minutes.

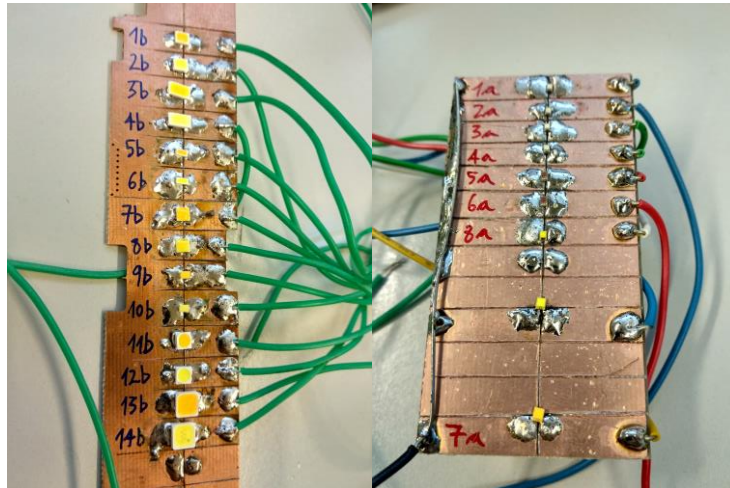


Figure 4-27. Some of the LEDs of the selection process.

After testing 30 different options, an optimal combination of warm white, cool white, red, green, and blue was found. It allowed obtaining excellent values for R_a and R_f (>95 in both cases) while conserving a very high energy efficiency (> 130 lm/W). Osram Duris S2 LEDs (2700 K, 6500 K) were used as white LEDs, while Lumileds LUXEON Z LEDs (660 nm, 500 nm and 470 nm) were used for the color LEDs.

The next step was to design the PCB for the LEDs. As, at this point, the idea was to validate the encapsulation of all the components inside a globe light bulb, the LED module PCB was made of standard material (FR4) that allows the use of different layers but does not dissipate the heat very well. The different LEDs were placed in such a way as to ensure a good color mixing and were connected according to their electrical characteristics.

The design of the LEDs PCB can be seen in Figure 4-28:

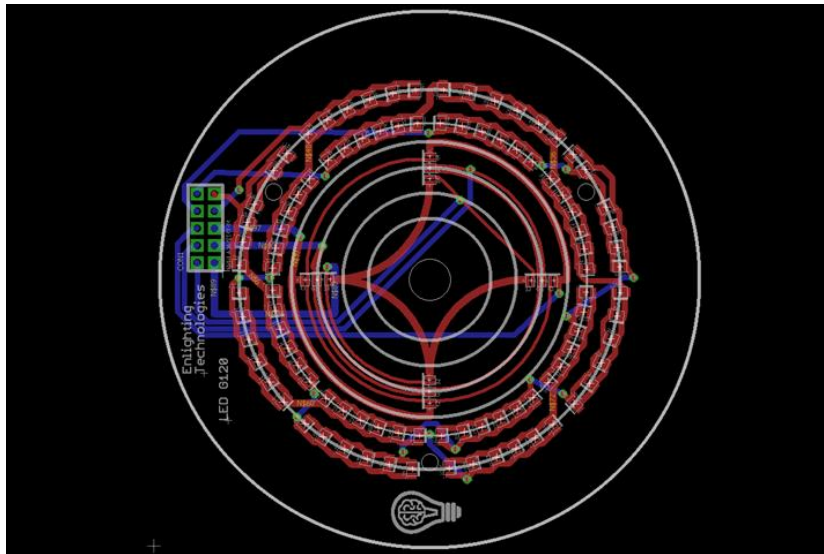


Figure 4-28. Design of the developed LEDs PCB.

The manufacture of the PCB and assembly of the LEDs were outsourced to a specialized company due to the enormous difficulty of welding small components. This PCB can provide about 1400 lm of luminous flux, although for thermal reasons a lower power was used to perform the tests.

Below (Figure 4-29) is a photograph of the LED PCB assembled and ready to be attached to the control module PCB:



Figure 4-29. Picture of the manufactured LEDs PCB.

Because of the material is not a good conductor, at thermal level the PCB heats up above the expected, although the values reached are perfectly acceptable for the LEDs (temperatures below 70 °C), as shown in Figure 4-30:

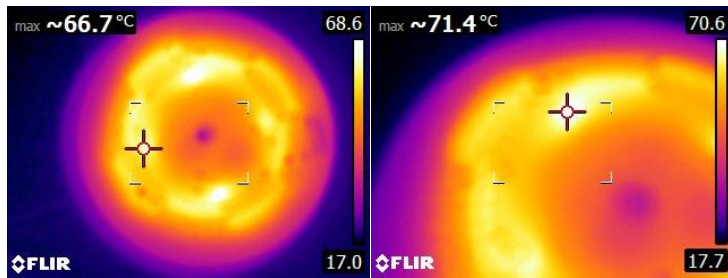


Figure 4-30. Thermal images of the PCB operating at 3000 K (20 minutes of operation) and maximum power. It is possible to see that the hottest spots are located above the LEDs R, G and B, where the highest electrical current circulates.

In Figure 4-31 it is possible to see the globe bulb, corresponding to the second prototype, working inside the integrating sphere:



Figure 4-31. Second version of the prototype working within the integrating sphere.

4.2.4 Third version of the prototypes

At this point, where the design had already been encapsulated in a globe bulb, the final version of the prototypes was created. In this case, breakout boards were removed. This point is very important, since it allows having total control over the design of

the PCBs, being able to miniaturize it. In addition, production costs are greatly reduced, because only the components strictly necessary for proper operation are used. In parallel, the LEDs were mounted on aluminum PCBs, which allow greater heat dissipation

The methodology, as a first step, consisted of making customized breakout boards to check the functionality of each of the elements separately. All the elements of the control system were combined and soldered into a single PCB. Several tests were performed, and some of them can be seen in the Figure 4-32.

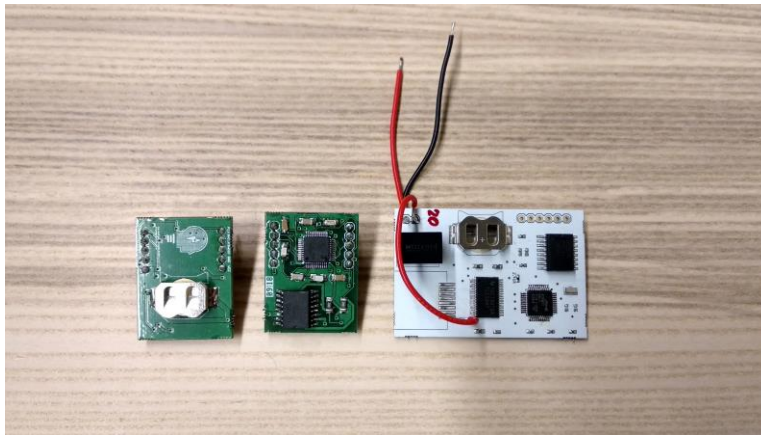


Figure 4-32. Various tests of the new control system designs.

In this case, it was decided to use a different current controller than the one used in the previous versions of the prototypes, as it presented several advantages. For the new version, a TLC5947 from Texas Instruments [109], was used, which allows electrical current control at 12-bit resolution (4096 steps) and, although it only provides 30 mA per channel, it has 24 channels that can be

combined among them, providing up to 720 mA of constant electrical current controllable by PWM. The switching frequency of the PWM is 4 MHz, avoiding any kind of flickering. Another advantage is that it uses Serial Peripheral Interface (SPI), a type of communication compatible with the microcontroller chosen for development. If more electrical power is required, several electrical current controllers can be daisy-chained together.

In total, three different models of prototype were developed. The control module PCBs were optimized to use the minimum number of components and the LED module PCBs were also designed to fit three selected commercial housings.

An aluminum substrate has been used in the fabrication of the LED PCBs. Unlike FR4, aluminum provides much higher thermal dissipation, although its electrical design is much more complex as only one layer can be used to avoid high cost.

This last family of prototypes was employed to validate the theoretical results through implementation on a real device. Two of the prototypes created, corresponding to the light bulb and the downlight, were integrated into a showroom created to have a space where the technology could be shown.

Light bulb

The housing is adaptable to a regular A-series E27 light bulb, corresponding to one of the standards. It has a luminous flux of 900 lm working along the Planckian locus.

The Figure 4-33 shows the schematics of the control module PCB and the LED module PCB designed for the light bulb prototype:

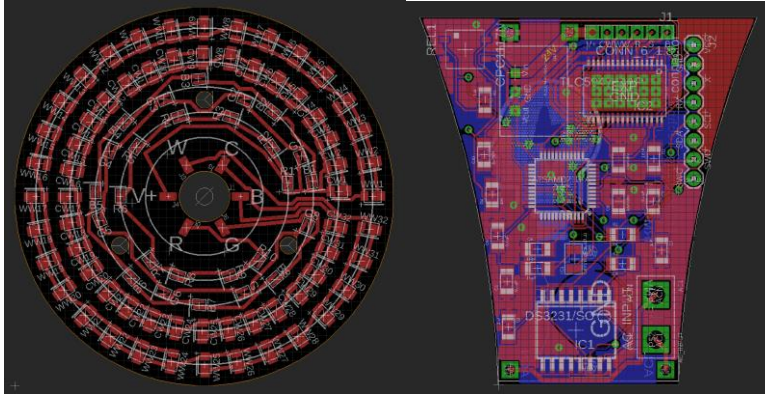


Figure 4-33. Schematics of the LED module PCB (left) and the control module PCB (right) of the light bulb prototype.

In addition to the PCB schematics, a picture of the light bulb prototype can be seen in Figure 4-34.

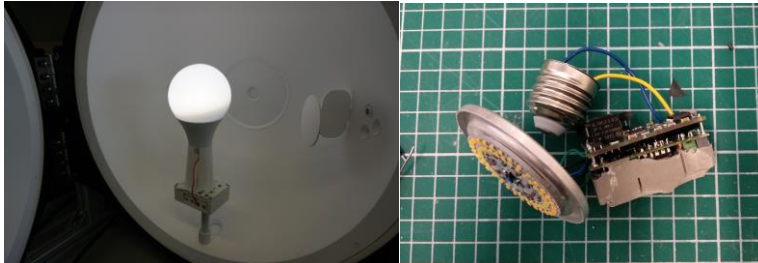


Figure 4-34. Picture of the light bulb prototype inside the integrating sphere (left) and the different disassembled modules (right).

From a thermal point of view, after 20 minutes of use, the temperature rises below 50 °C (Figure 4-35), about 20 °C lower than in the previous prototype (mainly due to the aluminum substrate of the LED PCB). This indicates that the temperature

of the LEDs is maintained in acceptable values when operating, delivering a good high luminous flux density (30 lm/cm² approximately).

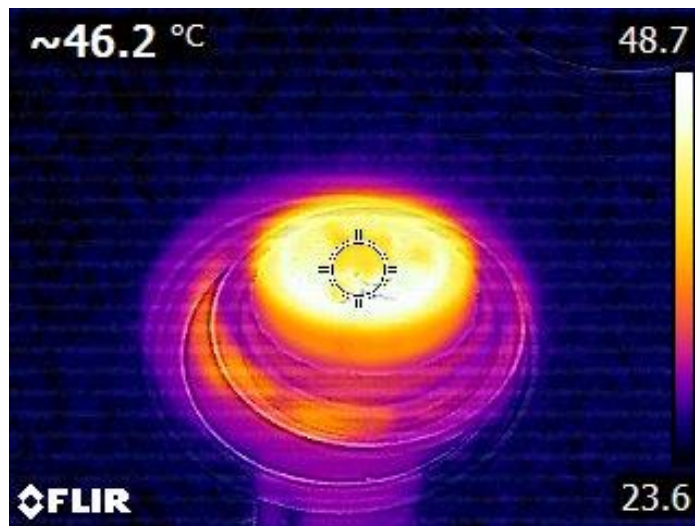


Figure 4-35. Thermal image of the light bulb prototype without the optical diffuser after 20 minutes of operation.

Downlight

Downlights are used as recessed lights in the ceilings. In this case, its technical characteristics are totally equivalent to floodlights since it uses the same components in the control module and the same number and type of LEDs.

Figure 4-36 shows the schematics of the control module PCB and the LED module PCB designed for the downlight prototype:

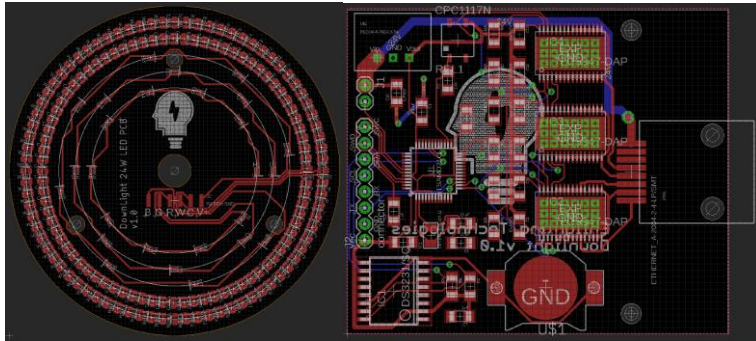


Figure 4-36. Schematics of the LED module PCB (left) and the control module PCB (right) of the downlight prototype.

In the case of the downlight, the control module is completely separated from the LED module. A Sigma R19 3D printer from BCN3D Technologies [110] was used to encapsulate the control module. A custom design was made using Tinkercad [111] and printed in order to protect the control module components. The downlight and control module are connected to each other via an Ethernet cable, which is responsible for power management to the LEDs.

Below (Figure 4-37) there is a picture of the downlight prototype without the optical diffuser and without the driver case cover:



Figure 4-37. Picture of the downlight prototype without the covers.

In this case, from a thermal point of view, the LED PCB is glued with thermal glue to the heat sink, which is made of aluminum. In the case of the control module PCB, the main heat focus is centered on the electrical current drivers. As was the case with the bulb prototype, after 20 minutes of operation, the temperature remains below 50 °C on both the LED PCB and the driver PCB. In Figure 4-38 it is possible to see the thermal behavior of both PCBs:

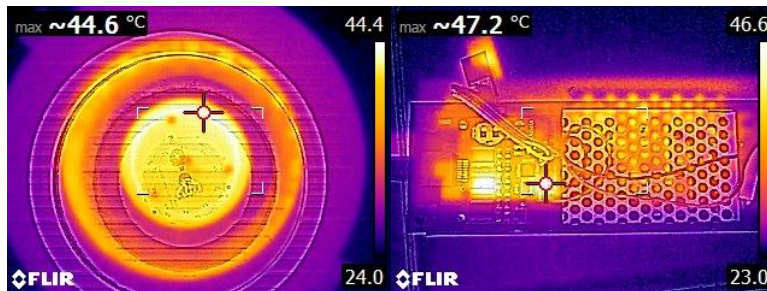


Figure 4-38. Thermal image of the LED module PCB (left) and the control module PCB (right) of the downlight prototype without the optical diffuser after 20 minutes of operation.

The downlights created have been installed in a showroom located in Parc Científic de Barcelona. The results of the installation can be seen in section 4.3.2.

Floodlight

Floodlights are used to project light onto surfaces in any position. They have a great versatility of use and usually have more power than a conventional bulb. In this case, the system is designed to

have about 2000 lm when the light emitted approaches the Planckian locus.

In the same way as in the previous case, Figure 4-39 shows the schematics of the control module PCB and the LED module PCB designed for the floodlight prototype:

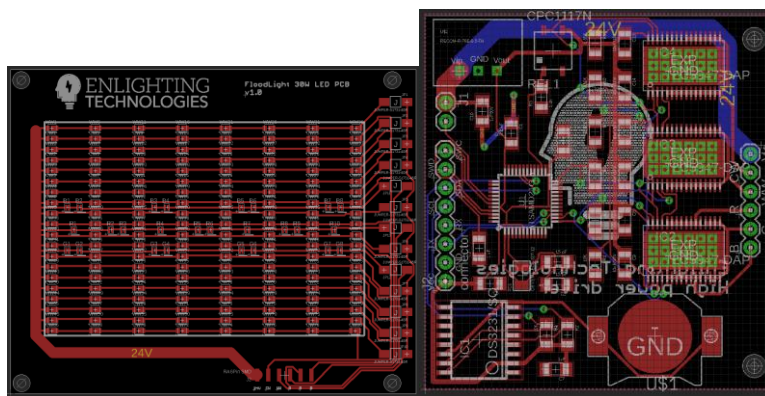


Figure 4-39. Schematics of the LED module PCB (left) and the control module PCB (right) of the floodlight prototype.

In addition to the PCB schematics, a picture of the floodlight prototype without the front cover can be seen in Figure 4-40:

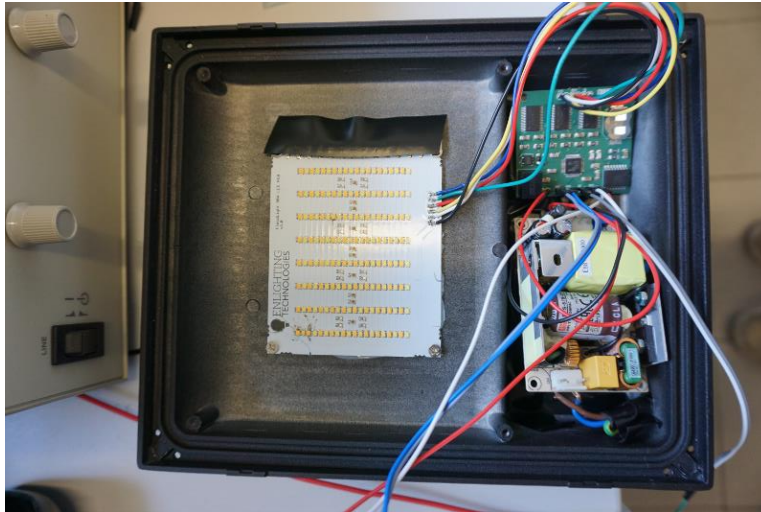


Figure 4-40. Picture of the floodlight prototype without the front cover

From a thermal point of view the situation is similar to that of the downlight: the LEDs PCB is glued to the thermal diffuser, which is also made of aluminum. In the case of the control PCB, it is totally separated and as in the previous case, the maximum heat source is in the electrical current drivers. Figure 4-41 shows the temperature distribution in the prototype after 20 minutes of use. In this case, the temperature is a little higher, around 60 °C. However, it is still within a totally acceptable range, since both the LEDs and the current drivers used are capable of withstanding temperatures above 80 °C:



Figure 4-41. Thermal image of the LED module PCB (left) and the control module PCB (right) of the floodlight prototype without the front cover after 20 minutes of operation.

4.3 Results

4.3.1 Measuring the light of the prototypes

Once the results for the light bulb and downlight prototypes have been obtained, the theoretical results are uploaded to the microcontroller and experimentally measured using an integrating sphere connected to a spectrometer. The prototypes and the spectrometer are controlled through Color Perception, the control software created for this purpose. Only the light bulb and downlight prototypes are evaluated because they are the ones that will be incorporated in a showroom located at Kumux offices, in Parc Científic de Barcelona. However, the floodlight results can be considered equivalent to those of the downlight, since the electronic and optical components are exactly the same.

In this case, the error associated with the coordinates (u', v') of the CIE 1976 chromaticity diagram will be measured. It has been decided to opt for the coordinates (u', v') because it corresponds to the most general output of the algorithm and also, the coordinates (u', v') are one of the parameters defined in the ANSI C78.377-2015 standard [39], which specifies the acceptable tolerance of the chromaticity of solid-state lighting products.

For this purpose, circles within the CIE 1976 chromaticity diagram are specified for the target coordinates so that if the SPD falls within the radius of the circle, it is considered to have a small chromatic variation. The circles are defined for different CCTs in the Planckian locus, but since there is no standard for cases far from the Planckian locus, the circles described in the

existing standard will be used. These circles have a radius of 0.0044 units in the CIE 1976 chromaticity diagram.

First, the different LED channels of the created prototypes are measured and loaded into the algorithm. The algorithm creates a table of results, and these are prepared for incorporation into the prototypes. In this way, the prototypes emit theoretical coordinates (u', v') separated by a distance of 0.01 units, with the condition of having an $Rf > 80$. Once the results are loaded into the prototype, they are measured.

Tables with the precise values of the measurements of the different prototypes can be found in section 7 (Table 7-1 and Table 7-2).

Light bulb

In the case of the light bulb, the following results (Figure 4 42) were obtained:

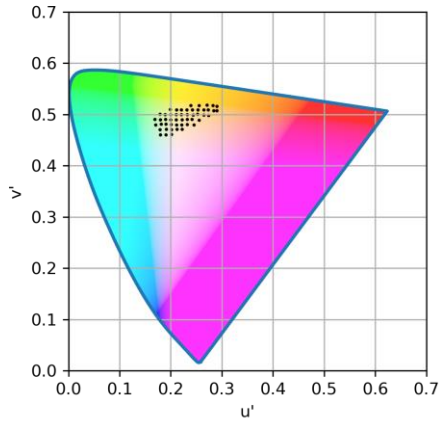


Figure 4-42. Area represented with points with $Rf > 80$ accessible for the light bulb prototype.

If we zoom into the area $Rf > 80$, we can see the chromatic deviation of the different points:

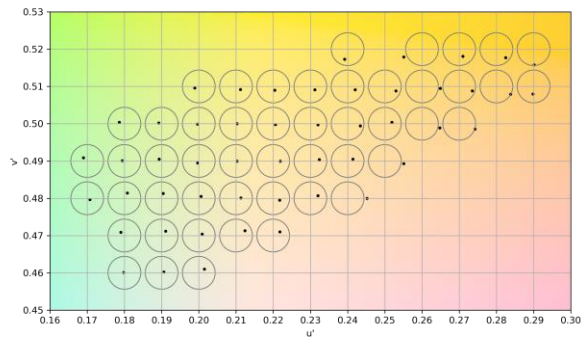


Figure 4-43. Chromatic deviations of the points with $Rf > 80$ for the prototype light bulb. Circles have a distance radius of 0.0044 units.

Figure 4-43 shows the circumferences defined in ANSI C78.377-2015 and the position of the experimental chromatic coordinates

for the bulb at the points where $Rf > 80$. In this case, 84% of the points fall within the error margins. At the remaining points, a recalibration of the system should be performed so that the remaining 16% also comply with a lower chromatic deviation.

The causes of the deviations can be diverse: from a deviation of the electric current emitted by the current controllers to an unforeseen increase in temperature. It must be considered that, in the case of the light bulb, the LEDs are very close together and, when a light configuration is emitted where several channels are involved, the temperature of one LED channel can affect the others. When measurements are made on each channel to enter the results into the spectral generation algorithm, however, there is not this associated problem. This means that the difference between the algorithm's input SPDs and the SPDs measured afterwards may be related thermal effects, indicating the importance of a good electronic design and a well-dimensioned heatsink.

On the other hand, the plot of maximum Rf as a function of CCT is shown below:

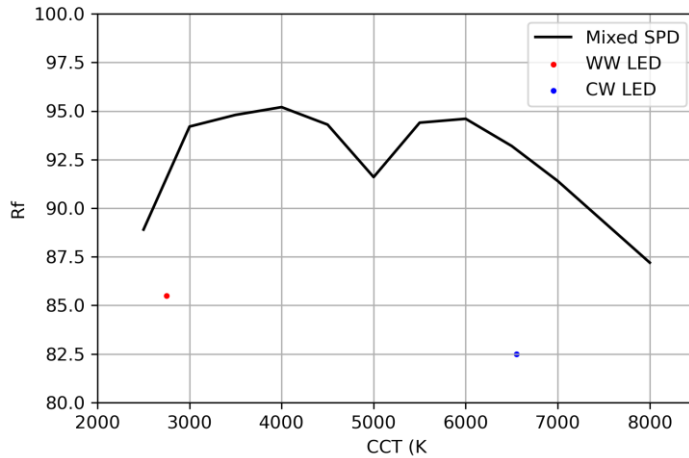


Figure 4-44. Rf values of the warm white LED, the cool white LED and the values achieved by the spectral mixing algorithm measured on the bulb prototype.

In this case, the imposed condition of $Rf > 80$ is more than met. On the other hand, Figure 4-44 shows the qualitative leap resulting from the application of the spectral mixing algorithm. The white LEDs used have an Rf of 85.5 in the case of warm white and 82.5 in the case of cool white. By mixing the different LED channels, these values are greatly exceeded. The maximum Rf point is achieved when the CCT is 4000 K, achieving a value above 95. From an efficiency point of view, with respect to white LEDs, the mixing of the different channels results in a loss of up to about 20%, depending on the spectral combination of each CCT. In absolute value, the energy efficiency moves in the range of 120-140 lm/W, higher than LEDs that are able to offer such high Rf values.

Downlight

In the case of the downlight, the procedure for the experimental measurement is exactly equivalent to the case of the light bulb, so that the results can be seen in the following Figures (Figure 4-45 and Figure 4-46):

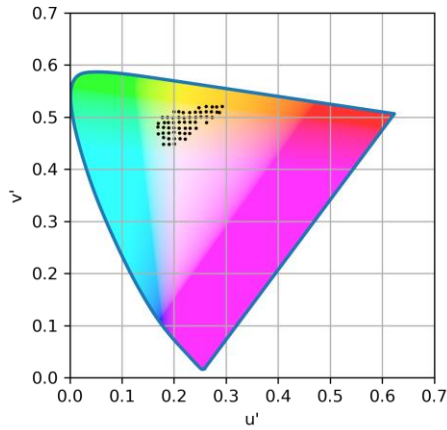


Figure 4-45. Area represented with points with $Rf > 80$ accessible for downlight prototypes.

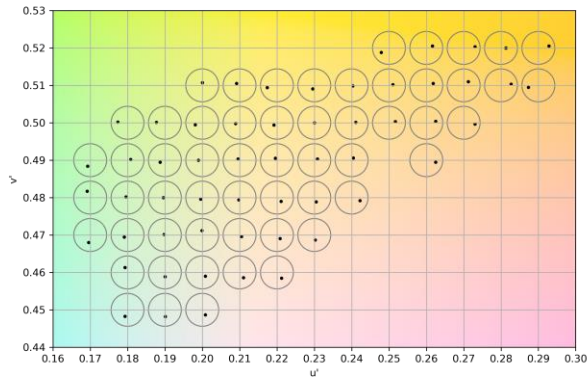


Figure 4-46. Chromatic deviations of the points with $Rf > 80$ for the downlight prototype. Circles have a distance radius of 0.0044 units.

Unlike in the case of the light bulb prototype, in this case 100% of the points fall within the error margins. Having the LEDs farther apart means that the thermal deviations between the different channels are lower, so the differences between the simulated and real spectra will also be lower.

The chart of maximum Rf as a function of CCT is shown in Figure 4-47:

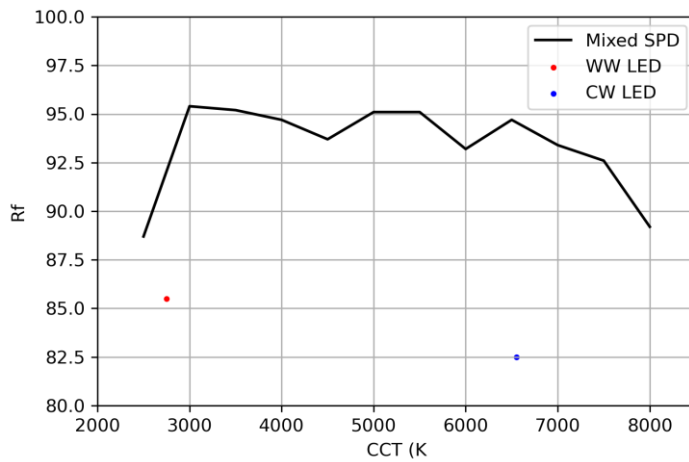


Figure 4-47. Rf values of the warm white LED, the cool white LED and the values achieved by the spectral mixing algorithm measured on the downlight prototype.

As in the previous case, the condition of $Rf > 80$ is more than fulfilled. In this case, Rf values > 95 are achieved around 3000 K and 5000 K. The energy efficiency is very similar to that of the light bulb.

4.3.2 Showroom installation

To demonstrate its potential, 8 downlights and 1 light bulb were installed in the Kumux showroom at Parc Científic de Barcelona.

The showroom is, at the same time, a working space for one person and has a main wooden table and several decorative elements, such as colorful chairs, flowers, books, shelves, among many others.

The control system is based on the use of the Wi-Fi network and the prototypes use an ESP8266 device connected to the optional control module. This allows a direct connection between the Color Perception software and the created prototypes via Wi-Fi. In addition, a series of predetermined scenes were designed to show some special functions, such as achieving a high $Rf (> 80)$ at a position far from the Planckian locus for different CCTs.

Some pictures of the installation are shown in Figure 4-48:



Figure 4-48. Different scenes in the showroom installed at Parc Científic de Barcelona.

The showroom was in operation from March 2019 until January 2022, at which time Kumux changed the location of its offices. During this period, numerous companies from the lighting industry as well as experts from the lighting field have passed through there. The showroom was also described in the award-winning article in LED Professional Review magazine.

4.3.3 Measuring the light of a commercial device

This section describes the results of the algorithm applied to a commercial device: a light bulb with a Tuya Smart control system [112] with tunable white balance control capability.

The bulb is composed of warm white LEDs at 2700 K and cool white LEDs at 6500 K. The control software used allows control of the CCT and separate control of the RGB LEDs. In this case, only the CCT control will be considered to evaluate the error of

the algorithm associated with this parameter in a low-cost commercial device.

In this case, the mixing algorithm uses an LED system composed of only two distinct channels: warm white and cool white. While this may seem like a simple case, the fact is that the variation of the CCT is not linear with respect to the electrical current values of the two channels, even if they are white, as is the case. This causes problems for control companies such as Tuya Smart, which can control bulbs of different brands in a single application. For the same value of electric current, two different bulbs can emit different CCTs, causing visible variations.

The warm white and cool white LEDs have been measured and the data have been incorporated as input parameters of the algorithm. The bulb is a 9W RGB+TW bulb marketed by Ampoule Smart brand [113]. As said before, only the use of whites will be considered. For controlling the light bulb, we will use the official app.

First the warm and cool white LEDs are measured, and the data is incorporated into the algorithm. Once the algorithm has produced the results, 10 different scenes (based on CCT) are selected and loaded into the Tuya Smart app using the calendar option.

The results obtained (theoretical and experimental) for CCT (K) and Ra can be seen in the Table 4-3:

Table 4-3. Experimental data containing expected and measured values of CCT and Ra .

#	c (%)	b (%)	Expected		Measured		CCT Error		Ra Error	
			CCT (K)	Ra	CCT (K)	Ra	Abs (K)	Rel (%)	Abs	Rel (%)
1	0	50	2766	82	2752	82	14	0.39	0	0
2	59	86	4909	86	4922	85	13	0.36	1	1
3	21	68	3541	85	3645	86	104	2.88	1	1
4	49	81	4548	86	4567	86	19	0.53	0	0
5	88	99	5939	85	5911	84	28	0.78	1	1
6	69	90	5269	85	5263	85	6	0.17	0	0
7	36	74	4052	86	4150	86	98	2.72	0	0
8	29	71	3806	86	3916	86	110	3.05	0	0
9	9	62	3094	84	3142	84	48	1.33	0	0
10	100	35	6378	84	6168	83	210	5.82	1	1

On the Table 4-3, the relative error of CCT has been calculated supposing that the maximum range is the interval the warmest and coolest possible CCTs. In the case of Ra , this range is fixed from 0 to 100.

In the case of the Tuya Smart app, the CCT value of a light bulb is controlled through the c parameter of Table 4-3. In the application there is a slider that allows controlling the CCT from a value 0 to a value 100, being 0 the warmest hue and 100 the coolest hue. Using this Table, it is possible to go from CCT values with arbitrary units ranging from 0 to 100 (c parameter) to CCT values in units of Kelvins.

To create the measurements, the 10 selected scenes have been programmed in the Tuya Smart app using the c parameter with random brightnesses (b parameter). Randomly varying the brightness allows us to obtain a more realistic scene, since it is a parameter that affects the CCT control in a secondary way but can be modified by the user.

To find out whether these results are acceptable or not, we turn again to the values recommended in ANSI C78.377-2015. According to this document, the CCT tolerance varies depending on the target CCT. The minimum acceptable variation is ± 102 K, corresponding to an extremely low CCT of 2200 K. In contrast, the highest acceptable variation is ± 510 K, corresponding to a CCT of 6500 K. The tolerable error increases proportionally as a function of the CCT, so that the intermediate values of CCT correspond to intermediate values of the errors considered. If all the values are reviewed, it can be observed that none of them exceeds the limits of ANSI C78.377-2015, being well below in all cases.

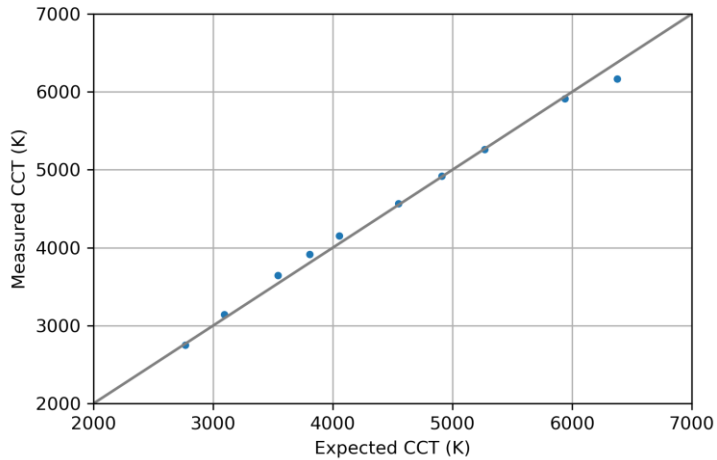


Figure 4-49. Display of the error between the expected CCT and the measured CCT. The gray diagonal line is for reference.

Generally, the experimental results of the measured CCT values are very good when compared to the expected values, as can be seen in Figure 4-49. In 50% of the cases, the error is less than 1%, while in 70%, the error is less than 3%. In all cases, the error is less than 6%.

The theoretical model developed, therefore, allows to apply improvements in different colorimetric parameters, such as Ra or Rf , with respect to the white LEDs used. These improvements have been applied in the prototypes created, although they are also applicable to commercial products that allow independent channel control.

5 Light sensing

The aim of this section is focused on the study of a multichannel color sensor to enhance its capabilities for improving its characteristics so that it can have functions similar to those of a spectrometer, albeit with limitations. Through the application of different models, ranging from interpolations to the use of NNs, it is intended to perform a spectral reconstruction and measure the following colorimetric parameters: CCT, Ra and Rf . A prototype to validate the theoretical development is presented afterwards.

In this case, as in section 4, Python 3 programming language has also been used. In addition to the libraries used in the previous section, we must add Tensorflow library [114], one of the references when applying ML algorithms.

In order to achieve this, the following hardware operation has been designed:

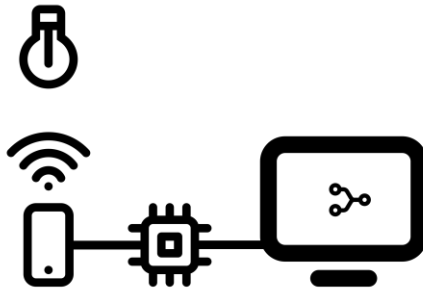


Figure 5-1. Schematic of the operation to improve the properties of a multichannel colorimetric sensor.

In Figure 5-1, the light emitted by an LED-source is collected by the multichannel color sensor which, through the connection with a microcontroller, sends the signal by cable to a computer. In the computer, the mathematical model is responsible for spectrally reconstructing the signal received by the colorimetric sensor and the colorimetric parameters are analyzed. The flow of information from the signal acquisition to the calculation of the colorimetric parameters is as follows (Figure 5-2):



Figure 5-2. Diagram of the information flow, from data acquisition to the calculation of colorimetric parameters.

This section, like the previous one, is also divided into 2 parts: algorithms for light sensing and color sensor for experimental verification.

5.1 Algorithms for light sensing

We proceed to create a virtual environment with a sensor and simulated SPDs to have a large amount of data to make interpolation adjustments and train the NNs involved, digitizing the whole process. These random SPDs are linked to a combination of LED light sources, so only spectra from LED technology can be faithfully reconstructed. The various reconstruction models that have been created are listed below:

- Linear interpolation. A linear interpolation is performed between the values of the different channels of the colorimetric sensor when measuring a light source. Subsequently, the colorimetric parameters are calculated.
- Cubic interpolation. Process analogous to linear interpolation, but using cubic interpolations between the values obtained by the colorimetric sensor.
- NN for spectral reconstruction. Same operation as in the previous cases, although this time a NN is used for spectral reconstruction.
- NNs for calculating CCT, Ra and Rf . In this case, no spectral reconstruction is performed and the values of CCT, Ra and Rf are calculated directly through 3 different NNs designed specifically for this purpose.

The errors committed in each model have been statistically analyzed to visualize the differences between them. Subsequently,

a database with SPDs of real LED-sources has been used to evaluate the error committed in commercial devices, being able to visualize the error committed in SPDs not created virtually.

The different components chosen to carry out the simulation, as well as the process of creating the virtual simulation environment, are described below, in the following subsections.

5.1.1 Sensor selection

There are a very large number of color sensors on the market, most of which are capable of providing red, green and blue values. However, there are other color sensors that can provide more information about the spectral composition of a light source, with more than 3 sensing bands. This is the case of the AS72651, AS72652 and AS72653 sensors from ams AG [115]. A schematic is shown in Figure 5-3.

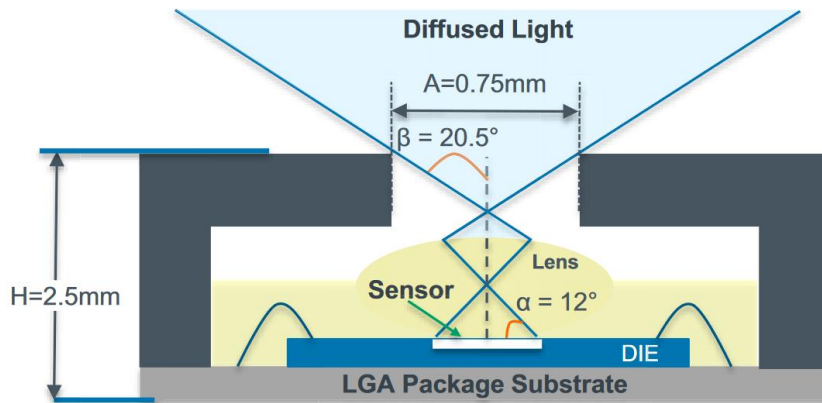


Figure 5-3. Schematic of AS72651, AS72652 and AS72653 devices.

Each of them has 6 independent optical filters with a total spectral range from 410 to 940 nm, with a FWHM of 20 nm. Putting the 3 sensors together (Figure 5-4) results in a module with 18 receiving channels, 14 of which are in the visible range, marketed under the name AS7265x.

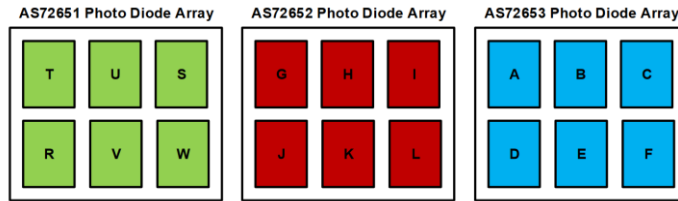


Figure 5-4. Photodiode arrays for the AS72651, AS72652 and AS72653 sensors.

The spectral response of the AS7265x module as a combination of the 3 sensors can be seen in Figure 5-5:

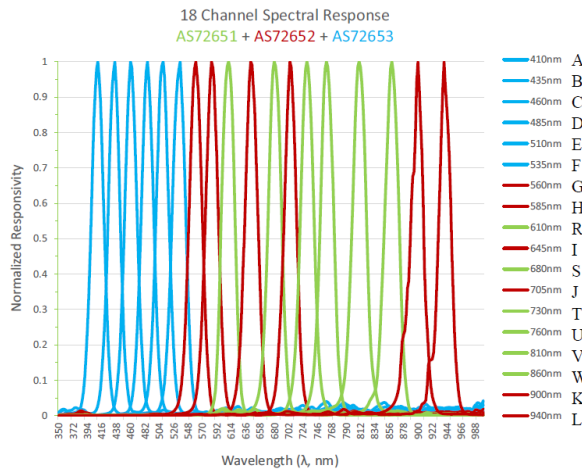


Figure 5-5. Normalized spectral response of the AS7265x module from ams AG. Each of the bands is labeled with a letter (A, B, C, D, E, F, G, H, R, I, S, J, T, U, V, W, K, L).

The module operates at a voltage of 3.3 V and has an I²C and serial interface that allows access to the sensor values. It has a 4 MB EEPROM memory with loaded firmware that controls the system. Each of the channels has an accuracy of 28.6 mW/cm² with an associated $\pm 12\%$ reading error. SparkFun Electronics has released a proprietary version of this module with a library developed for the Arduino platform (Figure 5-6). With it, it is possible to use I²C and access the sensor readings.

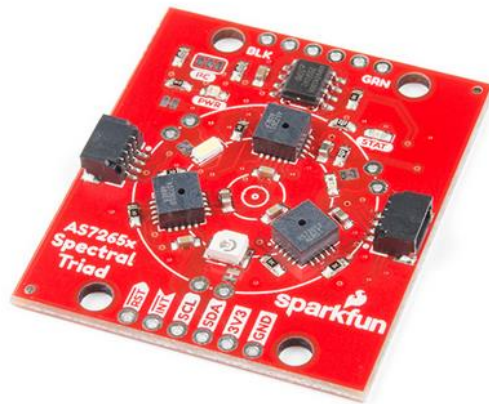


Figure 5-6. AS7265x module marketed by SparkFun Electronics [116].

5.1.2 Microcontroller selection

The microcontroller chosen is the same as the one used in the prototype construction (ATSAMD21G18A) since it is fully compatible with the potential drop of the chosen colorimetric sensor. In this case, unlike the previous one, only the Breakout Board version from SparkFun Electronics has been used, since there is no space limitation or thermal requirements.

5.1.3 Sensor module simulation

The spectral response of the AS7265x module has been simulated to make it easier to perform tests and, later, to program the different mathematical models for spectral reconstruction and calculation of colorimetric parameters. This allows a quick evaluation of the spectra, being able to generate a very large number of them, and to process the data easily. If the experimental device were used in the physical world, without using simulations, the number of data obtained would be much more restricted and it would not have been possible to perform the approximations in the following sections.

Since the objective is to calculate colorimetric parameters directly related to the visible range, only the sensor bands with the peak located between 380 nm and 780 nm have been simulated.

Each of the 14 sensor channels that fall within the visible range have been simulated, as shown in Figure 5-7:

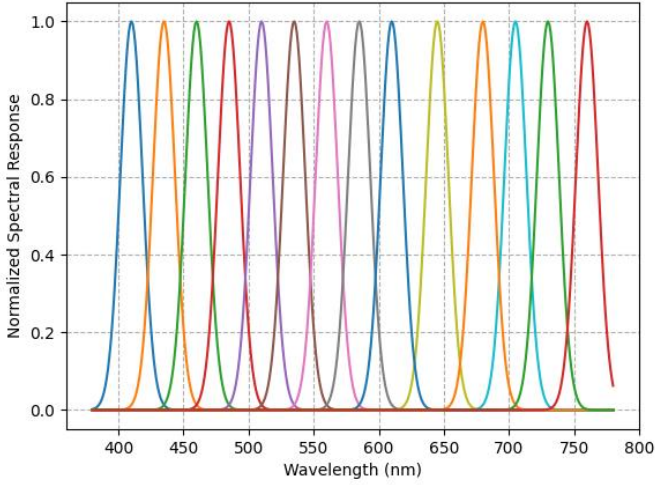


Figure 5-7. Simulation of the normalized spectral response of the different sensor channels within the visible range (380 - 780 nm).

The simulated measurement process performs a scalar product between the SPD of the light source and the spectral response of each of the sensor bands. Thus, the numerical value of the response of a band (S_b) is defined by the Equation (26):

$$S_b = \int_{380}^{780} I(\lambda) \cdot S(\lambda) \cdot d\lambda \quad (26)$$

where $I(\lambda)$ is the normalized LED irradiance, $S(\lambda)$ is the normalized spectral response of the band and λ is the wavelength in nanometers.

In this way, the responses of the different sensor bands can be obtained. Figure 5-8 shows an example of a set of randomly generated SPDs together with the simulated sensor response.

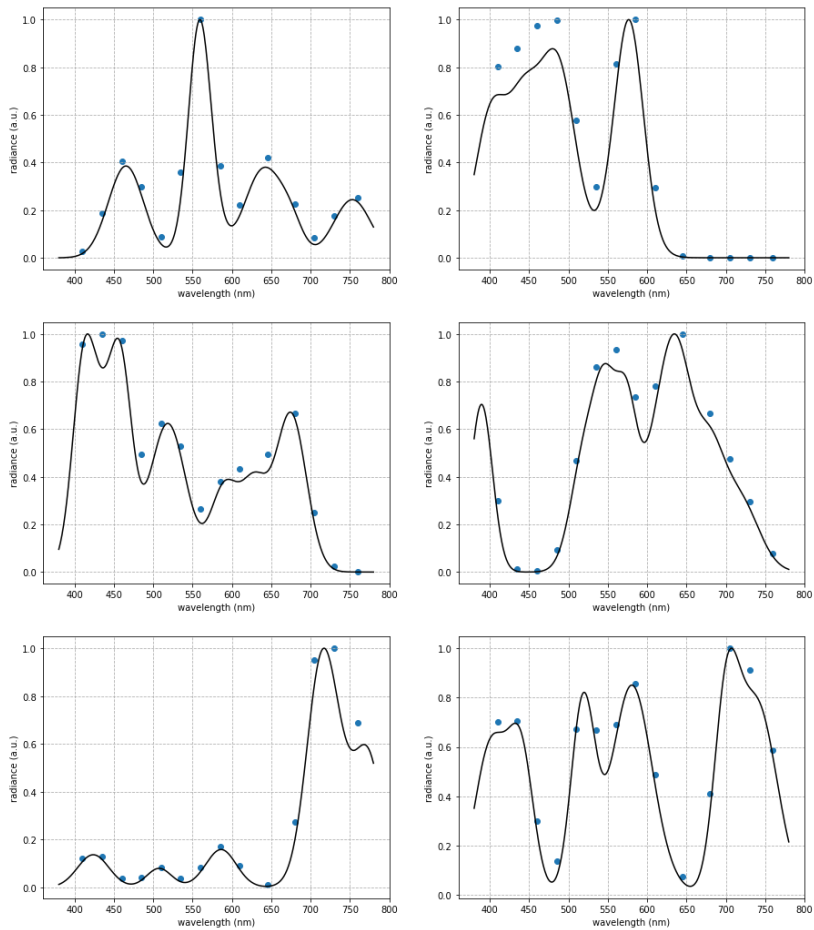


Figure 5-8. Simulation of the simulated sensor response (blue dots) compared to a randomly generated SPD (black solid line).

5.1.4 Creating random SPDs

To perform the simulations, a random SPD generation script has been developed. These SPDs are a composition of Gaussian functions with given values of peak wavelength, FWHM and radiance. This approach has been chosen because of its similarity

to a multichannel LED system in its most generic form, where all channels are composed of monochromatic channels. In addition, the spectra form of a white LED can also be considered as an array of monochromatic LEDs. The steps to create the set of random SPDs are described as follows:

- Definition of the number of individual Gaussian SPDs that will compose the random SPD set.
- Assignment of a random value for the peak wavelength between 380 nm and 780 nm for each Gaussian distribution.
- Assignment of a random value for the FWHM between 30 and 60 nm for each Gaussian distribution.
- Creation of the individual Gaussian SPD considering the peak position and the FWHM.
- Sum of the different individual Gaussian SPDs.
- Normalization of the sum SPD.

A graphical example of the generation of a random SPD is shown in Figure 5-9:

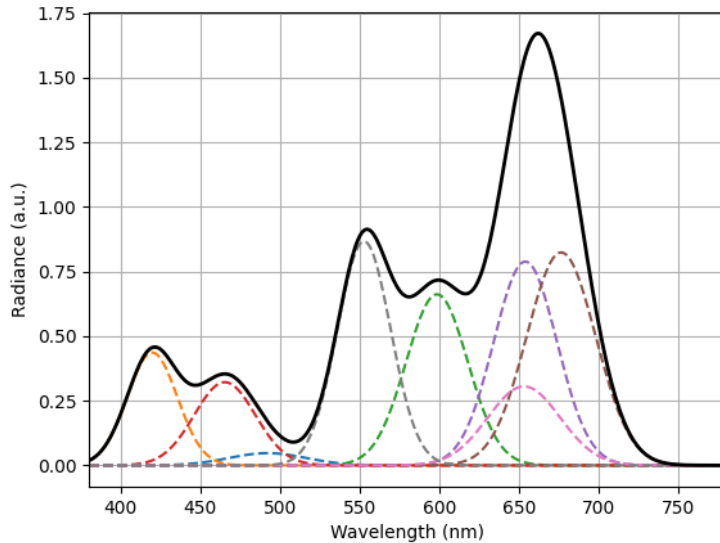


Figure 5-9. Example of the generation of a random SPD before normalization (black, bold). In this case, 8 individual Gaussian distributions (dotted lines) with the peak located between 380 and 780 nm and a variable FWHM from 30 to 60 nm have been used.

Although normally these generated random SPDs do not resemble the spectral shape of a white LED, this solution will allow solving more general cases, as shown at the end of this chapter.

5.1.5 Interpolated measurements

At this point, a comparison can be made between the simulated SPDs, and the data obtained by the simulated sensor, as well as CCT, Ra and Rf values. We will start with two different types of interpolation, linear and cubic, which will be in charge of generating the intermediate points given by the simulated sensor.

Cubic interpolation is interesting to consider as it can adapt well to the spectral nature of the LEDs, providing SPDs with smoothed peaks and valleys.

In this way, a large number of random SPDs are generated and the real calculated values of CCT, Ra and Rf of the SPDs are compared with the values obtained from the linear and cubic interpolations output from the simulated sensor values. The calculation of the colorimetric parameters is performed through the Luxpy library in both cases. In total, 10^5 random SPDs have been generated and 60% of them have been assigned to the training subset, 20% to the validation subset and the remaining 20% to the test subset. To see the error generated by the interpolations, only the test subset is used, which is the same that will be used later to see the reliability of the NNs developed.

The procedure to be followed to evaluate the errors made in the calculation of colorimetric parameters is shown schematically in Figure 5-10:

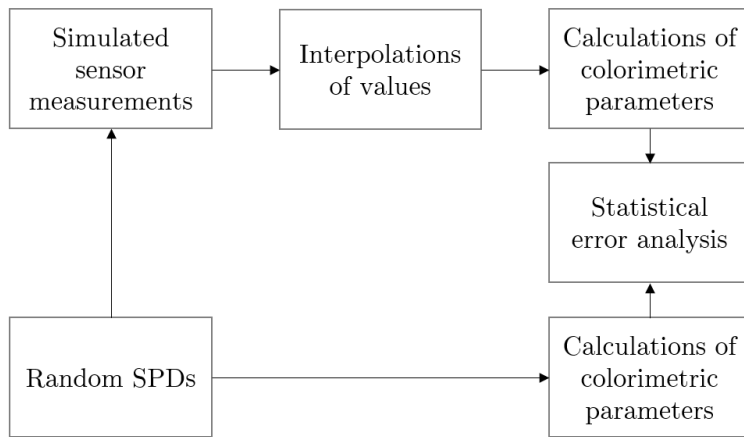


Figure 5-10. Schematic of the procedure to evaluate the error in the calculation of colorimetric parameters using the linear and cubic interpolations model.

Thus, if the sensor values are linearly interpolated, SPDs such as the following are obtained:

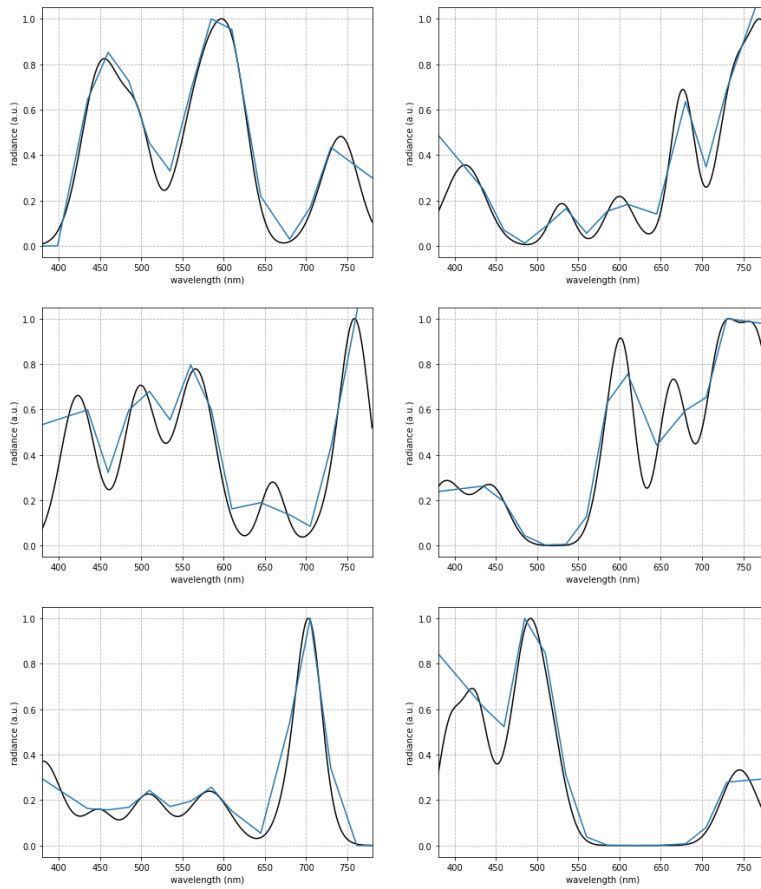


Figure 5-11. Example of linear interpolation of sensor measurements (blue) for randomly generated SPDs (black).

If a cubic interpolation of the same SPDs of Figure 5-11, is performed, the following results are obtained (Figure 5-12):

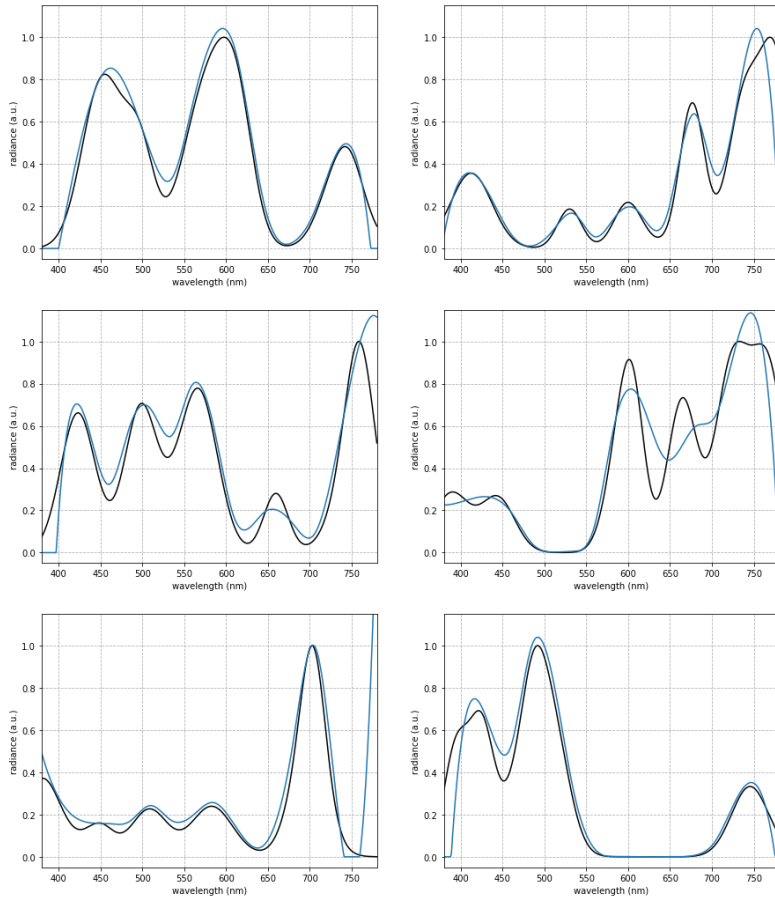


Figure 5-12. Example of cubic interpolation of sensor measurements (blue) for randomly generated SPDs (black).

If we calculate the CCT of the $2 \cdot 10^4$ randomly generated test subset SPDs (real CCT) and compare them with the CCT calculations derived from the linearly and cubically interpolated measurements, we obtain the results shown in Figure 5-13:

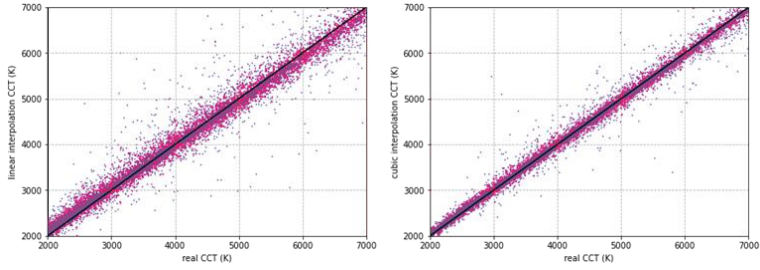


Figure 5-13. Comparison of the CCT calculation error for $2 \cdot 10^4$ random SPDs when the sensor measurements are linearly (left) and cubically (right) interpolated with respect to the real values. The black diagonal line serves as a reference to visualize the associated error in each case.

The distribution of the error in the CCT calculation between the real values and the linear and cubic interpolations is shown in Figure 5-14:

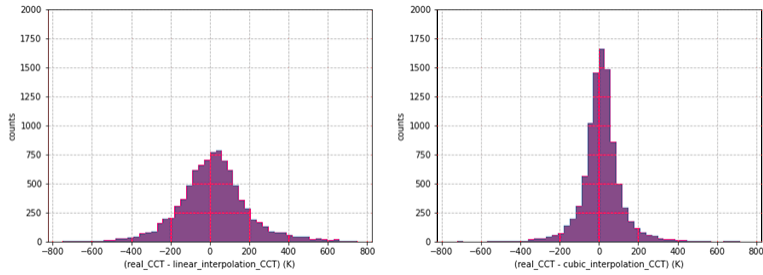


Figure 5-14. Distribution of the error committed in the calculation of the CCT for $2 \cdot 10^4$ random SPDs when the sensor measurements are linearly (left) and cubically (right) interpolated with respect to the real values.

Relevant statistical parameters are calculated, such as the arithmetic mean, the root mean square error (RMSE) and the standard deviation. The arithmetic mean measures the central value of a set of points in a distribution, while the RMSE is related with the precision, understood as the proximity of the

model to the real values. Finally, the standard deviation gives us information about the amount of variation or dispersion of a set of values.

Thus, we obtain the following statistical values for the calculation of the CCT (Table 5-1):

Table 5-1. Arithmetic mean, RMSE and standard deviation associated with the error of the CCT calculation for $2 \cdot 10^4$ random SPDs when sensor measurements are linearly and cubically interpolated.

CCT error (K)					
Arithmetic mean		RMSE		Standard deviation	
Linear	Cubic	Linear	Cubic	Linear	Cubic
21	13	241	131	240	130

For the calculation of the CCT, it can be observed that the statistical values obtained from the cubic interpolation are better than those from the linear interpolation. This fact can already be visualized in Figure 5-13 and Figure 5-14, where it is observed that the values obtained from cubic interpolation are more centered, more accurate and have less dispersion.

The same statistical analysis procedure is then performed for the *Ra* parameter, also obtaining better accuracy for cubic interpolation.

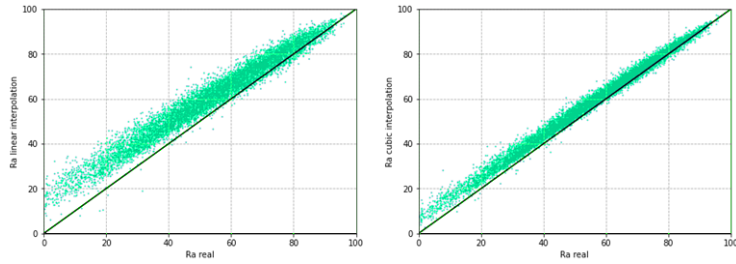


Figure 5-15. Comparison of the calculated Ra error for $2 \cdot 10^4$ random SPDs when the sensor measurements are linearly (left) and cubically (right) interpolated with the real values of the spectra. The black diagonal line serves as a reference to visualize the associated error in each case.

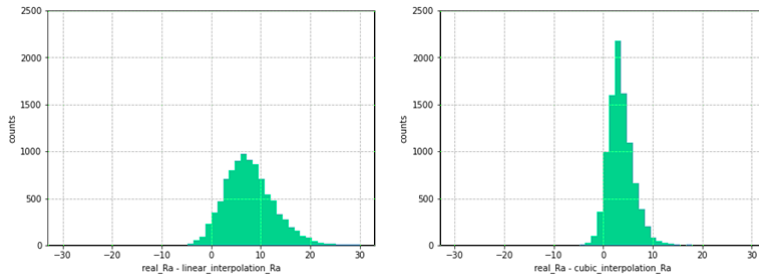


Figure 5-16. Distribution of the error committed in the calculation of Ra for $2 \cdot 10^4$ random SPDs when the sensor measurements are linearly (left) and cubically (right) interpolated with respect to the real values.

Table 5-2. Arithmetic mean, RMSE and standard deviation associated with the error of the Ra calculation for $2 \cdot 10^4$ random SPDs when sensor measurements are linearly and cubically interpolated.

CIE Ra error					
Arithmetic mean		RMSE		Standard deviation	
Linear	Cubic	Linear	Cubic	Linear	Cubic
7.8	3.5	9.3	4.4	5.2	2.6

In this case, a similar trend can be seen in the calculation of Ra , since the calculations made through cubic interpolation of the measurements are notably better than those made through linear interpolation. However, in this case it is also observed that the value of the arithmetic mean is much closer to the RMSE value compared to the previous case. This is because there is an overestimation of the value of Ra for both interpolations, providing higher values in general. As can be seen in Figure 5-15, Figure 5-16 and Table 5-2, this behavior is especially relevant at low Ra values.

Finally, the same statistical treatment is applied for the Rf parameter (Figure 5-17, Figure 5-18 and Table 5-3).

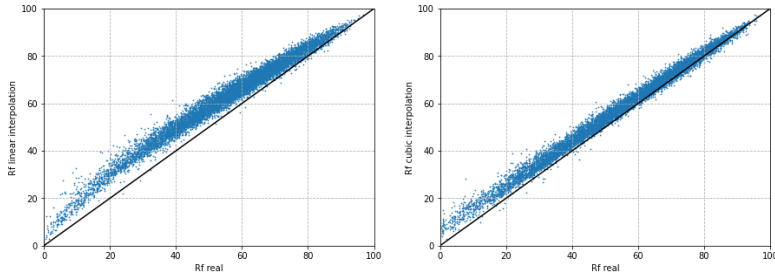


Figure 5-17. Comparison of the error of the Rf calculation for $2 \cdot 10^4$ random SPDs when the sensor measurements are linearly (left) and cubically (right) interpolated with the actual values of the spectra. The black diagonal line serves as a reference to visualize the associated error in each case.

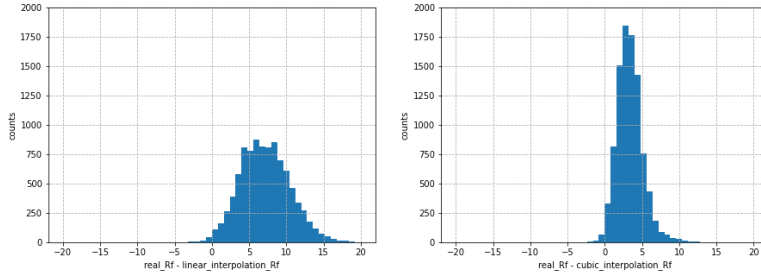


Figure 5-18. Distribution of the error committed in the calculation of Rf for $2 \cdot 10^4$ random SPDs when the sensor measurements are linearly (left) and cubically (right) interpolated with respect to the real values.

Table 5-3. Arithmetic mean, RMSE and standard deviation associated with the error of the Rf calculation for $2 \cdot 10^4$ random SPDs when sensor measurements are linearly and cubically interpolated.

IES TM-30-18 Rf error					
Arithmetic mean		RMSE		Standard deviation	
Linear	Cubic	Linear	Cubic	Linear	Cubic
7.2	3.4	7.9	3.8	3.3	1.7

In the case of Rf , the behavior is very similar to that of Ra . The values of the arithmetic mean, RMSE and standard deviation remain in the same order of magnitude as in the previous case. Again, cubic interpolation provides better values. The parameters Ra and Rf have a shared theoretical basis, so this behavior makes sense.

As a summary, in all cases, cubic interpolation provides a smaller error in the calculation of the CCT, Ra and Rf parameters than linear interpolation.

5.1.6 Spectral reconstruction neural network

In this section we are going to perform another type of approach: the creation of NNs for spectral reconstruction for the subsequent calculation of colorimetric parameters (CCT, Ra and Rf). NNs help to solve problems where there is a large amount of data, complex, with non-linear input and output values and sharing patterns [117], so they are a good tool for the problem we are trying to solve.

First, the SPD will be reconstructed through the application of a dedicated NN. Through this reconstruction, CCT, Ra and Rf calculations will be performed. In this case, a regressive NN is used since the repetition of certain patterns has been observed, such as smoothed ups and downs, which makes the spectral reconstruction follow a certain pattern with the potential to be trained. A schematic of the procedure to evaluate the error in the calculation of colorimetric parameters can be seen in Figure 5-19.

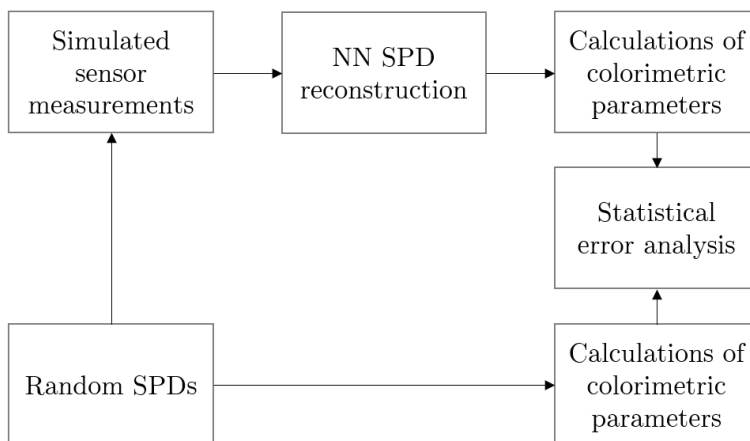


Figure 5-19. Schematic of the procedure to evaluate the error in the calculation of colorimetric parameters using the spectral reconstruction NN model.

The input parameters of the NN are the set of randomly created SPDs (forming a vector of 401 points) and the values of the simulated sensor channel measurements (forming a vector of 14 points). In this way, the NN is trained to convert the sensor values to the SPD values, undoing the integral of Equation (26). Figure 5-20 shows a diagram of the operation of the spectral reconstruction NN.

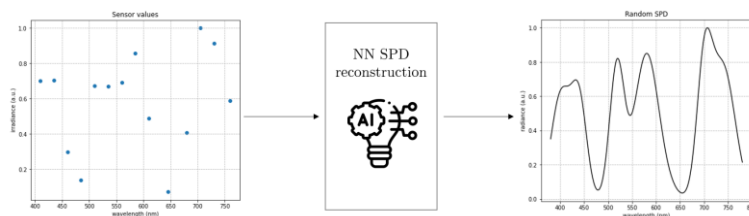


Figure 5-20. Diagram of the operation of the spectral reconstruction NN.

When performing the comparison between the different models (interpolations and NNs), the same test subset is always used in all cases.

At the NN architecture level, it must be considered that the input layer must have 14 neurons that match the 14 simulated sensor values, while the output layer has 401 neurons, corresponding to the 1 nm resolution of the randomly generated SPDs inside the visible range (401 points between 380 and 780 nm, both included). Thus, we start with a simple case, with a single hidden layer consisting of 128 neurons, an intermediate value between 14 and 401. The graphical results of the first approximation of 128 neurons, as an example, can be seen in the Figure 5-21:

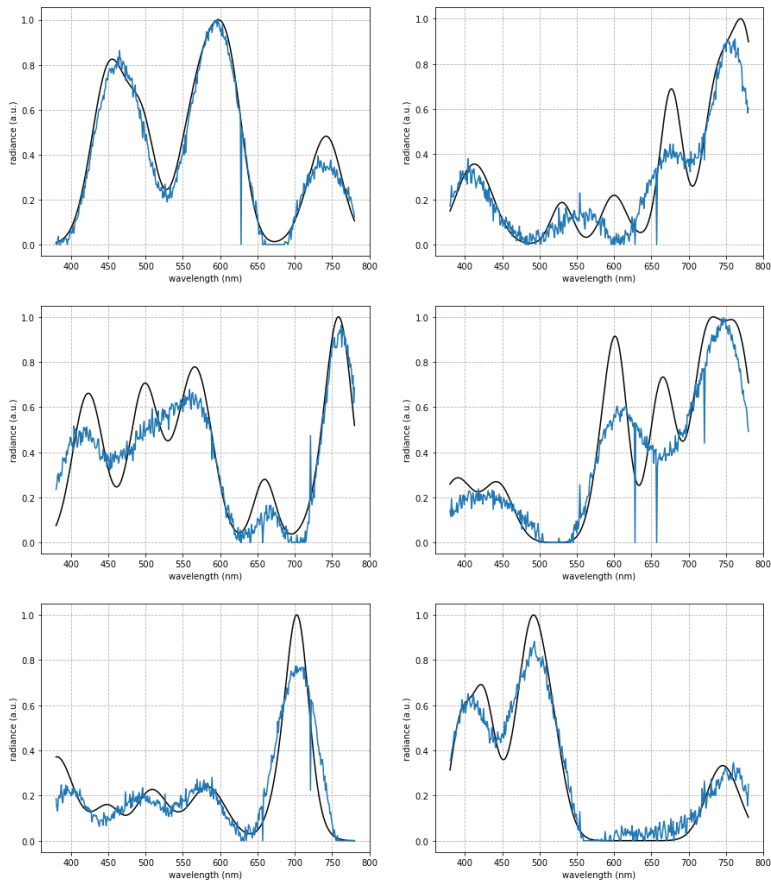


Figure 5-21. Example of spectral reconstruction of the simulated sensor measurements (blue) using a NN with a hidden layer with 128 neurons for randomly generated spectra (black solid line).

In Figure 5-21, the spectral reconstruction, in blue, is roughly fitted, containing a lot of noise and with some null values. This means that the NN has some bias, so it is not considering all the relevant information from the 14 sensor values to convert them into the 401 points of the SPD. The loss and accuracy values of the validation subset have been monitored as a function of the

number of iterations as the NN was training and complete stability has been achieved. This means that, if there is room for improvement, modifications to the design parameters must be made. Thus, this first iteration has served to have some initial reference values to make modifications to the architecture of the NN and to be able to achieve more accuracy.

After testing multiple configurations and trying to keep the NN as simple as possible by making small increases in the number of neurons, hidden layers or learning rates, a design has been chosen that performs an acceptable spectral reconstruction (Figure 5-22):

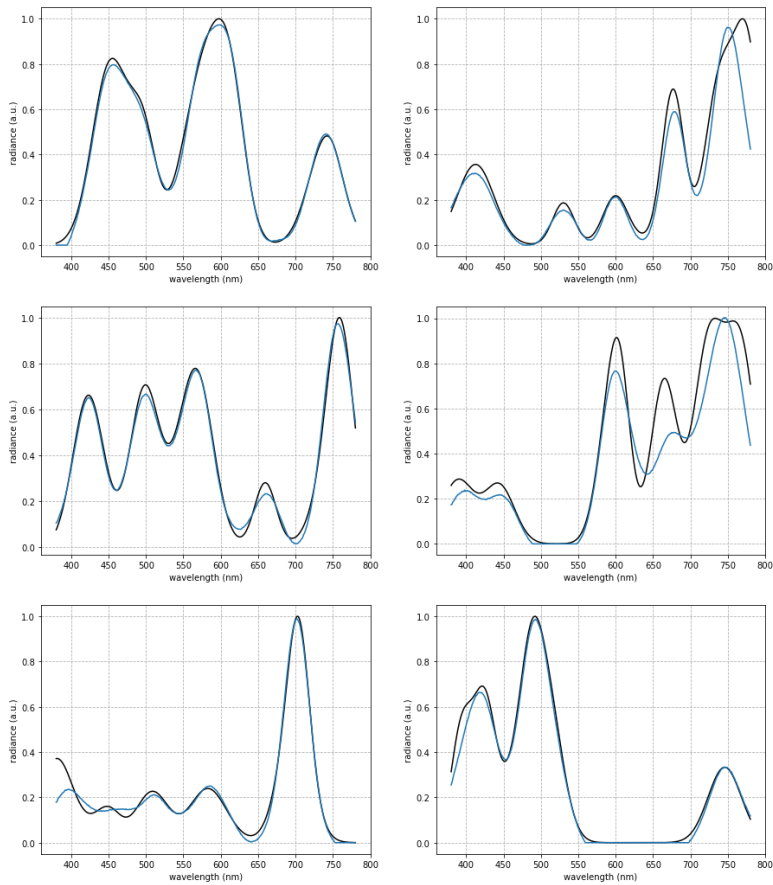


Figure 5-22. Example of spectral reconstruction of the simulated sensor measurements (blue) using a NN with two hidden layers with 2048 and 512 neurons for the randomly generated spectra (black).

As the NN was trained, the values of loss and accuracy have been monitored, resulting in the evolutions shown in Figure 5-23:

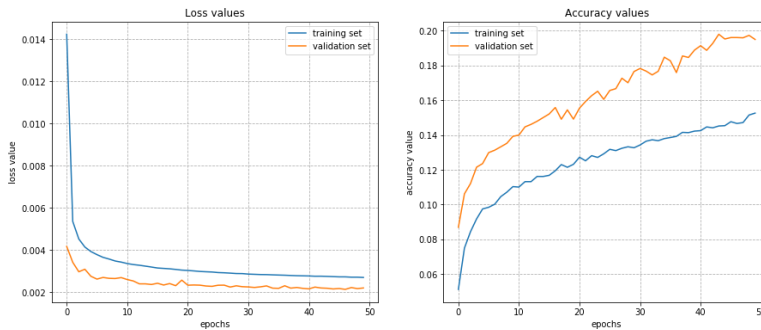


Figure 5-23. Evolution of the loss and accuracy values for the training (blue) and validation (orange) subsets as a function of the iterations in the NN training.

In this case, a NN with 4 layers has been used. The first (input layer) and the last (output layer) have 14 and 401 neurons respectively, exactly as in the previous case. In between there are 2 extra layers (hidden layers) with 2048 and 512 neurons. The activation function of all of them is a ReLu, while during training 10% of the neurons are deactivated to avoid overfitting. For the optimizer a SGD with a learning rate of 0.9 is used and the loss function performs a control of the MSE. As a second measure to avoid overfitting, a function has been configured that, if it detects that the loss value in the validation subset is not reduced in 5 consecutive iterations, the training process is terminated.

The results obtained in the test subsets for the parameters CCT, Ra and Rf can be seen in the Figure 5-24:

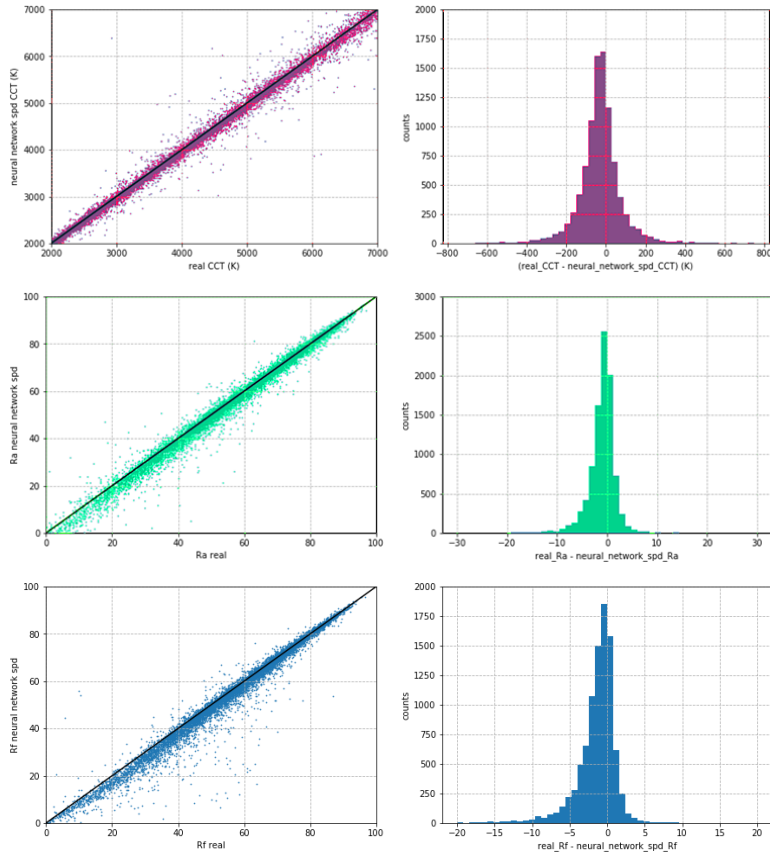


Figure 5-24. Comparison of the error in the calculation of CCT (purple), Ra (green) and Rf (blue) with respect to the real measurements for $2 \cdot 10^4$ random SPDs when the simulated sensor measurements are calculated through the spectral reconstruction NN (left column). Distribution of the error made in the calculation of CCT (purple), Ra (green) and Rf (blue) between the real values and those calculated through the spectral reconstruction NN (right column).

If the arithmetic mean, RMSE and standard deviation are calculated for the CCT, Ra and Rf values, the following values are obtained (Table 5-4):

Table 5-4. Arithmetic mean, RMSE and standard deviation associated with the error of the calculation of CCT, Ra and Rf for $2 \cdot 10^4$ random SPDs when sensor measurements are calculated through the spectral reconstruction NN.

	Neural Network SPD error		
	Arithmetic mean	RMSE	Standard deviation
CCT (K)	-31	144	141
CIE Ra	-1.1	3.3	3.1
IES TM-30-18 Rf	-1.5	3.9	3.6

5.1.7 Direct calculation of colorimetric parameters

On the other hand, the use of NN allows another radically different option: to directly calculate the values of CCT, Ra and Rf directly from the simulated sensor values used, without spectral reconstruction. In this way, 3 different NNs are created, one for each parameter to be calculated. The training process is equivalent to the one described above and the same set of randomly generated SPDs has been used. In this case, we will follow the schematic shown in Figure 5-25.

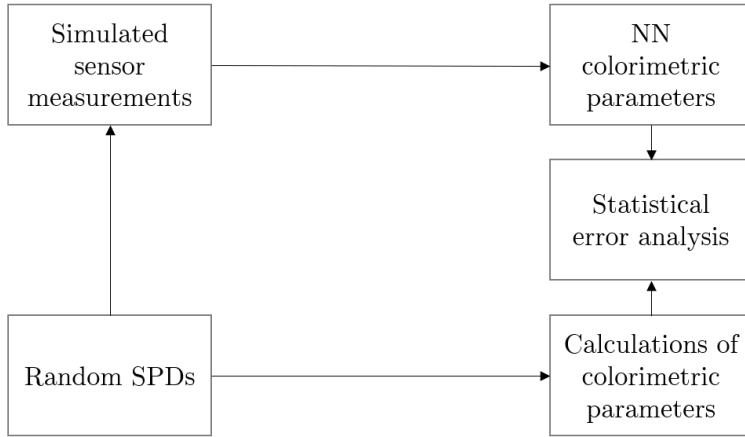


Figure 5-25. Schematic of the procedure to evaluate the error in the calculation of colorimetric parameters using the NN model of colorimetric parameter calculation.

The 3 new NNs (one for each colorimetric parameter) have been created following the same principle as described in the spectral reconstruction NN. We have started with a simple case and evaluated the values of the loss function, also linked to MSE. The same architecture as in the spectral reconstruction has been used for all 3 cases, although the output layer is a single neuron. The other difference is the optimizer, which in this case is a Root Mean Squared Propagation (RMSProp), which is an extension of Gradient Descent, with a learning rate of 0.0001.

The results obtained in each case are shown in Figure 5-26 in comparison with the real values of the calculated colorimetric parameters (CCT, Ra and Rf):

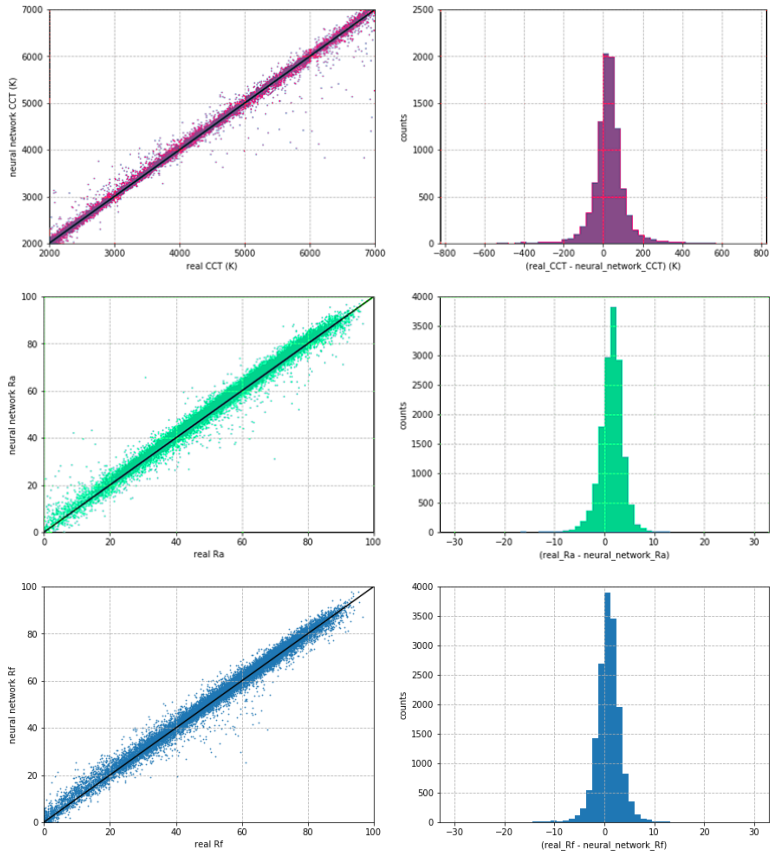


Figure 5-26. Comparison of the error in the calculation of CCT (purple), R_a (green) and R_f (blue) with respect to the real measurements for $2 \cdot 10^4$ random SPDs when the simulated sensor measurements are calculated through the NN for the calculation of the corresponding colorimetric parameter (left column). Distribution of the error made in the calculation of CCT (purple), R_a (green) and R_f (blue) between the real values and those calculated through the NN for the calculation of the corresponding colorimetric parameter (right column).

The statistical results of the error in the prediction of colorimetric parameters are also presented (Table 5-5, Table 5-6 and Table 5-7):

Table 5-5. Arithmetic mean, RMSE and standard deviation associated with CCT calculation error for $2 \cdot 10^4$ random SPDs when using a CCT calculation NN with the simulated sensor measurements as input.

CCT error (K)		
Arithmetic mean	RMSE	Standard deviation
25	162	160

Table 5-6. Arithmetic mean, RMSE and standard deviation associated with *Ra* calculation error for $2 \cdot 10^4$ random SPDs when using a NN for *Ra* calculation with the simulated sensor measurements as input.

CIE Ra error		
Arithmetic mean	RMSE	Standard deviation
1.4	2.9	2.6

Table 5-7. Arithmetic mean, RMSE and standard deviation associated with *Rf* calculation error for $2 \cdot 10^4$ random SPDs when using an *Rf* calculation NN with the simulated sensor measurements as input.

IES TM-30-18 Rf error		
Arithmetic mean	RMSE	Standard deviation
0.8	2.6	2.5

5.1.8 Comparison of all the models developed

Once the 4 different models have been analyzed (linear interpolation, cubic interpolation, spectral reconstruction NN and NNs for the calculation of colorimetric parameters), a comparison is made between the statistical values of the error committed in each case.

The arithmetic mean, RMSE and standard deviation values for each model is shown in Table 5-8:

Table 5-8. Summary of the arithmetic mean, RMSE and standard deviation values of the errors made in the different models used for $2 \cdot 10^4$ randomly created spectra. The smallest values for each case are marked in green.

	CCT error			CIE Ra error			IES TM-30-18 Rf error		
	Arithmetic mean	RMSE	Standard deviation	Arithmetic mean	RMSE	Standard deviation	Arithmetic mean	RMSE	Standard deviation
Linear interpolation	21	241	240	7.8	9.3	5.2	7.2	7.9	3.3
Cubic interpolation	13	131	130	3.5	4.4	2.6	3.4	3.8	1.7
Spectral reconstruction NN	-31	144	141	-1.1	3.3	3.1	-1.5	3.9	3.6
CCT NN	25	162	160	-	-	-	-	-	-
CIE Ra NN	-	-	-	1.4	2.9	2.6	-	-	-
IES TM-30-18 NN	-	-	-	-	-	-	0.8	2.6	2.5

Analyzing the results of the table above, it can be concluded that, for the subtest test with $2 \cdot 10^4$ randomly generated spectra, it is necessary to use different models for the calculation of different parameters.

In the case of the CCT, the model that obtains the best results is the cubic interpolation, obtaining the smallest errors in both the arithmetic mean, the RMSE and the standard deviation.

For the calculation of Ra , the best model is the Ra calculation NN. Although the spectral reconstruction NN has (narrowly) a better central value, the Ra computational NN has more precision and less scatter.

Finally, in the Rf calculation, the best model is the NN for Rf calculation. It has an error in the central value of less than unity and is the most accurate. The cubic interpolation model has a lower dispersion, but the central value is much farther away, so that the calculations are displaced with respect to the real values.

5.1.9 Using a real set of white LED-sources

Next, the randomly created spectra are replaced by a database with real experimental measurements consisting of 1495 SPDs of white LED-sources collected by the partners and collaborators of the project "EMPIR 15SIB07 PhotoLED - Future Photometry Based on Solid-State Lighting Products". Within this database SPDs can be found for different products manufactured between 2009 and 2016 ranging from bulbs, tubes, streetlamps, LED strips, downlights, etc., from a large number of manufacturers [118]. Sources with a CCT between 1000 K and 10000 K have been filtered and invalid data have been removed, resulting in 1479 distinct SPDs. A representation of the first 25 spectral distributions of the database can be seen in Figure 5-27:

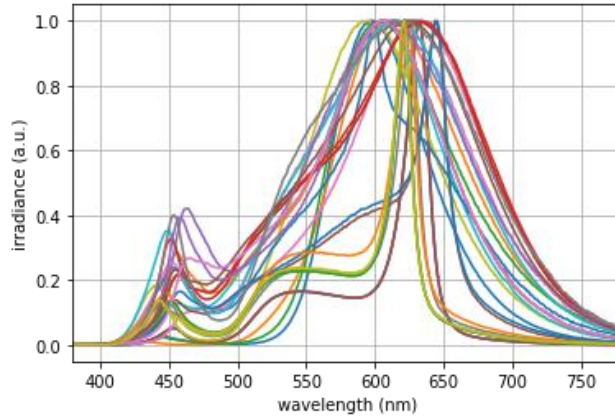


Figure 5-27. Example of the first 25 normalized spectral distributions from the database of real LED-sources.

If we apply the same models described and developed above, we obtain the following results (Table 5-9):

Table 5-9. Summary of the arithmetic mean, RMSE and standard deviation values of the errors made in the different models used for the 1479 SPDs in the real LED-source database. The smallest values for each case have been marked in green.

	CCT error			CIE Ra error			IES TM-30-18 Rf error		
	Arithmetic mean	RMSE	Standard deviation	Arithmetic mean	RMSE	Standard deviation	Arithmetic mean	RMSE	Standard deviation
Linear interpolation	-10	149	149	0.8	1.9	1.8	2.6	3.0	1.5
Cubic interpolation	-6	96	96	0.5	1.3	1.2	1.4	1.7	0.9
Spectral reconstruction NN	-1	87	87	0.2	1.0	0.9	0.0	1.7	1.7
CCT NN	7	85	85	-	-	-	-	-	-
CIE Ra NN	-	-	-	2.6	3.2	1.8	-	-	-
IES TM-30-18 NN	-	-	-	-	-	-	0.6	1.6	1.5

In this case, unlike the case of randomly created spectra, we see how the spectral reconstruction NN stands out above the other models in most of the sections. This is because this NN has been designed to reconstruct complex spectral distributions, with numerous peaks and valleys, and now encounters much simpler cases. Although the spectral fit is not perfect, it allows to obtain the values of CCT, Ra and Rf with very little associated error.

Comparative plots between the real CCT, Ra and Rf values and the values predicted by the spectral reconstruction NN for the set of SPDs of the real LED-source database are shown below. In the case of the error distribution, the same ranges have been maintained on the axes of the Figures as in the previous sections so that the difference can be visually displayed.

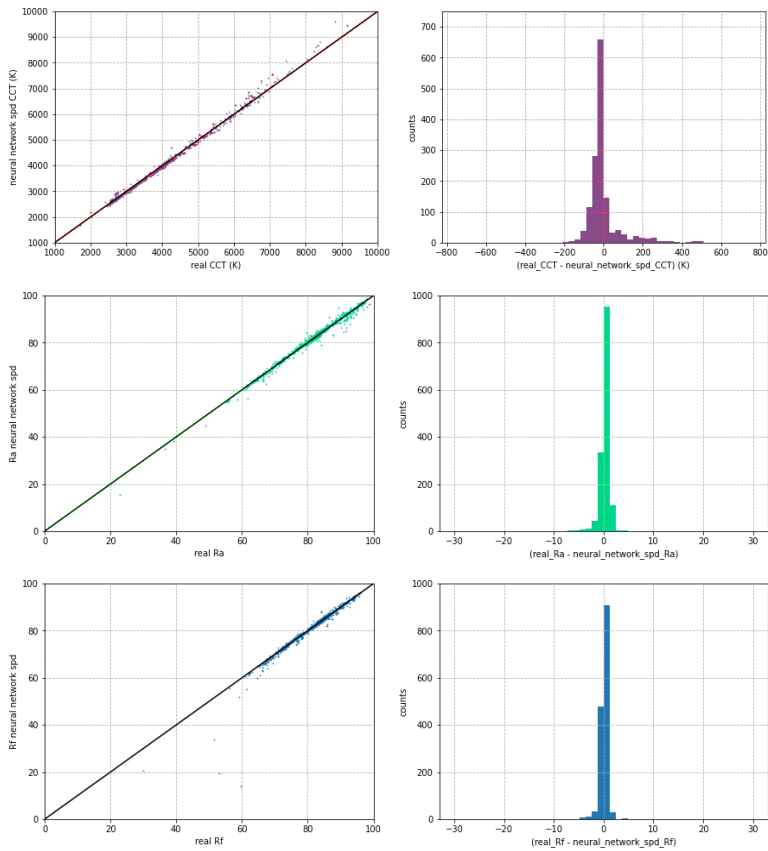


Figure 5-28. Comparison of the error in the calculation of CCT (purple), *Ra* (green) and *Rf* (blue) with respect to the real measurements for a set of 1479 real LED-sources using a spectral reconstruction NN (left column). Distribution of the error made in the calculation of the corresponding colorimetric parameter between the real values and those calculated through the spectral reconstruction NN (right column).

The charts in Figure 5-28 present a very good fit of the three colorimetric parameters considered, which explains the statistical parameters obtained in Table 5-9.

The Figure 5-29 shows the spectral reconstruction in 6 randomly chosen distributions from the real LED-source database used.

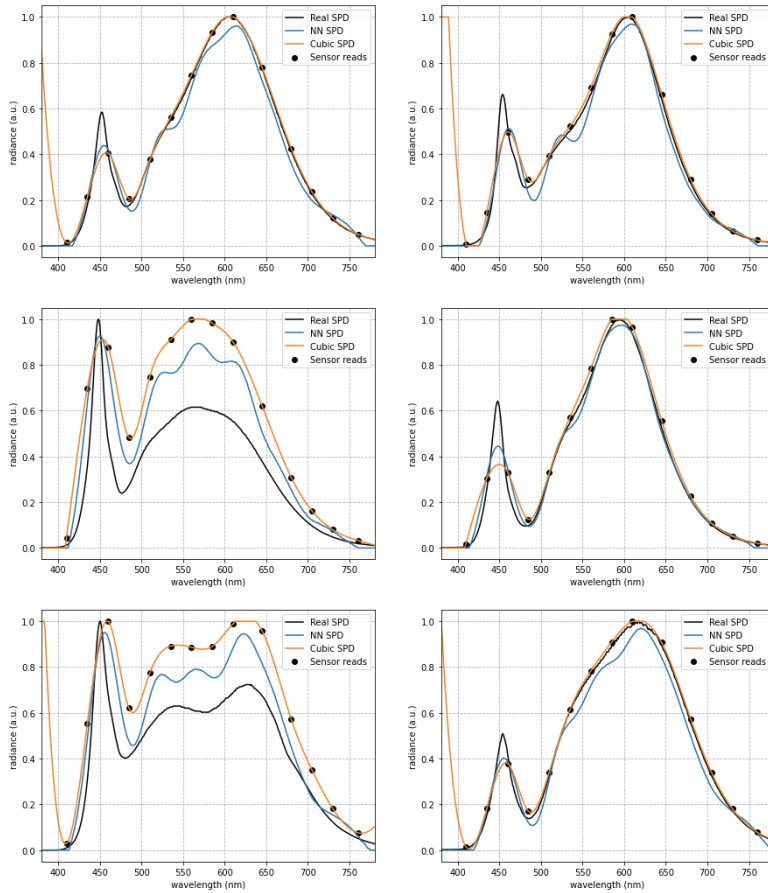


Figure 5-29. Comparison between the real SPD (black), the one created by the spectral reconstruction NN (blue), the cubically interpolated one (orange) and the simulated sensor values (black dots).

In Figure 5-29 it is possible to see how the spectral reconstruction model created through a NN is able to correctly approximate the real values of the SPD. In some cases, the fit is very similar to

that provided by cubic interpolation, but especially at high CCTs, the fit is substantially better. In addition, it can be observed that, in cubic interpolations, for the smallest wavelengths there is a sudden increase in irradiance, which does not happen in the NN approximation.

This database has been used only to test the accuracy of the models developed in standard white illumination. If it had been used as a database for training NNs, the results would only be valid for white LED lighting, having a large error in other more advanced systems, such as multichannel LED systems incorporating monochromatic LEDs. In addition, a large amount of data is needed to train NNs, much larger than that provided by this database.

5.2 Color sensor for experimental verification

Later, working in a real environment, a multichannel colorimetric sensor has been used and calibrated to read values compatible with the simulated module.

Now that it has been shown that it is possible to use a spectral reconstruction NN to calculate colorimetric parameters theoretically, the next step is to perform the implementation to a real sensor linked to a microcontroller. The scheme described in Figure 5-1 and Figure 5-2. will be followed. An I²C connection has been established between the sensor and the microcontroller and the results are sequentially sent to the computer using a serial connection through a USB port.

In order to have an encapsulated design, a custom housing has been designed using Tinkercad software [119] and printed using a Prusa i3 MK3S+ printer [120] with PLA material. The result can be seen in Figure 5-30:



Figure 5-30. Side and top view of the AS7265x module and ATSAM21G18 microcontroller breakout boards.

Calibration of the module is a necessary step to obtain consistent SPD values from the measured light sources. According to the datasheet, the components that integrate the AS7265x module are pre-calibrated with a specific light source, to collect the reflected values on objects. If it is to be used for other applications, such as measuring light sources directly, a new calibration is required.

For the calibration process of the AS7265x module, 5 different factors have been considered:

- Acquisition temperature. The datasheet specifies that the module's colorimetric sensor filters are not very temperature-dependent, although depending on the electronic design and the boundary conditions, the temperature variation while taking measurements can be large. For this reason, the commercial module incorporates a temperature sensor. As a consequence, the temperature was monitored while taking measurements and it was found that the stabilization time was 10 minutes at an ambient temperature of 20 °C, reaching a constant value of 34 °C.
- Dark measurement. Measurements have been performed with absolute darkness to know the background value of the sensor. In this case it has been observed that most of the module channels marked a value of 0 in the process of experimental measurements, so it has not been necessary to extract the dark measurement in these cases. However, a small signal was observed in the S

channel, so it will be subtracted from the values of the experimental measurements.

- Linearity with respect to intensity for each channel. The values of the sensor channels have been experimentally measured for different light intensities. It was found that, although the response is not completely linear, there is a very similar deviation with respect to linearity between the different channels. Since for the calculation of the colorimetric parameters mentioned (*CCT*, *Ra* and *Rf*) only the spectral shape is important, and not the intensity, it can be considered linear for this use. The relative response (in percentage) of each channel as a function of the relative brightness (also in percentage) of a light source can be seen in Table 5-10:

Table 5-10. Relative response of the different channels (A, B, C, D, E, F, G, H, I, J, R, S, T and U) of the AS7265x module as a function of the relative brightness of a light source.

Brightness level	A	B	C	D	E	F	G	H	I	J	R	S	T	U
100	100	100	100	100	100	100	100	100	100	100	100	100	100	100
90	91	89	91	91	90	90	90	90	90	91	90	90	90	91
80	81	80	81	81	80	81	81	81	80	81	80	81	80	81
70	73	72	73	73	72	73	72	72	72	73	72	72	72	72
60	64	63	63	64	64	64	64	64	63	64	64	64	63	63
50	54	54	54	54	54	55	55	54	54	55	54	54	54	54
40	45	45	44	45	45	46	45	45	45	46	46	45	45	45
30	36	37	36	37	37	37	37	37	37	37	37	37	36	36
20	27	28	27	27	28	28	28	28	28	28	28	28	27	27
10	18	19	18	18	19	19	19	19	19	19	19	19	18	18

- Correction of the response of each channel. The datasheet does not mention at any point the differences

in the spectral response of the different sensor channels. In Figure 5-5 it can be seen how all the peaks of the sensor channels are at the same height, and this has also been used in the sensor simulation (Figure 5-7). However, it is important to implement a calibration curve to obtain valid values with the corrected response. Thus, a calibration lamp (halogen, continuous SPD) was used, and its SPD was obtained with a calibrated spectrometer. Subsequently, the theoretical values of the calibrated SPD have been calculated with the simulated sensor and finally the values of the real sensor have been obtained experimentally. The vector containing the quotients of the simulated and experimental values of the sensor is the transfer function used as the calibration curve.

- Aperture angle. According to the module specifications, the aperture of the sensors is only 20.5° , which means that the module must point directly at the light source. In this case, a reflecting surface similar to those inside the integrating spheres has been used to increase the stability of the measurements when using different consecutive light sources.

5.3 Results

Once the spectral reconstruction model was chosen using NNs and the calibration process was implemented, experimental measurements of different light sources at different CCTs were performed. A sample of 15 commercial bulbs emitting white light, either static, tunable white or RGBW, was used. In total, 31 SPDs derived from the set of bulbs have been measured (Table 7-3) using the UPRtek MK350S premium calibrated portable spectrometer (providing the real values) and the AS7265x module running with the spectral reconstruction NN.

Comparative values between the real measurements with the spectrometer and the spectral reconstructions for the CCT, Ra and Rf parameters using the AS7265x module can be seen in Figure 5-31:

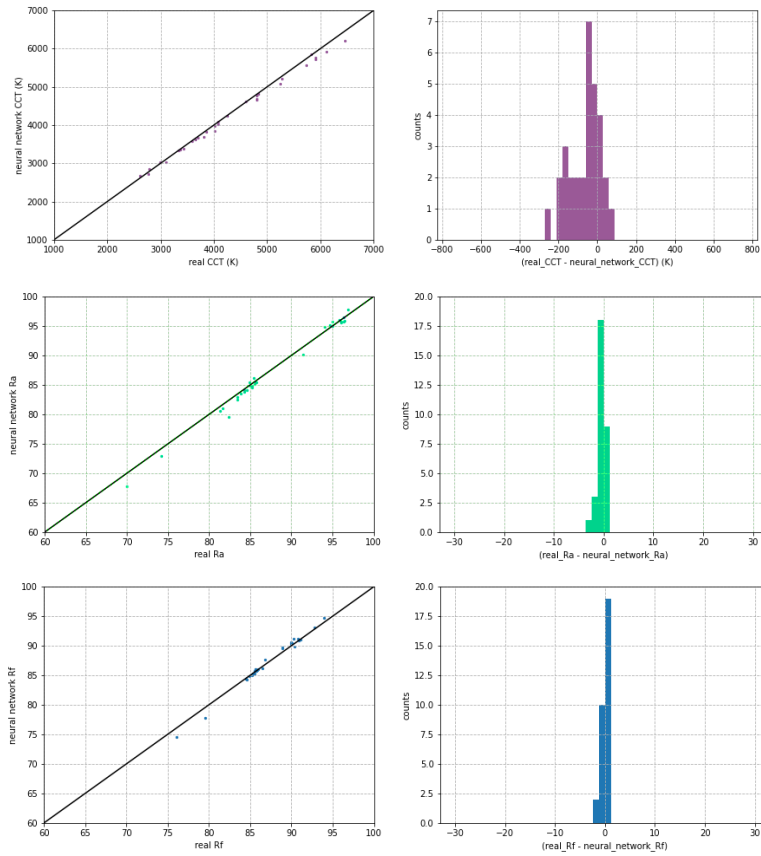


Figure 5-31. Comparison of the error in the calculation of CCT (purple), Ra (green) and Rf (blue) with respect to experimental measurements for a set of 31 SPDs from real LED-sources using a spectral reconstruction NN (left column). Distribution of the error made in the calculation of the corresponding colorimetric parameter between the real values and those calculated through the spectral reconstruction NN (right column).

The following statistical values were obtained for the 31 SPDs measured (Table 5-11):

Table 5-11. Summary of the arithmetic mean, RMSE and standard deviation values of the errors made in the experimental measurements of 31 different SPDs.

	CCT error			CIE Ra error			IES TM-30-18 Rf error		
	Arithmetic mean	RMSE	Standard deviation	Arithmetic mean	RMSE	Standard deviation	Arithmetic mean	RMSE	Standard deviation
Spectral reconstruction NN	64	102	80	-0.4	0.9	0.8	0.1	0.6	0.6

In this case there is a slight increase in most of the calculated parameters with respect to those marked in green in Table 5-9, which provided the theoretical values of this NN operating on a set of SPDs of real light sources. This increase is due to the differences between the simulated and the real sensor. In addition to the imperfections produced during the calibration process, the AS7265x module datasheet itself provides errors not previously contemplated, as could 20 nm associated to the channel peak wavelength, a 12% error in counts/ $\mu\text{W}/\text{cm}^2$ or to a non-Gaussian distribution of each channel.

To know whether the results are acceptably good or not, we can compare the data with the margins of error of a commercial spectrometer. To do this, we look at the UPRtek MK350S premium calibrated portable spectrometer, the same spectrometer with which we have made the measurements. In its datasheet, it specifies that it has an error of 2% in the CCT calculation and 1.5% in the Ra calculation. Figure 5-32, Figure 5-33 and Figure 5-34 show the relative error of the sensor compared to the error of the spectrometer:

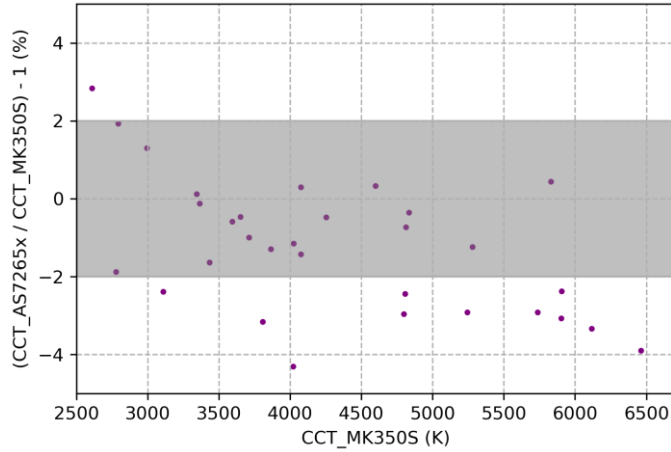


Figure 5-32. Relative error of the CCT of the AS7265x sensor with respect to the MK350S spectrometer. The points within the gray area are the points within the margin of error.

In the case of the CCT, as can be seen in Figure 5-32, 61% of the points are within the error margins. Although they are the majority, the error of the AS7265x sensor when calculating the CCT through spectral reconstruction by NN is substantially higher than that provided by the MK350S spectrometer.

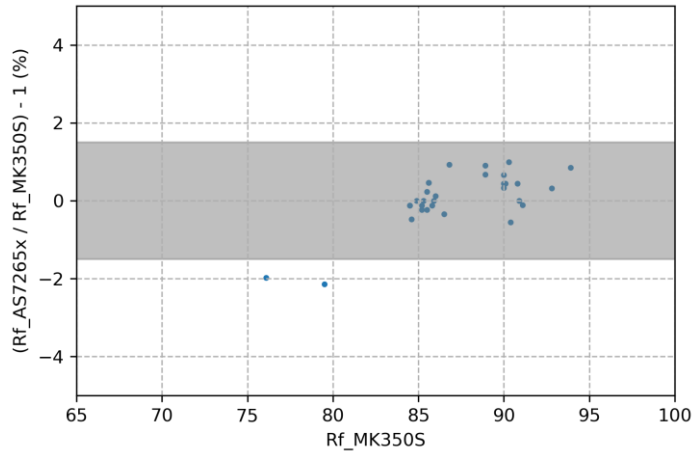


Figure 5-34. Relative error of the Rf of the AS7265x sensor with respect to the MK350S spectrometer. The points within the gray area are the points within the error margin.

The Rf analysis presents 94% of the points within the error margins of the spectrometer, even improving the Ra results.

On the other hand, since the NN loaded to the AS7265x sensor performs a spectral reconstruction, the SPDs measured with the sensor can be reconstructed. As an example, some of the results with the reconstructed SPDs can be seen in the Figure 5-35:

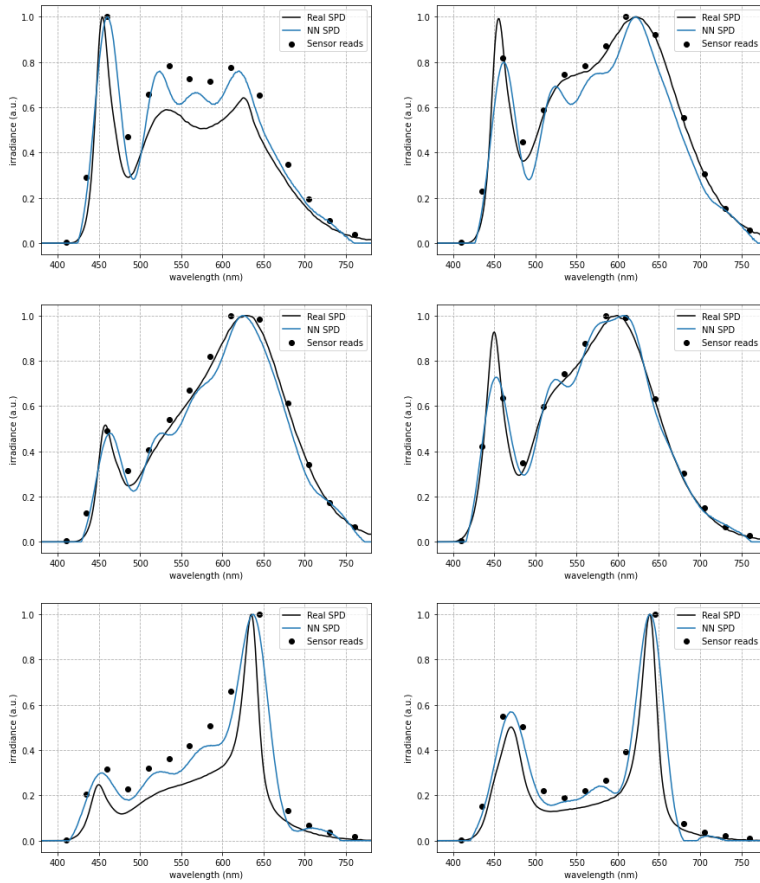


Figure 5-35. Real SPD (black line), spectral reconstruction (blue line) and AS7265x module values (black dots) for 6 of the 31 measured SPDs.

In addition, to obtain the values of the AS7265x module, a small graphical user interface (GUI) has been designed using the Flask framework [121] in order to obtain the spectra in an easy way, in addition to visualizing the CCT, Ra and Rf while taking measures (Figure 5-36).

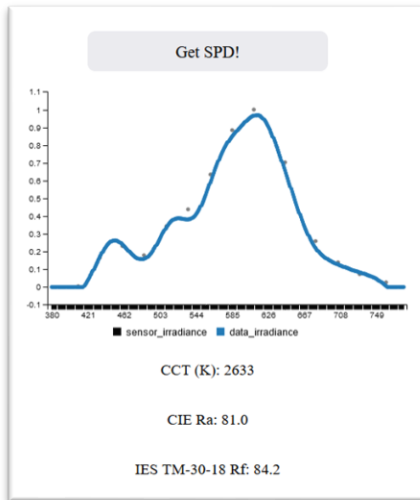


Figure 5-36. User interface designed where the colorimetric sensor values (sensor_irradiance, black dots) and spectral reconstruction (data_irradiance, blue line), as well as CCT, R_a and R_f values can be obtained.

6 Conclusions

This work has been focused on one main objective: to implement new algorithms for light emission and collection. To achieve this, the algorithms were first designed at a theoretical level and then applied to different experimental devices.

6.1 Conclusions

The following is a summary of the work carried out for each of the objectives and general conclusions:

- Objective 1: Developing new algorithms that can be incorporated in multichannel lighting systems to reach new applications. These algorithms are designed to obtain optimized values of colorimetric, non-visual and energy efficiency parameters throughout the chromaticity diagram, mixing the light of the different LED channels of the luminaire. Specifically, the new algorithms must be able to return results separated by 0.01 units in the CIE 1976 chromaticity diagram with an $R_f > 80$, even outside the Planckian locus.

A new algorithm based on brute force has been developed to obtain optimized values for different colorimetric, non-visual and energy efficiency parameters. This algorithm generates a huge amount of results spread all over the chromaticity diagram and then filtered according to the chosen optimization parameter and its position within the chromaticity diagram itself. The results are provided according to the needs of the control system, which can be through the control of the CCT or through the control of the chromaticity diagram coordinates. Thanks to the use of this algorithm, it is possible to obtain high values of R_a and R_f at points far from the Planckian locus, separated by 0.01 units in the CIE 1976 chromaticity diagram.

Within the spectral generation process, a project for hospital lighting has been carried out. For this purpose, we have been awarded with a SHAPE project, and we were granted access to BSC MareNostrum for the calculation of combinations at high resolution (32 steps). In the process, the code has been optimized to be run on a supercomputer with 9600 cores. To try to improve the results, another optimization algorithm based on gradient descent has been created that works in parallel with the brute force algorithm. The results show an improvement in the optimization of colorimetric parameters such as R_f , and non-visual parameters such as M/P ratio.

In addition, a study between colorimetric and non-visual parameters has been performed for a set of commercial white LEDs and for a multichannel LED system. In the case of commercial white LEDs, a common pattern can be observed: for the same CCT, generally the melanopic impact will be higher if the R_f is higher. This relationship is lost in light generated by LED multichannel systems. The relationships found in this section were published in the LED Professional Symposium 2020 in the form of a digital conference and to the LED Professional Review magazine in the Sept/Oct issue of the same year. The paper was awarded the Best Scientific Lecture/Paper – Technology Award 2020.

- Objective 2: Creating prototypes to be incorporated in a showroom that have the results of the developed algorithms in the microcontroller memory. Experimental measurements of the created prototypes will be performed, and their quality will be checked through the ANSI C78.377-2015 standard. In addition, tests will be performed on a commercial device. It is expected that at least half of the measured points will pass the quality test, both in the prototypes and in the commercial device.

Once the theoretical results have been obtained, prototypes have been built to validate the results experimentally. To this end, prototypes have been developed in 3 different phases until a final version adapted to standard market housings has been obtained. In this final version, the components are directly soldered to the respective PCBs, being made of aluminum in the case of the LEDs.

A customized control system has been developed that allows direct control of the CCT and colorimetric coordinates in the prototypes. In addition, it is possible to connect a spectrometer to perform measurements and obtain relevant colorimetric parameters. The control system can be wired (via USB) or wireless (via Wi-Fi).

At the thermal level, the developed prototypes work within reasonable margins. In the case of the bulb prototype, approximately 50 °C is reached on the

control PCB and the LED PCB. In the case of the floodlight, 60 °C is reached on both PCBs and in the case of the downlight, 45 °C is also reached on both PCBs. In all cases these values are very acceptable and below the specifications of the components used.

To evaluate the accuracy of the results, the ANSI C78.377-2015 standard was used. We proceeded to load the results of the theoretical algorithm (with the Rf as optimization parameter) to the developed prototypes and experimentally measured the deviations of the theoretical coordinates (u' , v') with respect to those emitted by the prototypes. In all cases, theoretical results with a minimum Rf of 80 have been chosen. In the case of the bulb, 84% of the emitted points comply with the standard, while in the case of the downlight it is complied with in 100% of the cases. Furthermore, when controlled using the CCT, the spectral mix achieves an increase of more than 10 Rf points compared to the Rf of white LEDs alone, both in the bulb and in the downlight.

Some of the prototypes developed, the downlights and bulbs, were installed in a showroom of the company Kumux, located in Parc Científic de Barcelona. The installed prototypes were working there for 3 years until the company moved to a new office. During this time, the prototypes have been used to show the developed spectral technology to numerous companies in the sector.

Finally, the error in a commercial device with tunable white control has also been evaluated. In this case the deviation in CCT was measured and again compared to the ANSI C78.377-2015 standard. All measured points have fallen within the error margins of the standard.

- Objective 3: Developing algorithms that allow a light sensor to provide CCT, Ra and Rf values in an accurate way. We have incorporated four different types of spectral reconstruction models to perform a calculation of colorimetric properties, making a comparison between the models through different statistical parameters related to the error and choose a candidate to be implemented to a prototype.

A multichannel colorimetric sensor (AS7265x) with 14 channels within the visible range has been simulated and a random SPD generation script has been generated. With this, 10^5 different SPDs have been generated and the values obtained by the sensor have been simulated.

Once all the necessary data had been generated, a comparison was made between 4 different models to calculate the CCT, Ra and Rf . The points generated by the sensor have been treated through a linear interpolation, a cubic interpolation, a spectral reconstruction NN and a NN to directly obtain colorimetric parameters. After analyzing the preliminary results, a database of 1495 commercial white LED-sources was used to choose the model with the least error

in the predictions. The model with the lowest overall error was the spectral reconstruction NN.

- Objective 4: Creating a prototype with the improved light sensor to validate the development. This prototype will have the chosen spectral reconstruction algorithm incorporated and measurements of commercial lighting systems will be performed. The relative error between the created prototype and a professional spectrometer will be calculated, expecting at least half of the measured points to be within the error margins (2% for the CCT and 1.5% for Ra and Rf).

To test the spectral reconstruction NN, a prototype has been developed incorporating the AS7265x module connected to a microcontroller, which in turn is connected to a computer with the NN running. The system has been calibrated considering factors such as acquisition temperature, dark measurements, relative linearity between channels, the calibration curve itself or the aperture angle.

To obtain the results, 31 different SPDs were measured, and the values obtained by the AS7265x module and the UPRtek MK350S premium calibrated portable spectrometer were compared. A small increase of the error with respect to the theoretical results has been detected due to the imperfections of the experimental system.

To evaluate the error committed, the relative errors between the spectrometer and the module have been evaluated and a comparison has been made with reference to the error range of the spectrometer datasheet. 61% of the SPDs calculated by the module fall within the error margins considered, while in the case of *Ra* it rises to 90%. Finally, for *Rf*, 94% of the values fall within the error margins.

6.2 Future work

A series of possible future improvements affecting both the spectral emission part and the sensing part are discussed below.

6.2.1 Light emission

As seen in section 5.1.7, it is possible to obtain CCT, Ra and Rf values with certain precision using NNs and only 14 points within the visible range. In the same way, it is also possible to obtain the values of these colorimetric parameters using the 401 points corresponding to the visible range from 380 nm to 780 nm, both included. In addition to providing a totally different way of calculating colorimetric parameters, using NNs can greatly optimize the calculation time when many operations are required. For example, using the Luxpy library, on an Intel Core i7-8565U processor, $2 \cdot 10^4$ Ra calculations can be performed in 91.4 s, while using NNs they can be calculated in 1.38 s, 98.5% less time.

This type of development can be included in spectral optimization procedures that require a very large number of operations, as in the case of the brute force algorithm. Since NN calculations will always have an associated error, even if it is small, they can be used to perform a first sweep and find those points that may be of interest. Later, classical calculation libraries can be used to finish refining the value if necessary. This process would significantly increase the performance of the algorithm and more accurate theoretical results could be obtained.

6.2.2 Light sensing

At the simulation level, one way to improve results for better accuracy with both standard white lighting and more advanced LED systems is to perform clustering prior to spectral reconstruction. Supervised clustering is a technique defined within the ML environment that can be used to separate data sets and assign them to a group. Applied to our problem, it would serve to differentiate white LEDs from monochromatic LEDs and LED multichannel systems. Different spectral reconstruction techniques could be applied depending on the SPD classification. For example, in the CCT calculation, one could use cubic interpolation in case of measuring a multichannel LED-source or use spectral reconstruction NN in case of measuring a white LED-source.

Another possible improvement at the simulation level is to use a larger real data set. Currently there is no spectral database of light sources large enough to be able to train a NN in good conditions. If such a database is created, it can be used as a basis for better results in the future. However, it should be noted that in a NN the results obtained depend dramatically on the data used during training. Therefore, if a database of white LED light sources were used, the results would only be valid for this type of light sources. It would most likely increase the accuracy of the predictions when measuring white LED-sources, but they would also be very limited to this condition.

At the device level, there is a noticeable variation in the channel values of the AS7265x module depending on the angle of

incidence of the light. To avoid this problem, a lens providing a larger aperture can be incorporated. Moreover, a light mixing element, such as a diffuser, can be used. This would greatly simplify the use of the sensor since it could be used without having to constantly check the angle of incidence of the light.

7 Supplementary tables

Table 7-1. Light bulb prototype measurements.

u' theo	v' theo	u'	v'	CCT (K)	R_a	R_f	R_g	Div	Luminous Flux (lm)
0.1700	0.4800	0.1707	0.4797	7308	86.0	82.9	91.5	0.0311	863
0.1700	0.4900	0.169	0.4909	6776	87.7	83.4	93.7	0.0366	866
0.1800	0.4600	0.1798	0.4601	8166	88.2	82.0	91.0	0.0165	861
0.1800	0.4700	0.179	0.4709	7370	89.3	85.3	92.8	0.0209	864
0.1800	0.4800	0.1808	0.4814	6629	91.7	88.8	95.4	0.0233	860
0.1800	0.4900	0.1794	0.4901	6279	91.2	87.5	95.5	0.0278	860
0.1800	0.5000	0.1786	0.5004	5895	89.2	83.1	93.4	0.0327	859
0.1900	0.4600	0.1906	0.4602	7342	92.8	87.2	94.7	0.0072	860
0.1900	0.4700	0.1911	0.4712	6585	95.4	91.4	96.9	0.0110	863
0.1900	0.4800	0.1904	0.4813	6099	95.4	92.8	99.3	0.0156	866
0.1900	0.4900	0.1893	0.4905	5770	94.2	90.7	97.3	0.0203	857
0.1900	0.5000	0.1892	0.5002	5430	90.8	86.4	94.0	0.0246	855
0.2000	0.4600	0.2015	0.461	6521	92.6	88.5	99.8	-0.0015	865
0.2000	0.4700	0.2009	0.4704	6029	98.0	93.2	100.1	0.0028	855
0.2000	0.4800	0.2006	0.4805	5591	97.8	94.6	100.6	0.0074	854
0.2000	0.4900	0.1997	0.4895	5308	96.9	93.8	99.7	0.0120	857
0.2000	0.5000	0.1996	0.4999	4991	93.7	89.3	96.5	0.0169	853
0.2000	0.5100	0.1989	0.5096	4770	90.4	83.3	92.6	0.0221	851
0.2100	0.4700	0.2124	0.4713	5319	92.8	90.6	102.2	-0.0055	857
0.2100	0.4800	0.2113	0.4801	5057	97.7	93.5	101.1	-0.0007	854
0.2100	0.4900	0.2103	0.49	4799	98.5	94.4	100.7	0.0048	854
0.2100	0.5000	0.2103	0.5	4549	96.8	91.6	98.1	0.0098	855
0.2100	0.5100	0.2112	0.5092	4321	94.0	87.0	95.4	0.0140	853

0.2200	0.4700	0.2218	0.471	4811	83.3	84.9	105.6	-0.0123	853
0.2200	0.4800	0.2217	0.4795	4560	93.2	90.5	101.4	-0.0080	854
0.2200	0.4900	0.2219	0.49	4291	97.7	93.9	102.3	-0.0027	855
0.2200	0.5000	0.2206	0.4998	4145	98.7	94.3	100.4	0.0033	855
0.2200	0.5100	0.2204	0.509	3993	95.8	90.2	97.2	0.0084	853
0.2300	0.4800	0.232	0.4807	4055	85.2	87.4	105.9	-0.0137	857
0.2300	0.4900	0.2324	0.4904	3857	95.8	93.1	102.9	-0.0086	855
0.2300	0.5000	0.232	0.4997	3729	98.1	95.2	102.4	-0.0031	850
0.2300	0.5100	0.2312	0.5091	3631	97.0	93.4	99.7	0.0027	848
0.2400	0.4800	0.2452	0.48	3521	72.8	80.7	110.0	-0.0211	851
0.2400	0.4900	0.2414	0.4905	3520	88.9	90.7	105.4	-0.0131	858
0.2400	0.5000	0.2434	0.4994	3351	94.2	93.2	105.7	-0.0088	856
0.2400	0.5100	0.242	0.5091	3299	97.1	95.3	102.7	-0.0023	855
0.2500	0.4900	0.2551	0.4893	3082	76.6	83.3	106.7	-0.0197	852
0.2500	0.5000	0.2519	0.5004	3088	92.2	93.1	104.7	-0.0116	858
0.2500	0.5100	0.253	0.5088	2997	96.8	94.8	104.1	-0.0068	857
0.2400	0.5200	0.2392	0.5173	3304	92.1	87.6	97.5	0.0038	854
0.2600	0.5000	0.2648	0.4989	2759	81.7	86.8	106.3	-0.0169	854
0.2600	0.5100	0.2649	0.5095	2708	93.6	93.5	105.7	-0.0102	854
0.2600	0.5200	0.2551	0.5179	2893	94.2	93.3	102.0	-0.0019	849
0.2700	0.5000	0.2742	0.4986	2549	75.2	82.6	108.6	-0.0196	850
0.2700	0.5100	0.2735	0.5088	2530	87.8	90.0	109.0	-0.0128	852
0.2700	0.5200	0.271	0.5181	2475	95.0	94.2	104.6	-0.0071	852
0.2800	0.5100	0.2838	0.5079	2341	80.5	84.5	113.7	-0.0155	850
0.2800	0.5200	0.2825	0.5177	2342	92.3	92.5	105.4	-0.0089	862
0.2900	0.5100	0.2898	0.508	2241	77.7	83.3	108.5	-0.0165	842
0.2900	0.5200	0.2901	0.5158	2224	86.6	88.9	108.4	-0.0114	861

Table 7-2. Downlight prototype measurements.

u' theo	v' theo	u'	v'	CCT (K)	R_a	R_f	R_g	D_{uv}	Luminous Flux (lm)
0.1700	0.4700	0.1696	0.4680	8505	85.7	80.8	90.5	0.0270	1983
0.1700	0.4800	0.1692	0.4817	7464	85.4	82.7	91.5	0.0320	1991
0.1700	0.4900	0.1693	0.4884	7223	87.1	82.4	92.8	0.0332	1981
0.1800	0.4500	0.1793	0.4483	9922	87.1	80.8	90.7	0.0124	1982
0.1800	0.4600	0.1793	0.4613	8377	90.0	84.8	92.6	0.0164	1985
0.1800	0.4700	0.1791	0.4695	7680	90.3	86.6	94.3	0.0192	1979
0.1800	0.4800	0.1796	0.4802	6926	90.8	88.8	95.9	0.0227	1990
0.1800	0.4900	0.1808	0.4902	6334	92.0	86.6	95.9	0.0256	1967
0.1800	0.5000	0.1774	0.5002	6072	87.1	80.9	91.7	0.0323	1958
0.1900	0.4500	0.1901	0.4482	8837	90.7	85.2	94.9	0.0027	1981
0.1900	0.4600	0.1900	0.4589	7745	94.8	89.2	97.1	0.0062	1976
0.1900	0.4700	0.1898	0.4701	6914	96.8	92.6	98.7	0.0104	1985
0.1900	0.4800	0.1896	0.4800	6350	95.9	93.4	99.8	0.0144	1989
0.1900	0.4900	0.1887	0.4895	5962	94.3	90.3	97.5	0.0191	1963
0.1900	0.5000	0.1877	0.5001	5601	90.1	84.9	93.6	0.0243	1953
0.2000	0.4500	0.2008	0.4487	7786	87.9	85.3	100.5	-0.0065	1982
0.2000	0.4600	0.2008	0.4590	6910	95.5	91.2	101.1	-0.0028	1992
0.2000	0.4700	0.1999	0.4712	6206	98.8	94.7	100.9	0.0027	1966
0.2000	0.4800	0.1996	0.4796	5809	98.3	95.4	101.2	0.0064	1974
0.2000	0.4900	0.1990	0.4900	5429	97.0	93.2	99.2	0.0114	1955
0.2000	0.5000	0.1981	0.4995	5153	93.8	88.6	96.0	0.0164	1942
0.2000	0.5100	0.2000	0.5107	4776	89.1	81.7	91.6	0.0205	1941
0.2100	0.4600	0.2110	0.4586	6195	86.0	86.6	104.8	-0.0112	1967
0.2100	0.4700	0.2105	0.4696	5640	94.2	92.3	102.0	-0.0062	1958
0.2100	0.4800	0.2098	0.4794	5263	97.4	94.9	102.0	-0.0014	1962

0.2100	0.4900	0.2096	0.4903	4910	98.8	95.1	101.2	0.0040	1948
0.2100	0.5000	0.2089	0.4998	4681	96.3	91.5	98.4	0.0091	1948
0.2100	0.5100	0.2092	0.5105	4428	91.9	84.7	93.9	0.0143	1937
0.2200	0.4600	0.2212	0.4585	5488	74.9	80.9	107.8	-0.0191	1953
0.2200	0.4700	0.2208	0.4691	5042	87.0	88.1	103.6	-0.0140	1953
0.2200	0.4800	0.2211	0.4790	4689	93.5	91.9	102.5	-0.0094	1941
0.2200	0.4900	0.2196	0.4905	4314	98.5	95.1	101.5	0.0006	1947
0.2200	0.5000	0.2192	0.4994	4268	98.2	94.7	100.9	0.0023	1944
0.2200	0.5100	0.2174	0.5094	4143	94.3	88.7	96.5	0.0087	1932
0.2300	0.4700	0.2302	0.4687	4523	77.6	82.7	107.0	-0.0206	1943
0.2300	0.4800	0.2305	0.4789	4232	88.2	89.4	103.9	-0.0154	1941
0.2300	0.4900	0.2308	0.4903	3977	95.2	93.7	103.5	-0.0094	1933
0.2300	0.5000	0.2300	0.5000	3840	97.1	95.5	103.1	-0.0036	1934
0.2300	0.5100	0.2296	0.5091	3722	96.0	93.3	100.1	0.0018	1928
0.2400	0.4800	0.2422	0.4792	3701	78.6	85.0	107.9	-0.0218	1936
0.2400	0.4900	0.2404	0.4906	3596	91.0	92.2	105.0	-0.0143	1930
0.2400	0.5000	0.2411	0.5001	3453	95.1	94.7	103.7	-0.0091	1945
0.2400	0.5100	0.2403	0.5099	3371	96.8	95.6	102.7	-0.0029	1944
0.2500	0.5000	0.2517	0.5003	3118	92.4	93.3	105.3	-0.0135	1943
0.2500	0.5100	0.2510	0.5102	3061	95.5	95.2	104.0	-0.0071	1945
0.2500	0.5200	0.2479	0.5188	3083	94.9	93.3	100.3	-0.0006	1923
0.2600	0.4900	0.2625	0.4895	2889	74.7	83.3	110.4	-0.0240	1923
0.2600	0.5000	0.2625	0.5004	2825	85.8	89.8	108.3	-0.0172	1913
0.2600	0.5100	0.2618	0.5105	2787	93.0	93.9	104.8	-0.0105	1933
0.2600	0.5200	0.2616	0.5205	2747	96.0	95.4	103.0	-0.0041	1931
0.2700	0.5000	0.2730	0.4997	2581	78.6	85.3	110.2	-0.0206	1910
0.2700	0.5100	0.2712	0.5110	2579	90.6	92.3	106.1	-0.0128	1930
0.2700	0.5200	0.2730	0.5203	2515	94.4	94.3	104.5	-0.0072	1928
0.2800	0.5100	0.2827	0.5103	2362	84.1	88.0	108.4	-0.0157	1929

0.2800	0.5200	0.2813	0.5200	2365	91.8	92.4	106.1	-0.0091	1936
0.2900	0.5100	0.2873	0.5095	2284	80.9	85.7	110.0	-0.0170	1890
0.2900	0.5200	0.2928	0.5205	2181	88.1	88.7	111.0	-0.0106	1935

Table 7-3. Measurements made with the UPRtek MK350S spectrometer and the ams AS7265x multiband colorimetric sensor.

MK350S CCT (K)	AS7265x CCT (K)	MK350S <i>R_a</i>	AS7265x <i>R_a</i>	MK350S <i>R_f</i>	AS7265x <i>R_f</i>
2792	2846	94.1	94.8	90.3	91.2
2994	3033	95.0	95.0	90.8	91.2
3363	3359	96.1	95.8	91.1	91.0
3649	3632	96.4	95.8	90.9	90.9
4075	4087	96.5	95.9	90.0	90.3
4598	4613	95.8	96.0	90.0	90.4
5280	5215	94.7	95.1	90.4	89.9
4833	4816	95.0	95.8	90.0	90.6
4253	4233	96.4	96.5	90.1	90.5
2778	2726	81.3	80.6	84.6	84.2
3109	3035	83.4	82.5	85.2	85.0
4811	4776	84.9	85.5	85.6	86.0
4074	4016	85.6	85.4	86.5	86.2
3865	3815	85.5	85.1	86.0	86.1
3709	3672	85.2	84.8	85.9	85.9
3593	3572	85.2	84.6	85.8	85.7
3344	3348	84.3	83.8	85.5	85.3
6463	6211	83.4	83.0	84.5	84.4
6117	5913	83.9	83.6	84.9	84.9
5903	5722	84.3	84.1	85.2	85.1
5737	5570	84.6	84.1	85.3	85.3
5243	5090	85.0	84.8	85.5	85.7
2607	2681	85.7	85.4	88.9	89.5
5829	5855	70.0	67.8	76.1	74.6

4021	3848	85.4	86.2	86.8	87.6
3434	3378	96.1	95.6	92.8	93.1
4022	3976	91.4	90.1	88.9	89.7
4798	4656	82.4	79.5	84.5	84.4
5904	5764	74.2	72.9	79.5	77.8
3807	3687	96.9	97.8	93.9	94.7
4806	4689	81.7	81.0	85.6	86.0

8 List of Figures

Figure 2-1. The electromagnetic spectrum, with the visible portion, highlighted [11].	14
Figure 2-2. Normalized blackbody radiation at different temperatures. The gray region indicates the visible range.....	16
Figure 2-3. Solar irradiance spectrum above the atmosphere (yellow) and surface (red) [17].....	17
Figure 2-4. Comparison of a black and white and color picture of a plant. If there is no color, it is much more difficult to distinguish the flowers from the rest of the plant.	18
Figure 2-5. Schematic diagram of the human eye [22].	19
Figure 2-6. Photopic eye sensitivity function [26].	21
Figure 2-7. Color matching functions for the Wright and Guild data [24].....	26
Figure 2-8. CIE 1931 XYZ color matching functions [32].	27
Figure 2-9. CIE 1931 chromaticity diagram generated using Luxpy library [34].....	29
Figure 2-10. CIE 1976 uniformity chromaticity scale diagram generated using Luxpy library.....	30
Figure 2-11. Situation of the Planckian locus in the CIE 1931 (left) and the CIE 1976 (right) chromaticity diagrams.....	32

Figure 2-12. Dynamic white light source working at different CCTs.	34
Figure 2-13. Example of the color gamut for a RGB LED display in the CIE 1931 chromaticity diagram.	36
Figure 2-14. Comparison between Rf and Ra values of 963 commercial LEDs. The diagonal black line serves as a reference to visualize the difference between Rf and Ra	40
Figure 2-15. Difference between circadian (orange) and photopic (blue) sensitivity functions [51].	41
Figure 2-16. Relationship between EML and CS (both at 100 lx) for 723 commercial white LEDs. The data have been obtained from information provided by the manufacturers.	44
Figure 2-17. Schematic of an LED [59].	46
Figure 2-18. Different LEDs presented in different packages [60].	47
Figure 2-19. Example of an LED PCB [61].	47
Figure 2-20. Typical forward current vs. forward voltage for LUXEON C PC Amber [62].	48
Figure 2-21. Typical normalized light output vs. forward current for LUXEON C Green, Cyan and Blue [62].	49
Figure 2-22. A square-shaped wave, example of PWM [63].	50
Figure 2-23. Different types of heat sinks [65].	51

Figure 2-24. Different types of reflectors [66].	52
Figure 2-25. Different optical diffusers used in linear lighting [67].	53
Figure 2-26. Example of a compact 5-channel LED strip (red, green, blue, warm white and cool white) commercialized by Samsung [69].	55
Figure 2-27. Production of metamers using Kumux platform [71]. In the first case, the system is composed of a single 2999 K warm white LED with a Duv of 0.0013. In the second case, the system is composed of a red, a cyan, a blue and a warm white which, combined together, can provide a CCT of 3009 K with a Duv of 0.0013. In both cases a standard observer will not be able to distinguish the color of the two light sources, although they have different Ra and M/P ratio parameters.	56
Figure 2-28. Multispectral horticultural luminaire by Valoya [79].	58
Figure 2-29. Typical operation of a color sensor (top) and a spectrometer (bottom). Normally, the spectrometer obtains a wavelength resolution unattainable for a color sensor [82].	59
Figure 2-30. UPRtek MK350S premium calibrated portable spectrometer [83].	60
Figure 2-31. ATMEGA328 microcontroller in two different versions [84].	61

Figure 2-32. Diagram of a NN consisting of 4 neurons in the input layer, 1 hidden layer consisting of 2 neurons, and an output layer with a single neuron.	68
Figure 4-1. Flow diagram of the developed algorithm.	75
Figure 4-2. Results of a simulation of a 5-channel light source (red, green, blue, warm white and cool white LEDs) at a resolution of 4 (top) and 16 (bottom) steps for the CIE 1931 (left) and CIE 1976 (right) chromaticity diagrams. Each dot corresponds to the chromatic position of each SPD.	78
Figure 4-3. Detail of the sectorization of the CIE 1976 chromaticity diagram.	80
Figure 4-4. R_a values distributed according to the coordinates (x, y) of the CIE 1931 chromaticity diagram. The color scale cuts the negative R_a values to a minimum value of 0.	83
Figure 4-5. R_a values distributed according to the (x, y) coordinates of the CIE 1931 color diagram viewed from above. The color scale cuts the smallest R_a values from 0 (top) and 80 (bottom) to facilitate the visualization of highest values.	84
Figure 4-6. Results of the maximization of the IES TM-30-18 R_f for 10000 K CCTs at different resolutions.	89
Figure 4-7. Results of the maximization of the M/P ratio for 3000 K CCTs white light ($-0.001 < D_{uv} < 0.001$) at different resolutions.	90

Figure 4-8. pySpy profiling of a simulation using the 1.0 version with 8 process and resolution 6.	92
Figure 4-9. Performance comparison between code versions 1.0 and 2.0.....	94
Figure 4-10. Time spent on input/output of versions 2.0 and 3.0 (left). Time spent on calculations of versions 2.0 and 3.0 (right).	96
Figure 4-11. Efficiency of the version 3.0 with resolution 16.	96
Figure 4-12. 723 white LEDs of the database represented on the CIE 1931 chromaticity diagram (left) and in the M/P ratio vs CCT chart (right).	98
Figure 4-13. M/P ratio vs CCT chart and comparison between white LEDs with similar M/P ratio but different CCT and vice versa.	99
Figure 4-14. Comparison between two LEDs with the same M/P ratio but very different CCT.....	99
Figure 4-15. Comparison between two LEDs with very similar CCT but different M/P ratio.	100
Figure 4-16. Relationship between M/P ratio, CCT and Ra applied to 723 commercial white LEDs.....	101
Figure 4-17. Achievable values of a multichannel luminaire for M/P ratio (left) and Ra (right) in function of CCT.	102

Figure 4-18. Achievable values of a multichannel LED system in order to get the maximum flexibility in M/P ratio.....	103
Figure 4-19. GUI of the program Color Perception.	106
Figure 4-20. Schematic view of the prototypes created. It is possible to see the electrical connections and communication paths between the different elements, separated by modules....	107
Figure 4-21. Picture of the breakout board used [103].	109
Figure 4-22. First version of the designed control system without the LED module.	112
Figure 4-23. First version of the LEDs PCB.	113
Figure 4-24. Design of tracks and layers of the developed driver PCB.....	114
Figure 4-25. Pictures of the control PCB inside the globe case.	114
Figure 4-26. Thermal image of the driver PCB while working.	115
Figure 4-27. Some of the LEDs of the selection process.....	116
Figure 4-28. Design of the developed LEDs PCB.	117
Figure 4-29. Picture of the manufactured LEDs PCB.	118
Figure 4-30. Thermal images of the PCB operating at 3000 K (20 minutes of operation) and maximum power. It is possible to see that the hottest spots are located above the LEDs R, G and B, where the highest electrical current circulates.	119

Figure 4-31. Second version of the prototype working within the integrating sphere.....	119
Figure 4-32. Various tests of the new control system designs ..	120
Figure 4-33. Schematics of the LED module PCB (left) and the control module PCB (right) of the light bulb prototype.....	122
Figure 4-34. Picture of the light bulb prototype inside the integrating sphere (left) and the different disassembled modules (right).....	122
Figure 4-35. Thermal image of the light bulb prototype without the optical diffuser after 20 minutes of operation.	123
Figure 4-36. Schematics of the LED module PCB (left) and the control module PCB (right) of the downlight prototype.	124
Figure 4-37. Picture of the downlight prototype without the covers.....	124
Figure 4-38. Thermal image of the LED module PCB (left) and the control module PCB (right) of the downlight prototype without the optical diffuser after 20 minutes of operation.	125
Figure 4-39. Schematics of the LED module PCB (left) and the control module PCB (right) of the floodlight prototype.	126
Figure 4-40. Picture of the floodlight prototype without the front cover	127

Figure 4-41. Thermal image of the LED module PCB (left) and the control module PCB (right) of the floodlight prototype without the front cover after 20 minutes of operation.128

Figure 4-42. Area represented with points with $Rf > 80$ accessible for the light bulb prototype.....131

Figure 4-43. Chromatic deviations of the points with $Rf > 80$ for the prototype light bulb. Circles have a distance radius of 0.0044 units.....131

Figure 4-44. Rf values of the warm white LED, the cool white LED and the values achieved by the spectral mixing algorithm measured on the bulb prototype.133

Figure 4-45. Area represented with points with $Rf > 80$ accessible for downlight prototypes.134

Figure 4-46. Chromatic deviations of the points with $Rf > 80$ for the downlight prototype. Circles have a distance radius of 0.0044 units.....134

Figure 4-47. Rf values of the warm white LED, the cool white LED and the values achieved by the spectral mixing algorithm measured on the downlight prototype.....135

Figure 4-48. Different scenes in the showroom installed at Parc Científic de Barcelona.137

Figure 4-49. Display of the error between the expected CCT and the measured CCT. The gray diagonal line is for reference.141

Figure 5-1. Schematic of the operation to improve the properties of a multichannel colorimetric sensor.	142
Figure 5-2. Diagram of the information flow, from data acquisition to the calculation of colorimetric parameters.	143
Figure 5-3. Schematic of AS72651, AS72652 and AS72653 devices.	145
Figure 5-4. Photodiode arrays for the AS72651, AS72652 and AS72653 sensors.	146
Figure 5-5. Normalized spectral response of the AS7265x module from ams AG. Each of the bands is labeled with a letter (A, B, C, D, E, F, G, H, R, I, S, J, T, U, V, W, K, L).	146
Figure 5-6. AS7265x module marketed by SparkFun Electronics [116].	147
Figure 5-7. Simulation of the normalized spectral response of the different sensor channels within the visible range (380 - 780 nm).	149
Figure 5-8. Simulation of the simulated sensor response (blue dots) compared to a randomly generated SPD (black solid line).	150
Figure 5-9. Example of the generation of a random SPD before normalization (black, bold). In this case, 8 individual Gaussian distributions (dotted lines) with the peak located between 380 and 780 nm and a variable FWHM from 30 to 60 nm have been used.	152

Figure 5-10. Schematic of the procedure to evaluate the error in the calculation of colorimetric parameters using the linear and cubic interpolations model.....154

Figure 5-11. Example of linear interpolation of sensor measurements (blue) for randomly generated SPDs (black).155

Figure 5-12. Example of cubic interpolation of sensor measurements (blue) for randomly generated SPDs (black).156

Figure 5-13. Comparison of the CCT calculation error for $2 \cdot 10^4$ random SPDs when the sensor measurements are linearly (left) and cubically (right) interpolated with respect to the real values. The black diagonal line serves as a reference to visualize the associated error in each case.....157

Figure 5-14. Distribution of the error committed in the calculation of the CCT for $2 \cdot 10^4$ random SPDs when the sensor measurements are linearly (left) and cubically (right) interpolated with respect to the real values.157

Figure 5-15. Comparison of the calculated Ra error for $2 \cdot 10^4$ random SPDs when the sensor measurements are linearly (left) and cubically (right) interpolated with the real values of the spectra. The black diagonal line serves as a reference to visualize the associated error in each case.159

Figure 5-16. Distribution of the error committed in the calculation of Ra for $2 \cdot 10^4$ random SPDs when the sensor measurements are linearly (left) and cubically (right) interpolated with respect to the real values.159

Figure 5-17. Comparison of the error of the Rf calculation for $2 \cdot 10^4$ random SPDs when the sensor measurements are linearly (left) and cubically (right) interpolated with the actual values of the spectra. The black diagonal line serves as a reference to visualize the associated error in each case.....160

Figure 5-18. Distribution of the error committed in the calculation of Rf for $2 \cdot 10^4$ random SPDs when the sensor measurements are linearly (left) and cubically (right) interpolated with respect to the real values.161

Figure 5-19. Schematic of the procedure to evaluate the error in the calculation of colorimetric parameters using the spectral reconstruction NN model.....163

Figure 5-20. Diagram of the operation of the spectral reconstruction NN.163

Figure 5-21. Example of spectral reconstruction of the simulated sensor measurements (blue) using a NN with a hidden layer with 128 neurons for randomly generated spectra (black solid line). 165

Figure 5-22. Example of spectral reconstruction of the simulated sensor measurements (blue) using a NN with two hidden layers with 2048 and 512 neurons for the randomly generated spectra (black).167

Figure 5-23. Evolution of the loss and accuracy values for the training (blue) and validation (orange) subsets as a function of the iterations in the NN training.....168

Figure 5-24. Comparison of the error in the calculation of CCT (purple), Ra (green) and Rf (blue) with respect to the real measurements for $2 \cdot 10^4$ random SPDs when the simulated sensor measurements are calculated through the spectral reconstruction NN (left column). Distribution of the error made in the calculation of CCT (purple), Ra (green) and Rf (blue) between the real values and those calculated through the spectral reconstruction NN (right column).169

Figure 5-25. Schematic of the procedure to evaluate the error in the calculation of colorimetric parameters using the NN model of colorimetric parameter calculation.171

Figure 5-26. Comparison of the error in the calculation of CCT (purple), Ra (green) and Rf (blue) with respect to the real measurements for $2 \cdot 10^4$ random SPDs when the simulated sensor measurements are calculated through the NN for the calculation of the corresponding colorimetric parameter (left column). Distribution of the error made in the calculation of CCT (purple), Ra (green) and Rf (blue) between the real values and those calculated through the NN for the calculation of the corresponding colorimetric parameter (right column).172

Figure 5-27. Example of the first 25 normalized spectral distributions from the database of real LED-sources.176

Figure 5-28. Comparison of the error in the calculation of CCT (purple), Ra (green) and Rf (blue) with respect to the real measurements for a set of 1479 real LED-sources using a spectral reconstruction NN (left column). Distribution of the error made in the calculation of the corresponding colorimetric parameter

between the real values and those calculated through the spectral reconstruction NN (right column).....	178
Figure 5-29. Comparison between the real SPD (black), the one created by the spectral reconstruction NN (blue), the cubically interpolated one (orange) and the simulated sensor values (black dots).	179
Figure 5-30. Side and top view of the AS7265x module and ATSAM21G18 microcontroller breakout boards.	181
Figure 5-31. Comparison of the error in the calculation of CCT (purple), R_a (green) and R_f (blue) with respect to experimental measurements for a set of 31 SPDs from real LED-sources using a spectral reconstruction NN (left column). Distribution of the error made in the calculation of the corresponding colorimetric parameter between the real values and those calculated through the spectral reconstruction NN (right column).	186
Figure 5-32. Relative error of the CCT of the AS7265x sensor with respect to the MK350S spectrometer. The points within the gray area are the points within the margin of error.....	188
Figure 5-33. Relative error of the R_a of the AS7265x sensor with respect to the MK350S spectrometer. The points within the gray area are the points within the error margin.	189
Figure 5-34. Relative error of the R_f of the AS7265x sensor with respect to the MK350S spectrometer. The points within the gray area are the points within the error margin.	190

Figure 5-35. Real SPD (black line), spectral reconstruction (blue line) and AS7265x module values (black dots) for 6 of the 31 measured SPDs.....191

Figure 5-36. User interface designed where the colorimetric sensor values (sensor_irradiance, black dots) and spectral reconstruction (data_irradiance, blue line), as well as CCT, *Ra* and *Rf* values can be obtained.192

9 List of Tables

Table 2-1. Relationship between color and wavelength [14].	15
Table 2-2. Reference values for outdoor daylighting and for different environments [27] [28].	23
Table 2-3. Examples of CCT and Ra values of different light sources [44] [45]. The LED values have been analyzed using a database that contains data of 963 commercial LEDs.	38
Table 4-1. Performance of the version 1.0 of the code with resolution 6.	91
Table 4-2. Performance of the versions 1.0 and 2.0 with resolution 6.	93
Table 4-3. Experimental data containing expected and measured values of CCT and Ra .	139
Table 5-1. Arithmetic mean, RMSE and standard deviation associated with the error of the CCT calculation for $2 \cdot 10^4$ random SPDs when sensor measurements are linearly and cubically interpolated.	158
Table 5-2. Arithmetic mean, RMSE and standard deviation associated with the error of the Ra calculation for $2 \cdot 10^4$ random SPDs when sensor measurements are linearly and cubically interpolated.	159
Table 5-3. Arithmetic mean, RMSE and standard deviation associated with the error of the Rf calculation for $2 \cdot 10^4$ random	

SPDs when sensor measurements are linearly and cubically interpolated.	161
Table 5-4. Arithmetic mean, RMSE and standard deviation associated with the error of the calculation of CCT, Ra and Rf for $2 \cdot 10^4$ random SPDs when sensor measurements are calculated through the spectral reconstruction NN.	170
Table 5-5. Arithmetic mean, RMSE and standard deviation associated with CCT calculation error for $2 \cdot 10^4$ random SPDs when using a CCT calculation NN with the simulated sensor measurements as input.	173
Table 5-6. Arithmetic mean, RMSE and standard deviation associated with Ra calculation error for $2 \cdot 10^4$ random SPDs when using a NN for Ra calculation with the simulated sensor measurements as input.	173
Table 5-7. Arithmetic mean, RMSE and standard deviation associated with Rf calculation error for $2 \cdot 10^4$ random SPDs when using an Rf calculation NN with the simulated sensor measurements as input.	173
Table 5-8. Summary of the arithmetic mean, RMSE and standard deviation values of the errors made in the different models used for $2 \cdot 10^4$ randomly created spectra. The smallest values for each case are marked in green.	174
Table 5-9. Summary of the arithmetic mean, RMSE and standard deviation values of the errors made in the different	

models used for the 1479 SPDs in the real LED-source database.
The smallest values for each case have been marked in green. .176

Table 5-10. Relative response of the different channels (A, B, C, D, E, F, G, H, I, J, R, S, T and U) of the AS7265x module as a function of the relative brightness of a light source.183

Table 5-11. Summary of the arithmetic mean, RMSE and standard deviation values of the errors made in the experimental measurements of 31 different SPDs.....187

Table 7-1. Light bulb prototype measurements.204

Table 7-2. Downlight prototype measurements.....206

Table 7-3. Measurements made with the UPRtek MK350S spectrometer and the ams AS7265x multiband colorimetric sensor.....209

10 References

- [1] H. Ries, I. Leike, J.A. Muschaweck, Optimized additive mixing of colored light-emitting diode sources, <https://doi.org/10.1117/1.1753273>. 43 (2004) 1531–1536.
- [2] L. Lohaus, E. Leicht, S. Dietrich, R. Wunderlich, S. Heinen, Advanced color control for multicolor LED illumination systems with parametric optimization, IECON Proceedings (Industrial Electronics Conference). (2013) 3305–3310. <https://doi.org/10.1109/IECON.2013.6699658>.
- [3] A. Llenas, J. Carreras, Arbitrary spectral matching using multi-LED lighting systems, <https://doi.org/10.1117/1.OE.58.3.035105>. 58 (2019) 035105.
- [4] A. Eissfeldt, T.Q. Khanh, Algorithm for real-time colour mixing of a five-channel LED system while optimising spectral quality parameters:, <https://doi.org/10.1177/14771535211058096>. (2021).
- [5] F. Zhang, H. Xu, Z. Wang, Optimizing spectral compositions of multichannel LED light sources by IES color fidelity index and luminous efficacy of radiation, Applied Optics, Vol. 56, Issue 7, Pp. 1962-1971. 56 (2017) 1962–1971. <https://doi.org/10.1364/AO.56.001962>.
- [6] J.N. Dodd, Introduction and History, Atoms and Light: Interactions. (1991) 1–6. https://doi.org/10.1007/978-1-4757-9331-4_1.
- [7] B.R. Masters, Albert Einstein and the Nature of Light, Optics and Photonics News, Vol. 23, Issue 7, Pp. 42-47.

- 23 (2012) 42–47.
<https://doi.org/10.1364/OPN.23.7.000042>.
- [8] J. Güémez, M. Fiolhais, L.A. Fernández, The principle of relativity and the de Broglie relation, *Am J Phys.* 84 (2016) 443. <https://doi.org/10.1119/1.4941569>.
- [9] Purcell and Morin, *Electricity and Magnetism*, 3rd ed., Cambridge University Press, New York, 2013.
- [10] M. Browne, *Physics for Engineering and Science*, 2nd ed., McGraw Hill/Schaum, New York, 2013.
- [11] Philip Ronan, File:EM spectrum.svg - Wikimedia Commons, (n.d.).
https://commons.wikimedia.org/wiki/File:EM_spectrum.svg (accessed January 17, 2022).
- [12] D.H. Sliney, What is light? The visible spectrum and beyond, *Eye* 2016 30:2. 30 (2016) 222–229.
<https://doi.org/10.1038/eye.2015.252>.
- [13] IES Method for Evaluating Light Source Color Rendition – Illuminating Engineering Society, (2018) 26.
<https://www.ies.org/product/ies-method-for-evaluating-light-source-color-rendition/> (accessed January 13, 2022).
- [14] E.F. Schubert, *Light-Emitting Diodes*, 2nd ed., Cambridge University Press, 2006.
- [15] G.S. Ranganath, Black-body radiation, *Resonance* 2008 13:2. 13 (2008) 115–133. <https://doi.org/10.1007/S12045-008-0028-7>.
- [16] Sun Fact Sheet, (n.d.).
<https://nssdc.gsfc.nasa.gov/planetary/factsheet/sunfact.html> (accessed January 17, 2022).
- [17] Nick84, File:Solar spectrum en.svg - Wikimedia Commons, (n.d.).

- https://commons.wikimedia.org/wiki/File:Solar_spectrum_en.svg (accessed January 17, 2022).
- [18] T.W. Cronin, Visual Ecology, *The Senses: A Comprehensive Reference*. 1 (2008) 211–245.
<https://doi.org/10.1016/B978-012370880-9.00337-6>.
- [19] S. Laureys, M. Boly, G. Moonen, P. Maquet, Two Dimensions of Consciousness: Arousal and Awareness, *Neuroscience*. 2 (2009) 1133–1142.
http://www.coma.ulg.ac.be/papers/vs/EncConsc_coma_2009.pdf (accessed January 17, 2022).
- [20] G.C. Brainard, J.R. Hanifin, J.M. Greeson, B. Byrne, G. Glickman, E. Gerner, M.D. Rollag, Action Spectrum for Melatonin Regulation in Humans: Evidence for a Novel Circadian Photoreceptor, *Journal of Neuroscience*. 21 (2001) 6405–6412.
<https://doi.org/10.1523/JNEUROSCI.21-16-06405.2001>.
- [21] K.S. Chew, J.M. Renna, D.S. McNeill, D.C. Fernandez, W.T. Keenan, M.B. Thomsen, J.L. Ecker, G.S. Loevinsohn, C. Vandunk, D.C. Vicarel, A. Tufford, S. Weng, P.A. Gray, M. Cayouette, E.D. Herzog, H. Zhao, D.M. Berson, S. Hattar, A subset of iprgcs regulates both maturation of the circadian clock and segregation of retinogeniculate projections in mice, *Elife*. 6 (2017).
<https://doi.org/10.7554/ELIFE.22861>.
- [22] Rhcastilhos, Jmarchn, File:Schematic diagram of the human eye en.svg - Wikimedia Commons, (n.d.).
https://commons.wikimedia.org/wiki/File:Schematic_diagram_of_the_human_eye_en.svg (accessed January 17, 2022).

- [23] O. Muftuoglu, F. Karel, R. Duman, Effect of a yellow intraocular lens on scotopic vision, glare disability, and blue color perception, *J Cataract Refract Surg.* 33 (2007) 658–666. <https://doi.org/10.1016/J.JCRS.2006.12.018>.
- [24] T. Gevers, A. Gijsenij, J. van de Weijer, J.-M. Geusebroek, Color Vision, in: *Color in Computer Vision: Fundamentals and Applications*, 1st ed., John Wiley & Sons, Inc., Hoboken, New Jersey, 2012: pp. 14–14.
- [25] H. Okumura, M. Fukusaki, S. Takubo, K. Arai, Development of a human vision simulation camera and its application, <https://doi.org/10.1117/12.912151>. 8295 (2012) 470–477.
- [26] CIE, CIE 784 TN003 Toolbox, (n.d). files.cie.co.at/784_TN003_Toolbox.xls (accessed January 26, 2022).
- [27] C. Kofod, *Indoor Lighting in the Public and Private Service Sectors*, Virum, 2017. <https://ec.europa.eu/research/participants/documents/downloadPublic?documentIds=080166e5b6d1bf85&appId=PGMS> (accessed February 22, 2022).
- [28] K.M. Al-Obaidi, M.A. Ismail, A.M. Abdul Rahman, Assessing the allowable daylight illuminance from skylights in single-storey buildings in Malaysia: a review, *Ceased.* 6 (2016) 236–248. <https://doi.org/10.1080/2093761X.2015.1129369>.
- [29] Y. Ohno, CIE Fundamentals for Color Measurements, in: *IS&T NIP16 Conference*, 2000.
- [30] W.D. Wright, A re-determination of the trichromatic coefficients of the spectral colours, *Transactions of the*

- Optical Society. 30 (1929) 141.
<https://doi.org/10.1088/1475-4878/30/4/301>.
- [31] B.J. Guild, F. InstP, The colorimetric properties of the spectrum, Philosophical Transactions of the Royal Society of London. Series A, Containing Papers of a Mathematical or Physical Character. 230 (1931) 149–187.
<https://doi.org/10.1098/RSTA.1932.0005>.
- [32] E.F. Schubert, Light-Emitting Diodes, 2nd ed., Cambridge University Press, 2006.
- [33] E.F. Schubert, Light-Emitting Diodes, 2nd ed., Cambridge University Press, 2006.
- [34] K.A.G. Smet, Tutorial: The LuxPy Python Toolbox for Lighting and Color Science, LEUKOS - Journal of Illuminating Engineering Society of North America. 16 (2020) 179–201.
<https://doi.org/10.1080/15502724.2018.1518717>.
- [35] E.F. Schubert, Light-Emitting Diodes, 2nd ed., Cambridge University Press, 2006.
- [36] N. Ohta, A.R. Robertson, Colorimetry Fundamentals and Applications, in: 1st ed., Wiley-IS&T Series in Imaging Science and Technology, 2005: pp. 83–83.
- [37] A.R. Robertson, Computation of Correlated Color Temperature and Distribution Temperature, JOSA, Vol. 58, Issue 11, Pp. 1528-1535. 58 (1968) 1528–1535.
<https://doi.org/10.1364/JOSA.58.001528>.
- [38] Y. Ohno, Practical Use and Calculation of CCT and Duv, <http://dx.doi.org/10.1080/15502724.2014.839020>. 10 (2013) 47–55.

- [39] Jackson Andrew, J. Jiao, Willism Karen B., *Electric Lamps - Specifications for the Chromaticity of Solid-state Lighting Products*, ANSI C78.377-2015, 2015.
- [40] T. Ajito, T. Obi, M. Yamaguchi, N. Ohyama, Expanded color gamut reproduced by six-primary projection display, <https://doi.org/10.1117/12.383364.3954> (2000) 130–137.
- [41] C.I. de l’Eclairage, *International lighting vocabulary*, Paris, CIE. (1970).
- [42] E.F. Schubert, *Light-Emitting Diodes*, (2006) 315.
- [43] K. Houser, M. Mossman, K. Smet, L. Whitehead, Tutorial: Color Rendering and Its Applications in Lighting, <https://doi.org/10.1080/15502724.2014.989802.12> (2015) 7–26.
- [44] M.R. Luo, The quality of light sources, *Coloration Technology*. 127 (2011) 75–87.
<https://doi.org/10.1111/J.1478-4408.2011.00282.X>.
- [45] Y. Ohno, Spectral design considerations for white LED color rendering, <https://doi.org/10.1117/1.2130694.44> (2005) 111302.
- [46] F. Zhang, Evaluation of changing the components involved in CIE color rendering index, *Optik (Stuttg)*. 219 (2020) 165261.
<https://doi.org/10.1016/J.IJLEO.2020.165261>.
- [47] IES Method for Evaluating Light Source Color Rendition – Illuminating Engineering Society, (2018) 26.
<https://www.ies.org/product/ies-method-for-evaluating-light-source-color-rendition/> (accessed February 16, 2022).
- [48] G.C. Brainard, J.R. Hanifin, J.M. Greeson, B. Byrne, G. Glickman, E. Gerner, M.D. Rollag, Action Spectrum for Melatonin Regulation in Humans: Evidence for a Novel

- Circadian Photoreceptor, *Journal of Neuroscience*. 21 (2001) 6405–6412.
<https://doi.org/10.1523/JNEUROSCI.21-16-06405.2001>.
- [49] K.Y. Wong, F.A. Dunn, D.M. Berson, Photoreceptor Adaptation in Intrinsically Photosensitive Retinal Ganglion Cells, *Neuron*. 48 (2005) 1001–1010.
<https://doi.org/10.1016/J.NEURON.2005.11.016>.
- [50] A. Kawasaki, R.H. Kardon, Intrinsically photosensitive retinal ganglion cells, *Journal of Neuro-Ophthalmology*. 27 (2007) 195–204.
<https://doi.org/10.1097/WNO.0B013E31814B1DF9>.
- [51] N.J. Miller, E. Noell-Waggoner, R. Baier, J. Collier, D. Gifford, E. McCreedy, C. Mills, S. Stringer, R. Uth, T.F. Wetle, Measuring Light Exposure and its Effects on Sleep and Behavior in Care Center Residents, Sacramento, CA, 2019.
- [52] A. Barroso, K. Simons, P. de Jager, Metrics of circadian lighting for clinical investigations:,
<http://dx.doi.org/10.1177/1477153513502664>. 46 (2013) 637–649.
- [53] Circadian Lighting: An Engineer’s Perspective – Illuminating Engineering Society, (n.d.).
<https://www.ies.org/fires/circadian-lighting-an-engineers-perspective/> (accessed February 23, 2022).
- [54] Circadian lighting design | WELL Standard, (n.d.).
<https://standard.wellcertified.com/light/circadian-lighting-design> (accessed February 23, 2022).
- [55] M/P ratios – Can we agree on how to calculate them? – Illuminating Engineering Society, (n.d.).

- <https://www.ies.org/fires/m-p-ratios-can-we-agree-on-how-to-calculate-them/> (accessed February 22, 2022).
- [56] A. Sánchez-cano, J. Aporta, Optimization of Lighting Projects Including Photopic and Circadian Criteria: A Simplified Action Protocol, *Applied Sciences* 2020, Vol. 10, Page 8068. 10 (2020) 8068.
<https://doi.org/10.3390/APP10228068>.
- [57] M. Bürmen, F. Pernu, B. Likar, LED light sources: a survey of quality-affecting factors and methods for their assessment, *Meas Sci Technol.* 19 (2008) 122002.
<https://doi.org/10.1088/0957-0233/19/12/122002>.
- [58] National Research Council, Assessment of Advanced Solid-State Lighting, in: 2013: pp. 35–37.
<https://doi.org/10.17226/18279>.
- [59] S-kei, File:PnJunction-LED-E.svg, (2011).
<https://commons.wikimedia.org/wiki/File:PnJunction-LED-E.svg> (accessed February 23, 2022).
- [60] Dispositivos optoelectrónicos | Iluminación led - Blanca | DigiKey, (n.d.).
<https://www.digikey.es/es/products/filter/iluminaci%C3%B3n-led-blanca/124?s=N4IgTCBcDaIDYFMAMiC6BfIA> (accessed February 23, 2022).
- [61] 2057-A-579-915A ADURA LED Soutions | Dispositivos optoelectrónicos | DigiKey Marketplace, (n.d.).
<https://www.digikey.es/es/products/detail/adura-led-soutions/2057-A-579-915A/15851116> (accessed February 24, 2022).
- [62] Lumileds, LUXEON C Color Line, (n.d.).
<https://lumileds.com/wp-content/uploads/files/DS144->

- luxeon-c-color-line-datasheet.pdf (accessed February 24, 2022).
- [63] C. Buttay, File:Duty cycle general.svg, (n.d.).
https://en.wikipedia.org/wiki/File:Duty_cycle_general.svg (accessed February 24, 2022).
- [64] L. Sun, J. Zhu, H. Wong, Simulation and evaluation of the peak temperature in LED light bulb heatsink, *Microelectronics Reliability*. 61 (2016) 140–144.
<https://doi.org/10.1016/J.MICROREL.2015.12.023>.
- [65] Ventiladores, gestión térmica | Dispositivos térmicos - disipadores térmicos | DigiKey, (n.d.).
<https://www.digikey.es/es/products/filter/dispositivos-t%C3%A9rmicos-disipadores-t%C3%A9rmicos/219?s=N4IgTCBcDaIBYFMCGAXAzgSwHYGsQF0BfIA> (accessed February 25, 2022).
- [66] Reflectores LED Farnell ES, (n.d.).
<https://es.farnell.com/c/componentes-de-iluminacion-led/reflectores-led?st=reflector> (accessed February 25, 2022).
- [67] ▷ Perfiles de superficie para tiras led - Proyectos a medi..., (n.d.). https://www.ledbox.es/iluminacion-led/perfiles-superficie-tira-led/7|tags*1:28 (accessed February 25, 2022).
- [68] K. Eskins, Light-quality effects on Arabidopsis development. Red, blue and far-red regulation of flowering and morphology, *Physiol Plant*. 86 (1992) 439–444.
<https://doi.org/10.1111/J.1399-3054.1992.TB01341.X>.
- [69] Tira LED SAMSUNG SMD5050, RGB+CCT, DC24V, 5m (60Led/m 5 en 1) - I..., (n.d.).
<https://www.ledbox.es/tiras-de-led/tira-led-samsung->

smd5050-rgb-cct-dc24v-5m-(60led-m-5-en-1)-ip20

(accessed March 1, 2022).

- [70] D. Miyazaki, M. Nakamura, M. Baba, R. Furukawa, S. Hiura, Optimization of LED illumination for generating metamerism, *Journal of Imaging Science and Technology*. 60 (2016).
<https://doi.org/10.2352/J.IMAGINGSCI.TECHNOL.2016.60.6.060502>.
- [71] Kumux | Spectral solutions focused on human centring lighting, (n.d.). <https://kumux.io/> (accessed March 16, 2022).
- [72] A. Wunsch, K. Matuschka, A controlled trial to determine the efficacy of red and near-infrared light treatment in patient satisfaction, reduction of fine lines, wrinkles, skin roughness, and intradermal collagen density increase, *Photomed Laser Surg*. 32 (2014) 93–100.
<https://doi.org/10.1089/PHO.2013.3616/ASSET/IMAGES/LARGE/FIGURE4.JPEG>.
- [73] C. Volf, A.S. Aggestrup, P.M. Petersen, C. Dam-Hansen, U. Knorr, E.E. Petersen, J. Engstrøm, J.C. Jakobsen, T.S. Hansen, H.Ø. Madsen, I. Hageman, K. Martiny, Dynamic LED-light versus static LED-light for depressed inpatients: study protocol for a randomised clinical study, *BMJ Open*. 10 (2020) e032233.
<https://doi.org/10.1136/BMJOPEN-2019-032233>.
- [74] J. Chen, S. Loeb, J.H. Kim, LED revolution: fundamentals and prospects for UV disinfection applications, *Environ Sci (Camb)*. 3 (2017) 188–202.
<https://doi.org/10.1039/C6EW00241B>.

- [75] K. Curtis, High Power IR LED Driver Using the PIC16C781/782 , 2015.
- [76] C.C.S. Nicole, F. Charalambous, S. Martinakos, S. van de Voort, Z. Li, M. Verhoog, M. Krijn, Lettuce growth and quality optimization in a plant factory, *Acta Hort.* 1134 (2016) 231–238.
<https://doi.org/10.17660/ACTAHORTIC.2016.1134.31>.
- [77] S. Afshari, L. Moynihan, S. Mishra, An optimisation toolbox for multi-colour LED lighting;, *Light* 50 (2016) 467–481.
<https://doi.org/10.1177/1477153516669881>
- [78] A. Llenas, J. Carreras, Arbitrary spectral matching using multi-LED lighting systems, *Opt. Eng.* 58 (2019) 035105.
<https://doi.org/10.1117/1.OE.58.3.035105>.
- [79] LightDNA - Valoya LED Grow Lights, (n.d.).
<https://www.valoya.com/lightdna/> (accessed March 1, 2022).
- [80] sensor noun - Definition, pictures, pronunciation and usage notes | Oxford Advanced Learner’s Dictionary at OxfordLearnersDictionaries.com, (n.d.).
<https://www.oxfordlearnersdictionaries.com/definition/english/sensor?q=sensor> (accessed March 2, 2022).
- [81] Color Sensors | ams, (n.d.). <https://ams.com/en/color-sensors> (accessed March 14, 2022).
- [82] What is the difference between a Colorimeter and Spectrometer? | UPRtek, (n.d.).
<https://www.uprtek.com/en/blogs/difference-between-colorimeter-and-spectrometer> (accessed May 10, 2022).

- [83] MK350S Premium Spectrometer | UPRtek, (n.d.).
<https://www.uprtek.com/en/product/spectrometers/mk350s-premium> (accessed December 13, 2021).
- [84] ATMEGA328-AU - MCU, 8 Bits, Flash de 32KB,
Microcontroladores de Familia AVR ATmega, Serie
ATmega328, 20MHz, (n.d.).
<https://es.farnell.com/microchip/atmega328-au/mcu-8bit-atmega-20mhz-tqfp-32/dp/1972086> (accessed March 15, 2022).
- [85] N. Karumanchi, Data Structures And Algorithmic Thinking With Python, in: CareerMonk.com, 2020: pp. 20–20.
- [86] DIALux - DIAL, (n.d.). <https://www.dial.de/en/dialux/> (accessed March 15, 2022).
- [87] Tracepro, illumination and non-imaging optical design & analysis tool., (n.d.). <https://lambdare.com/tracepro/> (accessed March 15, 2022).
- [88] Y.J. Saw, V. Kalavally, C.P. Tan, The Spectral Optimization of a Commercializable Multi-Channel LED Panel with Circadian Impact, *IEEE Access*. 8 (2020) 136498–136511.
<https://doi.org/10.1109/ACCESS.2020.3010339>.
- [89] F. Zhang, H. Xu, Z. Wang, Spectral design methods for multi-channel LED light sources based on differential evolution, *Applied Optics*, Vol. 55, Issue 28, Pp. 7771-7781. 55 (2016) 7771–7781.
<https://doi.org/10.1364/AO.55.007771>.
- [90] A. Llenas, J. Carreras, Arbitrary spectral matching using multi-LED lighting systems,

- <https://doi.org/10.1117/1.OE.58.3.035105>. 58 (2019) 035105.
- [91] P. Mehta, M. Bukov, C.-H. Wang, A.G.R. Day, C. Richardson, C.K. Fisher, D.J. Schwab, A high-bias, low-variance introduction to Machine Learning for physicists, *Phys Rep.* 810 (2018) 1–124.
<https://doi.org/10.1016/j.physrep.2019.03.001>.
- [92] G. Carleo, I. Cirac, K. Cranmer, L. Daudet, M. Schuld, N. Tishby, L. Vogt-Maranto, L. Zdeborová, Machine learning and the physical sciences, *Rev Mod Phys.* 91 (2019) 045002.
<https://doi.org/10.1103/REVMODPHYS.91.045002/FIGURES/8/MEDIUM>.
- [93] S. Vaswani, F. Bach, M. Schmidt, Fast and Faster Convergence of SGD for Over-Parameterized Models and an Accelerated Perceptron, in: K. Chaudhuri, M. Sugiyama (Eds.), *Proceedings of the Twenty-Second International Conference on Artificial Intelligence and Statistics*, PMLR, 2019: pp. 1195–1204.
<https://proceedings.mlr.press/v89/vaswani19a.html>.
- [94] D. Svozil, V. Kvasnička, J. Pospíchal, Introduction to multi-layer feed-forward neural networks, *Chemometrics and Intelligent Laboratory Systems.* 39 (1997) 43–62.
[https://doi.org/10.1016/S0169-7439\(97\)00061-0](https://doi.org/10.1016/S0169-7439(97)00061-0).
- [95] S. Sharma, S. Sharma, A. Athaiya, Activation functions in neural networks, *Towards Data Science.* 6 (2017) 310–316.
- [96] B. Ding, H. Qian, J. Zhou, Activation functions and their characteristics in deep neural networks, *Proceedings of the 30th Chinese Control and Decision Conference, CCDC*

2018. (2018) 1836–1841.
<https://doi.org/10.1109/CCDC.2018.8407425>.
- [97] G. Bebis, M. Georgiopoulos, Why network size is so important, *IEEE Potentials*. 13 (1994) 27–31.
<https://doi.org/10.1109/45.329294>.
- [98] J. Fan, Y. Li, I. Fryc, C. Qian, X. Fan, G. Zhang, Machine-Learning Assisted Prediction of Spectral Power Distribution for Full-Spectrum White Light-Emitting Diode, *IEEE Photonics J.* 12 (2020).
<https://doi.org/10.1109/JPHOT.2019.2962818>.
- [99] A. Huguet-Ferran, C.M. Pérez, High resolution calculation for the optimisation of commercial LED spectra in health applications, (2021).
<https://doi.org/10.5281/ZENODO.5154666>.
- [100] Awards – LpS Digital, (n.d.). <https://led-professional-symposium.com/awards/> (accessed April 27, 2022).
- [101] ap--/python-seabreeze: Python module for oceanoptics spectrometers, (n.d.). <https://github.com/ap--/python-seabreeze> (accessed May 2, 2022).
- [102] ATSAMD21G18 | Microchip Technology, (n.d.).
<https://www.microchip.com/en-us/product/ATSamd21g18> (accessed November 18, 2021).
- [103] SparkFun SAMD21 Mini Breakout - DEV-13664 - SparkFun Electronics, (n.d.).
<https://www.sparkfun.com/products/13664> (accessed November 18, 2021).
- [104] Adafruit DS3231 Precision RTC Breakout : ID 3013 : \$17.50 : Adafruit Industries, Unique & fun DIY electronics and kits, (n.d.). <https://www.adafruit.com/product/3013> (accessed May 2, 2022).

- [105] P. Teikari, R.P. Najjar, H. Malkki, K. Knoblauch, D. Dumortier, C. Gronfier, H.M. Cooper, An inexpensive Arduino-based LED stimulator system for vision research, *J Neurosci Methods*. 211 (2012) 227–236.
<https://doi.org/10.1016/J.JNEUMETH.2012.09.012>.
- [106] PicoBuck Hookup Guide v12 - learn.sparkfun.com, (n.d.).
<https://learn.sparkfun.com/tutorials/picobuck-hookup-guide-v12> (accessed May 3, 2022).
- [107] EAGLE | PCB Design And Electrical Schematic Software | Autodesk, (n.d.).
<https://www.autodesk.com/products/eagle/overview?term=1-YEAR&tab=subscription> (accessed May 3, 2022).
- [108] Support for FLIR E5 | Teledyne FLIR, (n.d.).
<https://www.flir.es/support/products/e5/#Overview> (accessed May 3, 2022).
- [109] TLC5947 data sheet, product information and support | TI.com, (n.d.). <https://www.ti.com/product/TLC5947> (accessed May 4, 2022).
- [110] BCN3D Sigma R19 3D Printer - BCN3D Technologies, (n.d.). <https://www.bcn3d.com/bcn3d-sigma-r19/> (accessed May 5, 2022).
- [111] Tinkercad | Create 3D digital designs with online CAD | Tinkercad, (n.d.). <https://www.tinkercad.com/> (accessed May 5, 2022).
- [112] Tuya Smart - Global IoT Development Platform Service Provider, (n.d.). <https://www.tuya.com/> (accessed May 12, 2022).
- [113] Bombillas inteligentes Smart Wifi RGBWW 9W | Smart Home, (n.d.). <https://www.barcelonaled.com/smart->

- home/bombilla-smart-wifi-rgbww-e27-9w.html (accessed May 12, 2022).
- [114] M. Abadi, M. Isard, D.G.M. Google Brain, A Computational Model for TensorFlow An Introduction, Proceedings of the 1st ACM SIGPLAN International Workshop on Machine Learning and Programming Languages. (n.d.). <https://doi.org/10.1145/3088525>.
- [115] ams AG, ams Datasheet AS7265x Smart 18-Channel VIS to NIR Spectral_ ID 3-Sensor Chipset with Electronic Shutter, n.d.
- [116] SparkFun Triad Spectroscopy Sensor - AS7265x (Qwiic) - SEN-15050 - SparkFun Electronics, (n.d.). <https://www.sparkfun.com/products/15050> (accessed November 18, 2021).
- [117] C.M. Bishop, Neural networks and their applications, Review of Scientific Instruments. 65 (1998) 1803. <https://doi.org/10.1063/1.1144830>.
- [118] S. Jost, EMPIR 15SIB07 PhotoLED - Database of LED product spectra, (2021). <https://doi.org/10.11583/DTU.12783389.v1>.
- [119] Tinkercad | Create 3D digital designs with online CAD | Tinkercad, (n.d.). <https://www.tinkercad.com/> (accessed December 9, 2021).
- [120] Original Prusa i3 MK3S+ 3D printer | Original Prusa 3D printers directly from Josef Prusa, (n.d.). <https://www.prusa3d.com/product/original-prusa-i3-mk3s-3d-printer-3/> (accessed December 9, 2021).
- [121] Welcome to Flask — Flask Documentation (2.1.x), (n.d.). <https://flask.palletsprojects.com/en/2.1.x/> (accessed May 12, 2022).

